



Australian Government
Department of Defence
Defence Science and
Technology Organisation

A large, stylized, textured graphic of the letters 'DSTO' in a bold, sans-serif font, positioned vertically on the left side of the page.

Fatigue Life Estimate of Centre-Box Lug in Seahawk's Stabilator

Frank G. Polanco and
Robert P.H. Boykett

DSTO-TR-1590

DISTRIBUTION STATEMENT A
Approved for Public Release
Distribution Unlimited

BEST AVAILABLE COPY



Australian Government
Department of Defence
Defence Science and
Technology Organisation

Fatigue Life Estimate of Centre-Box Lug in Seahawk's Stabilator

Frank G. Polanco and Robert P. H. Boykett

**Air Vehicles Division
Platforms Sciences Laboratory**

DSTO-TR-1590

ABSTRACT

The fatigue failure of a centre-box lug, found in the Seahawk's stabilator, highlighted deficiencies in the fatigue life assessment of helicopter airframe structure. Thus a methodology for fatigue life assessment was developed using this cracked lug as a demonstrator. Indirect measurements from the Flight Loads Survey on the Black Hawk, although not ideal, allowed the estimation of the amplitude and frequency of the lug's loading. Of the sixteen assumptions made in this fatigue analysis, the most restrictive was that a high amplitude and high frequency loading acts for the entire flying time. Three different fatigue lives were obtained based on different levels of conservatism in the loading estimates. These three loadings were: the worst-case scenario, a high loading scenario, and a best-case scenario. The worst-case and high-loading scenarios resulted in low fatigue lives, while the best-case scenario resulted in an unlimited life for the cracked lug. It was surprising to find such low fatigue lives for two of these scenarios, but these low lives may be due to the conservative assumptions used in the analysis.

APPROVED FOR PUBLIC RELEASE

AQ F04-12-1715

20041008 550

Published by

*DSTO Platforms Sciences Laboratory
506 Lorimer St,
Fishermans Bend, Victoria, Australia 3207*

Telephone: (03) 9626 7000

Facsimile: (03) 9626 7999

© Commonwealth of Australia 2004

AR No. AR-013-125

July 2004

APPROVED FOR PUBLIC RELEASE

Fatigue Life Estimate of Centre-Box Lug in Seahawk's Stabilator

EXECUTIVE SUMMARY

During the routine folding of a Seahawk stabilator in June 2003, a crack was found in the centre-box lug, which had accrued only 402 flight hours. Had this cracked lug gone unnoticed, the eventual loss of the stabilator mid-flight could have resulted in loss of control—and the potential loss of the crew and aircraft. The simplified fatigue analysis undertaken in this report investigates the possibility of this fatigue cracking occurring in other Seahawk helicopters operated by the Australian Defence Force (ADF). However, the primary intention was not to define an alternative fatigue life, but to (i) explore a *methodology* for and (ii) develop DSTO's *capability* in assessing the fatigue life of helicopter airframe structure. In other words, the fatigue analysis undertaken on the lug was used as a demonstrator of this developed methodology.

A significant limitation was that only indirect loading information was available for the Seahawk's stabilator. We used the measurements taken in 2000 during the Flight Loads Survey for the Black Hawk as the indirect information to estimate the lug loading. The indirect nature of the loading measurements meant that the fatigue analysis required sixteen assumptions. The two coarsest assumptions were: (1) The estimated high loading acted for the entire flight time. (2) The cycle counting (for fatigue purposes) could be estimated from the frequency decomposition of the loading's time-history.

The fatigue analysis relied upon bending stresses resulting from stabilator buffeting during flight. These bending stresses were measured by a strain gauge bridge that was located 9.2 inches from the cracked lug and directly above the forward spar on the stabilator's skin. Thus the loading on the cracked lug itself had to be calculated indirectly by assuming a particular lifting distribution on the stabilator.

The lug's fatigue life was calculated for three cases, which included a case termed the worst-case scenario. This worst-case considered fatigue under a "harsh" loading environment and resulted in a short fatigue life. This short life was of concern because the cracked lug was life unlimited. We would have expected that such a conservatively designed lug (one with an unlimited life) would yield a long fatigue life even under the worst-case scenario. In fact, the opposite was found—namely, a short component life—but this result is possibly due to the two coarse assumptions listed above. The analysis in this report suggests that fatigue might be a problem in other Seahawks in the ADF's fleet. However, a full fatigue analysis (using the suggested refinements made in this report) would be required to further quantify the fatigue susceptibility of the centre-box lug in question.

The load path from the stabilator to the centre-box is redundant, and so a crack detection (instead of crack prevention) program would be sufficient for safety. Within the fidelity of results obtained so far, the work carried out in this report does *not* conflict with Sikorsky's assessment of an unlimited fatigue life.

Authors



Frank G. Polanco

Air Vehicles Division

Frank Polanco graduated in 1992 with a Bachelor of Aerospace Engineering (Honours) and a Bachelor of Applied Science (Distinction) from the Royal Melbourne Institute of Technology (RMIT). He joined the Platforms Sciences Laboratory (PSL) in 1993, working on aircraft structural integrity and fatigue life monitoring before returning to RMIT to complete a Doctorate in Mathematics. He then rejoined the PSL in 1998 to work in the area of helicopter life assessment. At PSL he has worked on: loads synthesis of helicopter-rotor component, fatigue and cost effects of spectrum perturbations, component reliability, and measures for vibrational modes.



Robert P. H. Boykett

Air Vehicles Division

Robert Boykett is a graduate of the Royal Melbourne Institute of Technology with a Bachelor Degree of Aeronautical Engineering in 1984. At the Government Aircraft Factories (now Boeing Australia) he undertook detail design and stress analysis of civil and military aircraft components in production, including repairs to metallic and composite structures. His work at the Defence Science and Technology Organisation, since 1990, has been in the field of aircraft structural integrity, especially testing. Major tasks have been the development of the F/A-18 IFOSTP test rig, the certification testing program for a composite repair to F-111 wing skins and co-ordination of the Joint USAF-ADF Black Hawk Flight Load Survey. Current duties are managing Helicopter Structural Integrity of all Army and Navy rotary-wing platforms.

Contents

Notation	xiii
1 Introduction	1
1.1 Description of Cracked Lug and Design Review	2
1.2 Philosophy behind Fatigue Analysis	5
1.3 Synopsis of Assumptions	6
2 Stabilator's Geometry and Gauge Locations	8
2.1 Stabilator Strain Gauge and Accelerometer Locations	8
2.2 Geometry of Forward and Aft Stabilator Spars	10
3 Stabilator Loading	14
3.1 External Loads on Stabilator	14
3.2 Vertical Load on Stabilator Spars	15
3.3 Horizontal (Spanwise) Load on Stabilator Spars	19
3.4 Using Vertical Load to Calculate Horizontal Load on Spars	21
4 Information from Flight Loads Survey	23
4.1 Partitioning 526 Manoeuvres into 12 Groups	23
4.2 Statistically Reduced Data Set of Flight Loads Survey	25
5 Bending Stress on Stabilator Spar	28
5.1 Fatigue Equation for 7075 Aluminium Alloy	28
5.2 Worst-Case Bending Stress from Flight Loads Survey	29
5.3 High Bending Stress from Flight Loads Survey	32
5.4 Best-Case Bending Stress from Flight Loads Survey	36
6 Fatigue of Cracked Lug	37
6.1 Stabilator Frequency Response during Level Flight	37
6.2 Stress and Fatigue on Centre-Box Lug	41
7 Summary	46
Acknowledgements	48
References	49

Appendices

A	Engineering Drawings	51
B	Twelve Manoeuvre Groups	69
C	Mathematica Code for Bending Stress Plots	75
D	Bending Stress from Flight Loads Survey	83
E	Frequency Response of Rolling Pullout and Rough Approach	109
F	Bending Stress on Wing Panel Lug	116
G	Fractographic Analysis	120

Figures

1.1	Line drawing of the starboard side stabilator and centre-box	1
1.2	Aft portion of clevis lug completely cracked	3
1.3	Stabilator centre-box and close-up of lug's broken portion	4
2.1	Stabilator gauge locations during Flight Loads Survey	9
2.2	Caps of both forward and aft spars on horizontal stabilator	11
2.3	Estimated dimensions of the forward and aft spars	12
3.1	Free-body diagram of cross-sectional loads on spar	15
3.2	Horizontal (spanwise) loading, a product of stress and area.	17
5.1	Maximum stress versus stress ratio plot for Flight Loads Survey	30
5.2	Legend for statistical parameter plots of bending stress	33
5.3	Bending stress for level flight group sorted by average steady stress	34
6.1	Frequency response of stabilator during level flight	39
6.2	Relevant failure modes of a lug: tension and shear tear out	41
6.3	Cross-sections showing dimensions of cracked lug	42
A1	Horizontal stabilator	52
A2	Top skin of the horizontal stabilator	53
A3	UH-60 (?) top skin of the horizontal stabilator	54
A4	Lugs from forward spar of stabilator's wing panel	55
A5	Forward spar of the port side stabilator	56
A6	Aft spar of the port side stabilator	57
A7	UH-60 (?) aft spar of the port side stabilator	58
A8	Bottom cap of the aft stabilator spar	59
A9	Rib of stabilator at BL 28	60
A10	Rib of stabilator at BL 9	61
A11	Rib of stabilator at BL 9, including view of lugs	62
A12	Lugs from aft spar of stabilator's wing panel	63
A13	Rib of stabilator at BL 6.75 (centre-box section)	64
A14	Stabilator attaching lug (centre-box section)	65
A15	Stabilator beam at BL 5.40 (centre-box section)	66
A16	Centre-box attachment for forward spars (Sheet 2)	67

A17	Centre-box attachment for forward spars (Sheet 5)	68
C1	Mathematica code for stress plots, Page 1.	76
C2	Mathematica code for stress plots, Page 2.	77
C3	Mathematica code for stress plots, Page 3.	78
C4	Mathematica code for stress plots, Page 4.	79
C5	Mathematica code for stress plots, Page 5.	80
C6	Mathematica code for stress plots, Page 6.	81
C7	Mathematica code for stress plots, Page 7.	82
D1	Autos group bending stress (sorted by average steady stress)	85
D2	Climb group bending stress (sorted by average steady stress)	86
D3	Hover group bending stress (sorted by average steady stress)	87
D4	Level flight group bending stress (sorted by average steady stress)	88
D5	Miscellaneous group bending stress (sorted by average steady stress)	89
D6	Reversals group bending stress (sorted by average steady stress)	90
D7	Pullouts group bending stress (sorted by average steady stress)	91
D8	Side and rear flight group bending stress (sorted by average steady stress)	92
D9	Sideslip group bending stress (sorted by average steady stress)	93
D10	Symmetric pullouts group bending stress (sorted by average steady stress)	94
D11	Taxi group bending stress (sorted by average steady stress)	95
D12	Turns group bending stress (sorted by average steady stress)	96
D13	Autos group bending stress (partitioned into manoeuvres)	97
D14	Climb group bending stress (partitioned into manoeuvres)	98
D15	Hover group bending stress (partitioned into manoeuvres)	99
D16	Level flight group bending stress (partitioned into manoeuvres)	100
D17	Miscellaneous group bending stress (partitioned into manoeuvres)	101
D18	Reversals group bending stress (partitioned into manoeuvres)	102
D19	Rolling pullout group bending stress (partitioned into manoeuvres)	103
D20	Side and rear flight group bending stress (partitioned into manoeuvres)	104
D21	Sideslip group bending stress (partitioned into manoeuvres)	105
D22	Symmetric pullout group bending stress (partitioned into manoeuvres)	106
D23	Taxi group bending stress (partitioned into manoeuvres)	107

D24	Turns group bending stress (partitioned into manoeuvres)	108
E1	Frequency response of rolling pullout	110
E2	Frequency response of rough approach	111
E3	Mathematica code for frequency plots, Page 1.	112
E4	Mathematica code for frequency plots, Page 2.	113
E5	Mathematica code for frequency plots, Page 3.	114
E6	Mathematica code for frequency plots, Page 4.	115
F1	Calculating second moment of area for wing panel lugs	117
G1	Upper cracked lug tip with positions of sampling regions	120
G2	Estimate of crack growth rate from five regions	123

Tables

2.1	Heights of forward and aft stabilator spars	13
4.1	Comparing groupings used by King and Lombardo and this report	24
4.2	Ten statistical parameters used to reduce time-history of Flight Loads Survey	25
4.3	Comparison of statistical parameters obtained by GTRI and this report	26
B1	Autos group manoeuvres	69
B2	Climb group manoeuvres	69
B3	Hover group manoeuvres	70
B4	Level flight group manoeuvres	70
B5	Miscellaneous group manoeuvres	70
B6	Symmetric pullouts group manoeuvres	71
B7	Rolling pullouts group manoeuvres	72
B8	Reversal group manoeuvres	72
B9	Side and rearward flight group manoeuvres	73
B10	Sideslip group manoeuvres	73
B11	Taxi group manoeuvres	73
B12	Turns group manoeuvres	74
D1	Deleted runs due to lack of additional statistical information	84
G1	Coordinates of sampled striations from five regions	121
G2	Median of crack growth rate for sampled regions and aggregate	124

Notation

Roman Symbols

a	crack length
A_{*i}	cross-sectional area of i th rectangular region (where the subscript “*” denotes either “a” or “f” respectively for aft or forward spar)
A_ℓ	cross-sectional area of cracked lug
C	coefficient in law for simple crack growth rate
F_{tu}	tensile ultimate strength
F_{ty}	tensile yield strength
\bar{h}	distance from neutral axis to top of beam
\bar{h}_a	height of half the aft spar
\bar{h}_f	height of half the forward spar
H	horizontal load
\mathcal{H}	frequency response function
H_{ai}	horizontal load on i th rectangular region of aft spar
H_{fi}	horizontal load on i th rectangular region of forward spar
H_u	ultimate horizontal load of lug
i	counting variable for crack striations
i	counting variable for enumeration of run number
\hat{i}	imaginary unit vector (that is, $\sqrt{-1}$)
I	second moment of area
j	counting variable used in Fourier transform (time domain)
k	counting variable used in Fourier transform (frequency domain)
K_t	stress concentration factor
ΔK	range of stress intensity factor
L	length of stabilator spar
m	characteristic slope for curve of crack growth rate
M	bending moment for free-body diagram
M_g	bending moment at gauge
M_r	bending moment at root
M_r^*	bending moment at root, not including lift between gauge and root
n	number of points in time-history vector for Fourier transform
N	loading cycles
N_f	cycles to fatigue failure
p	lifting distribution acting on stabilator's spar
P	maximum of elliptic lifting distribution
R	stress ratio (for use in cycles to failure equation)
s	direct stress measurement
$s_{0\%}$	minimum (0th percentile) of directly measured stress
$s_{5\%}$	5th percentile of directly measured stress
$s_{95\%}$	95th percentile of directly measured stress
$s_{100\%}$	maximum (100th percentile) of directly measured stress
S_1	turning point at start of loading cycle
S_2	turning point at end of loading cycle
S_{eq}	equivalent stress (for use in cycles to failure equation)

notation continued on next page ...

... notation continued from previous page

S_{\max}	maximum stress (for use in cycles to failure equation)
S_{\min}	minimum stress (for use in cycles to failure equation)
\mathbf{u}	vector containing time-history data for Fourier transform
\mathbf{v}	vector containing frequency data for Fourier transform
V	vertical force for free-body diagram
V_{\max}	maximum vertical force on stabilator wing panel
x	coordinate of crack growth striation
x	spanwise distance measured from stabilator's root
x_g	spanwise location of strain gauge
\mathcal{X}	frequency input function
y	coordinate of crack growth striation
y	vertical distance of a fibre from neutral axis
y_ℓ	distance between top and bottom lugs in spar
\mathcal{Y}	frequency output function
z	coordinate of crack growth striation

Greek Symbols

α	non-dimensional length coefficient (used in range of stress intensity factor)
γ	correction factor (compensates for lift ignored between gauge and root)
η	fillet height on forward spar's lug
λ_a	centroidal distance of aft spar's lug
λ_f	centroidal distance of fillet for forward spar's lug
ϑ	angle from horizontal made by lug of aft spar
ν	vibratory component of stress
$\nu_{95\%}$	95% percentile vibratory component of stress
ν_{avg}	average vibratory component of stress
ν_{\max}	maximum vibratory component of stress
ξ	distance from stabilator wing panel root
σ	steady component of stress
σ_a	bending stress on aft spar of stabilator
σ_{avg}	average steady component of stress
σ_f	bending stress on forward spar of stabilator
σ_g	bending stress at gauge
σ_∞	principal stress
σ_{\max}	maximum steady component of stress
σ_{\min}	minimum steady component of stress
σ_ℓ	stress at lug
ϕ_{hi}	frequency of worst-case loading
ϕ_{med}	frequency of typically high loading
χ	constant: first component of bending moment at gauge
ψ	constant: second component of bending moment at gauge
ω	frequency
ω_m	main rotor frequency
ω_t	tail rotor frequency

notation continued on next page ...

...notation continued from previous page

Miscellaneous Symbols (in the following notation a is a dummy variable)

\mathbf{a}	vector
a_{avg}	subscript for average
a_{a}	subscript for aft spar
a_{f}	subscript for forward spar
a_{g}	subscript for bending bridge gauge
a_{ℓ}	subscript for cracked lug
a_{r}	subscript for spar's root
a_{wp}	subscript denoting lugs from stabilator's wing panel
\mathbb{R}	real field

1 Introduction

Following flying operations on the 29th of June 2003, a potentially significant crack was found on a Seahawk helicopter. This crack occurred on the stabilator's centre-box (see Figure 1.1) and was found during a routine folding of the stabilator. Had this crack gone unnoticed further fractures would have developed. Due to these additional fractures, the loss of the stabilator mid-flight could have meant a loss of control for the helicopter—and the potential loss of the crew and the aircraft.

The Australian Defence Force's (ADF) response to this lug failure was guided by advice [17] from the Rotary Wing Section of the Director General Technical Airworthiness. This advice concluded that the damage was of a *fail safe* nature as intended by the original equipment manufacturer (which was the Sikorsky Aircraft Corporation). Hence the recommendation [17] was for a minor amendment of the inspection program to detect the unlikely fracture of this lug.

The work carried out in this report investigates the fatigue loading the lug would probably experience, and hence the possibility of this type of fatigue cracking occurring in other Seahawks. However, the primary intention is not to define an alternative fatigue life, but to explore a *methodology* for assessing the fatigue life of helicopter airframe structure, for which there are currently no robust methodologies. Furthermore, the development of

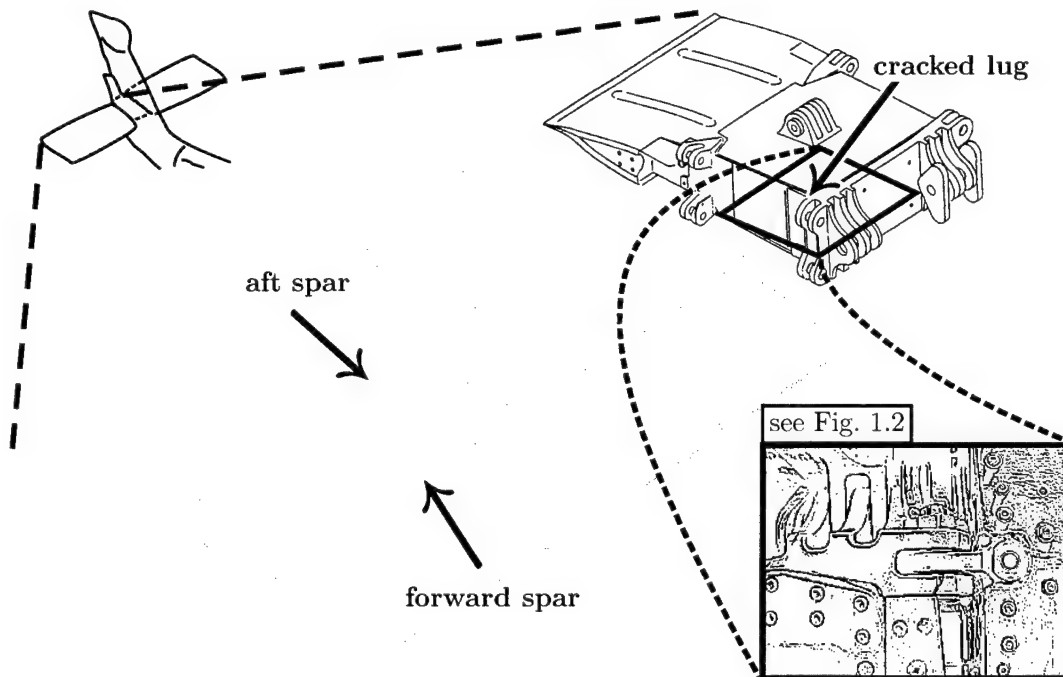


Figure 1.1: Line drawing of the starboard side stabilator and centre-box from the Seahawk's tail. An arrow points to the cracked lug, which is the aft portion of the clevis lug. This lug is located on the top starboard side of the forward spar. The two remaining arrows point to the forward and aft spars. (Drawings adapted from Black Hawk manuals [24, 25].)

this methodology will improve DSTO's *capability* in the fatigue life assessment of helicopter airframe structure. As a demonstrator, we develop this methodology using the lug failure in the Seahawk stabilator together with the extensive data that DSTO acquired from Flight Loads Survey [3] of the Black Hawk.

The fatigue characteristics of a Seahawk lug are investigated using simplified procedures. First, a brief description of this cracked lug is given, the philosophy behind the fatigue analysis explained, and the assumptions made throughout this report summarised. In order to calculate the stress on this lug, the geometry of the loading spars and gauge locations are then given. The horizontal and vertical loading on these spars are then approximated using skin bending stresses. These bending stresses were obtained from the Flight Loads Survey carried out on a Black Hawk helicopter. The loading frequency and the stress on the lug are then estimated, and the fatigue properties of the cracked lug approximated. The final section summarises the finding made within this report.

1.1 Description of Cracked Lug and Design Review

The crack occurred in the receiving clevis lug (only the aft portion) on the starboard side of the stabilator centre-box. (For brevity, this lug will be called the *cracked lug* in this report.) From new, this lug component had experienced a mere 402 flight hours, which is below the more than 3000 flight hours the fleet leader has accumulated. Figure 1.1 shows the crack in relation to the tail of the aircraft, progressively zooming-in on the cracked lug. The centre-box and starboard stabilator are shown in this figure, and an arrow marks the cracked lug.

As can be seen from Figure 1.1, the cracked lug is part of a clevis, which is one of a set of four clevis joints that attach the outboard portion of the stabilators to the centre box. This design has a level of inherent damage tolerance because the failure of any single lug will not result in the loss of the stabilator wing. The clevis design maintains independent and redundant load paths [1, p. H-13] by preventing cracks in one lug from propagating to the other lugs. The design of the centre-box lugs considered only static loads, that is, fatigue loading was *not* considered.

Figure 1.2 shows a top view of the centre-box (bottom left) attached to the starboard stabilator (right) and tail pylon (top left). The white arrow marks the cracked lug and the hollow arrow to the left of this photograph defines the forward direction. Both sides of the lug's aft portion were completely cracked and only the lug's bolt was holding the outer tip of the lug in place.

A DSTO minute by Byrnes [5] and a DSTO investigation report, also by Byrnes [6], describe this cracking problem further. Byrnes' forensic investigation report also details the folding property of the Seahawk's stabilator and provides more detailed photographs of the lug fracture.

Figure 1.3 shows the centre-box detached from the stabilator, and a red circle highlights the cracked lug. A close-up of the lug's broken portion is shown along with a ruler on the bottom photograph of this figure. This bottom photograph shows striation marks, which are typical of fatigue cracking (see Byrnes [6]).

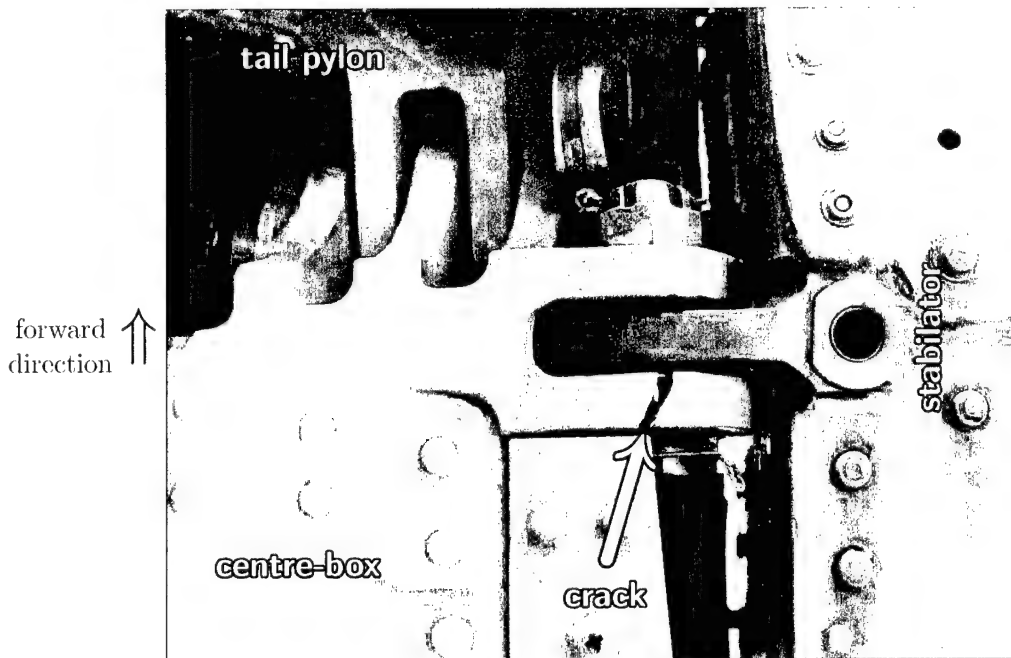


Figure 1.2: The aft portion of the clevis lug (centre of photograph) has completely cracked. only the bolt is holding the outer tip of the lug in place. Portions of the stabilator (right), tail pylon (top left), and centre-box (bottom left) are shown in this photo. (Photograph courtesy of Jamie Edwards).

The stabilator assembly, composed of the stabilator wing panels and centre-box, was fatigue tested by Sikorsky.¹ According to Sikorsky [1], *steel lugs* attach the wing panels to the centre-box; it is unclear whether this “steel” reference is simply a typing error. If the testing was indeed conducted on a stabilator with steel lugs, then the aluminium² centre-box lugs found in the ADF’s Seahawks may *not* have been tested by Sikorsky for fatigue.

The crack initiation phase of Sikorsky’s fatigue testing was conducted at a constant vibratory stress determined from high-speed level flight. When a crack was detected in the centre-box, the load was reduced to a conservative loading simulation. One hour of this loading simulation consisted of 62 000 cycles of flight loading (namely, high-speed level flight) followed by 4 ground-air-ground (GAG) cycles. Sikorsky define a GAG cycle as the maximum single stress cycle (steady plus vibratory) occurring in a complete flight. To assess damage tolerance, the testing continued beyond crack detection until the stabilator was no longer able to sustain the testing load.

For helicopters, a working fatigue curve is obtained by reducing the mean fatigue curve, which is achieved by shifting the curve down and to the left on the S-N plane. The down-shift is obtained by multiplying the stresses, on the mean fatigue curve, by a reducing

¹See in particular Section H, pages 8–13, of this Sikorsky report [1].

²For a discussion of the material properties of the cracked lug see Section 5.1 on page 28.

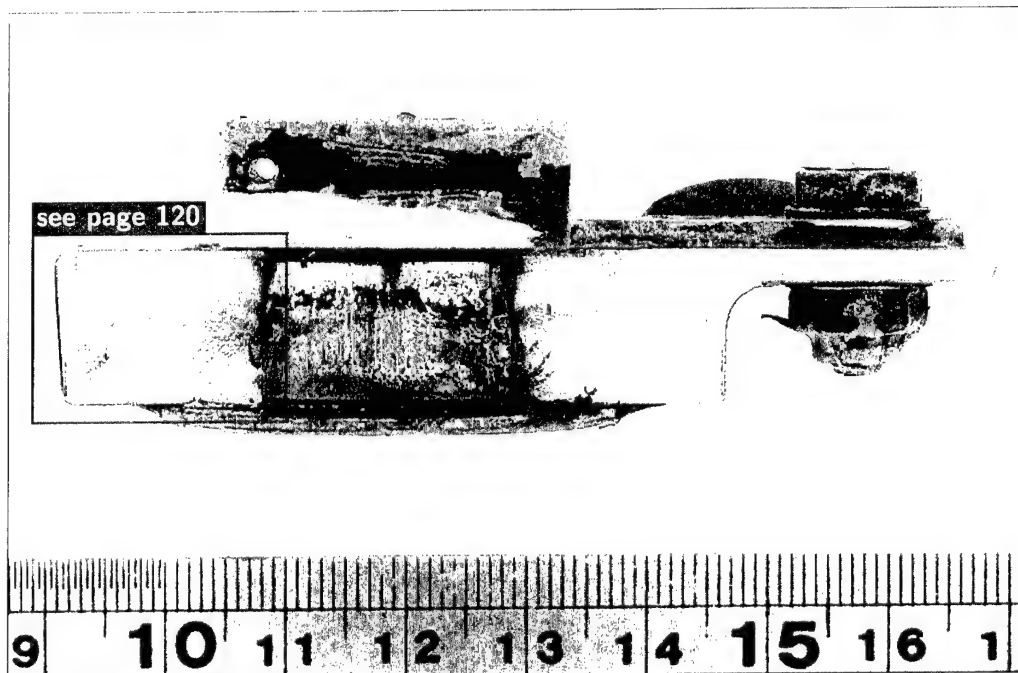


Figure 1.3: *Stabilator centre-box (top photograph) and close-up of lug's broken portion (bottom photograph). In the stabilator photograph, the red circle highlights the cracked lug. In the close-up photograph, the ruler's units are centimetres. (Photographs courtesy of Rohan Byrnes.)*

factor. Similarly, the left-shift is obtained by multiplying the cycles to failure, on the mean fatigue curve, by a different reducing factor. The results described in the following two paragraphs use multiplying factors of:

- 0.61 and 0.80 for the *down-shift* and
- 1/5 and 1/3 for the *left-shift*, respectively.

For further details about how to develop a reduced (or working) fatigue curve from the mean fatigue curve see, for example, Lombardo [18, p. 32].

In the stabilator's wing panels, it was the forward spar that failed in this fatigue test. This forward spar (on the right-hand panel) failed in cracking without chafing. The stabilator wing panels were given component retirement lives of 1600 hours and 18 000 hours for respectively a 0.61 and 0.80 reduction of the mean fatigue curve. The damage tolerant testing showed that after this spar cracking was detected, the stabilator could endure a further 250 hours of equivalent mission flight before failure.

In the centre-box, it was a rivet hole on the top flange of the aft fitting that cracked. This rivet hole was located on the spar that connects the left and right aft lugs of the centre-box. The centre-box was given component retirement lives of 660 hours and 6100 hours for respectively a 0.61 and 0.80 reduction of the mean fatigue curve. The damage tolerant testing showed that after this rivet crack was detected, the stabilator could endure a further 160 hours of equivalent mission flight before failure.

Sikorsky concluded that the fail-safety of the stabilator had been demonstrated, and recommended the stabilator assembly be replaced on-condition [1].

1.2 Philosophy behind Fatigue Analysis

The analysis carried out in this report involved the use of several *quick-and-dirty* methods, which required several assumptions. The nature of this analysis was made necessary by either: (i) a lack of information or (ii) a requirement for a timely solution. The lack of information meant that there was often no benefit in using a more sophisticated or complicated analysis.

As a first order approximation, we were trying to assess the *worst-case* and *best-case* scenarios (which are defined below) for the fatigue cracking of the lug.

Worst-Case Scenario: assumes the helicopter is continuously operated in a "harsh" manner. If the estimated stresses experienced by the lug under this harsh scenario were below the lug's run-out stress, then we could effectively rule out fatigue cracking as a problem in the centre-box lugs of *ordinary* Seahawk stabilators. This scenario is essentially a *bound from above on stress*.

Best-Case Scenario: assumes the helicopter is continuously operated in a "gentle" manner. If the estimated stresses experienced by the lug were significant in terms of fatigue, then we could conjecture that centre-box lugs in *ordinary* Seahawk stabilators might be at risk from fatigue. This scenario is essentially a *bound from below on stress*.

It is important to note at this stage that *no conclusion* (or at least only a tentative conclusion) could be drawn if we obtained either of the two opposing scenarios; namely, (i) high stresses under the harsh operations assumption or (ii) low stresses under the gentle operations assumption. These two scenarios will be termed the *null conclusions*.

To explain these null conclusions more concretely, let us consider the first case of high stresses under harsh operations. If we obtained this null conclusion, then we could not be sure whether these high stresses were due to (i) a possible operating environment or (ii) an over-pessimistic view of the operating environment. In contrast, we could confidently say that fatigue was not a problem if we obtained low stresses under the worst-case scenario (namely, harsh operations). An analogous argument can be made for the best-case scenario and its associated null conclusion.


To summarise, this quick analysis was really a process of elimination rather than a complete solution. Throughout this report suggested improvements to the analysis are made; along with some comments on the added complexity required and possible accuracy gained in using these suggested improvements.

In addition to these extreme cases, an intermediate loading case is also analysed. This intermediate-case estimates the lug loading by using high loads from a level flight manoeuvre, in other words, a typical high-loading case. Unlike the worst-case, this intermediate-case is *not necessarily* conservative, and hence it is used more as a check on the level of conservatism inherent in the worst-case scenario than as a solution in its own right.

1.3 Synopsis of Assumptions

In this section we summarise the assumptions made during the analysis of the lug cracking problem. The assumptions in this report were made for one of two reasons:

- *Lack of information:* There was insufficient information to carry out a full analysis or the available information was ambiguous.
- *Expediency of the solution:* In order to obtain a quick-and-dirty solution a full analysis was often omitted, and instead a simplified analysis was undertaken.

In this report, the symbol  is printed in the left margin to emphasise the introduction of an assumption.

The calculations in this report use dimensions of the load bearing components obtained from Sikorsky maintenance drawings (see Appendix A starting on page 51). In using these Sikorsky drawings an implicit assumption was made:



Assumption 1 *The horizontal stabilators of the Seahawk are identical to those of the Black Hawk. Or at least from a loading perspective, the structural information obtained from the Sikorsky drawings are a good representation of the stabilator structure found on the Seahawk.*

This assumption was made because only Black Hawk (and not Seahawk) component drawings were readily available. The Sikorsky maintenance drawings of the Black Hawk available at DSTO appear to be a mixed bag of drawings. For example, there are two drawings of the aft stabilator spar, compare Figure A6 with Figure A7 (on pages 57 and 58, respectively). These two drawings, of what should be the same component, are completely different: the *angled* aft spar in Figure A7 probably belongs to the UH-60 as compared to the *straight* aft spar of Figure A6. Similarly, compare the top stabilator views in Figures A2 and A3 (on pages 53 and 54, respectively).

The specific assumptions made throughout this report are summarised below. More detailed information on each of these assumptions is given on the page where the assumption is first introduced (references to these pages are given next to the assumption number).

The following assumptions were made during the calculation of lug stress:

- *Assumption 2 (p. 8)*: how the bending bridges on the stabilator are mounted.
- *Assumption 3 (p. 10)*: the dimensions of the spar caps in the stabilator are constant.
- *Assumption 4 (p. 12)*: the dimensions of spars in the stabilator are estimated.
- *Assumption 5 (p. 14)*: torsional and chordwise loads in the stabilator are ignored.
- *Assumption 6 (p. 16)*: the lifting load on the stabilator is elliptic.
- *Assumption 7 (p. 23)*: manoeuvres within a group are similar.
- *Assumption 8 (p. 28)*: the fatigue properties of 7075 aluminium alloy with T6 and T7 temperings are similar.
- *Assumption 9 (p. 29)*: the cycles to failure equation given by the military handbook for metallic materials can be extrapolated.
- *Assumption 10 (p. 31)*: the stabilator's percentile stresses characterise fatigue loading in the cracked lug.
- *Assumption 11 (p. 33)*: level flight stresses are typical all the time.
- *Assumption 12 (p. 34)*: all manoeuvres consume the same fraction of usage time and experience the same stress.
- *Assumption 13 (p. 35)*: the steady and vibratory percentile stresses yield conservative estimates of fatigue.
- *Assumption 14 (p. 36)*: the Flight Loads Survey is representative of the in-service flight loads.
- *Assumption 15 (p. 37)*: the typical loading frequency dominates fatigue usage.
- *Assumption 16 (p. 37)*: all manoeuvres exhibit the typical loading frequency.

Not all of these assumptions were used for the three loading cases (worst-, best-, and intermediate-cases). For example, Assumption 11 is not required for the worst-case scenario.

2 Stabilator's Geometry and Gauge Locations

In order to determine the vertical and horizontal loading on the cracked lug we must know the loading on the stabilator. The only information readily available were strain gauge and accelerometer measurements from the Flight Loads Survey on the Black Hawk. The strain gauge information came in the form of bending stress on the upper and lower skins of the stabilator (directly above and below the forward and aft spars). The spars' geometries were needed to convert this bending stress to a lug loading. Hence this section provides information on both the gauge locations and the spars' geometries.

2.1 Stabilator Strain Gauge and Accelerometer Locations during Flight Loads Survey

During the Flight Loads Survey [3] carried out on a Black Hawk, five bending stresses were measured on the both the port and starboard stabilators [8, pp. 76–8]. For each of these ten stabilator locations (five on the port side and five on the starboard side), four strain gauges were configured as a full-bending bridge. In total, forty strain gauges were mounted on the stabilators (4 gauges \times 5 locations \times 2 stabilators = 40 gauges). Figure 2.1 shows where these five bending bridges were mounted for the port side stabilator.

Friend [8] does *not* state how these bending bridges were mounted, and so we make the following assumption:



Assumption 2 *Each bending bridge mounted on the stabilator consisted of four strain gauges, two gauges on the forward spar and two gauges on the aft spar. For both the forward and aft spars, a strain gauge was mounted on both the top and bottom skins directly above and below each spar. The bending stresses on the front and aft spars (obtained from these strain gauges) were then combined to obtain an average stabilator bending at a particular butt line. A positive bending measurement implies a compressive stress on the top skin.*

Figure 2.1 shows the five butt line locations (note that distances in this figure are shown from the inboard edge of the stabilator, which is 9.00" from the helicopter's centreline). We have assumed the convention that a positive bending measurement implies a compressive stress on the stabilator's top skin; and hence a compressive load on the cracked lug.

In Friend's report [8], these bending bridges on the left- and right-hand sides were respectively given the mnemonics STBNBM $_i$ L and STBNBM $_i$ R, where $i = 0, 1, 2, 3, 4$ as shown in Figure 2.1.

In addition to these strain gauges, there were also four accelerometers mounted on the stabilator and three strain gauges mounted on the stabilator's centre-box.

The four accelerometers (two on each side of the stabilator) were mounted on the forward spar of the stabilator approximately 37" and 74" from the inboard edge [8, pp. 90–1], see Figure 2.1. In Friend's report, these accelerometers on the left- and right-hand sides were respectively given the mnemonics VSTAB $_x$ L and VSTAB $_x$ R, where $x = T, M$ as shown in Figure 2.1.

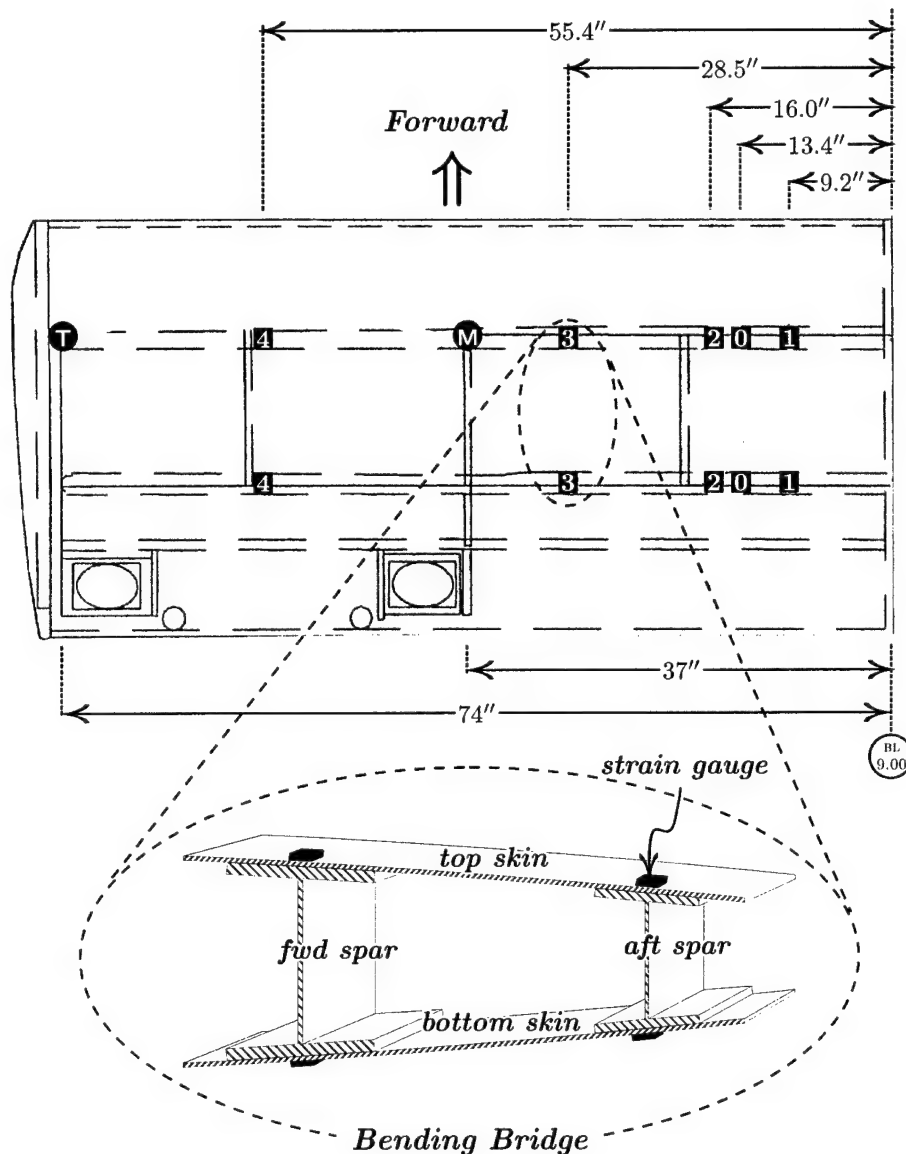


Figure 2.1: Top view of the port side stabilator showing the location of the strain gauges \blacksquare (for $i = 0, 1, 2, 3, 4$) and accelerometers \otimes (for $x = T, M$) mounted during the Flight Loads Survey. Distances shown are from the inboard edge of the stabilator, which is 9.00" from the helicopter's centreline. The schematic of the zoomed section represents a perpendicular (that is, chordwise) cross-section of the stabilator. This cross-section shows the assumed location of the strain gauges within a bending bridge. (Stabilator drawing adapted from a GTRI report [8, p. 78].)

The three centre-box strain gauges were mounted in a 45° rosette pattern on the horizontal stabilator. More specifically these strain gauges were mounted on the forward spar's forward face of the centre-box. In Friend's report [8, pp. 76–7], these strain gauges were given the mnemonics STBCBR1 y , where $y = A, B$, and C respectively represent the gauges aligned 0°, 45°, and 90° from the vertical. These gauges are *not* shown in Figure 2.1 because the centre-box is not included in this illustration.

2.2 Geometry of Forward and Aft Stabilator Spars

The approximate dimensions of the forward and aft spars were obtained from Sikorsky maintenance drawings. Figure 2.2 shows drawings of the forward and aft spars:

- Box A shows the middle rib (along with the forward and aft spars) of the horizontal stabilator at BL 28. This box is a zoomed section from Sikorsky drawing 70201-07052 grid reference D8, see Figure A9 (on page 60) for the complete drawing.
- Box B shows the dimensions of the top cap from the forward spar at BL 9. This box is a zoomed section from Sikorsky drawings 70202-07051 grid reference K21, see Figure A5 (on page 56) for the complete drawing.
- Box C shows the bottom cap of the aft spar. This box is a zoomed section from Sikorsky drawings 70202-27001 grid reference B5, see Figure A8 (on page 59) for the complete drawing.

The drawings shown in Figures A4 and A10 (on pages 55 and 61, respectively) may also be of interest.

It was unclear from these drawings how the spar cap dimensions changed with spanwise location, and so we make the following assumption:



Assumption 3 *In both the forward and aft spars of the horizontal stabilator, the cross-sectional dimensions of the spar caps remained constant with spanwise location.*

This assumption was made for expediency, because from the forward and aft spar drawings these caps *do* taper. In particular, the caps appear to taper in at least the following ways: (i) the width of the spar flanges taper, (ii) the thickness of the spar flanges taper, (iii) the height of the cap's web tapers, and (iv) the boron composite (bonded to the caps) tapers. For additional details on cap tapering see Figures A5 and A6 (on pages 56 and 57, respectively).

What are the implications of Assumption 3? Given that we are using the cap dimensions obtained from BL 9.00 (see Assumption 4 below), if the caps were tapered then the true stresses on the lug would be lower than the stress estimations obtained in this report. The reason the stress would be lower is that the cross-sectional area of the caps would be smaller, which would reduce the estimated tensile stress (see Section 3.3 for more details). Given that we are primarily chasing a worst-case scenario, this over-estimation of stress is fortuitous (but would probably not be significant anyway).

Using the information in Figure 2.2, the caps were assumed to have the following dimensions (obtained from the top cap of the forward spar at BL 9.00):

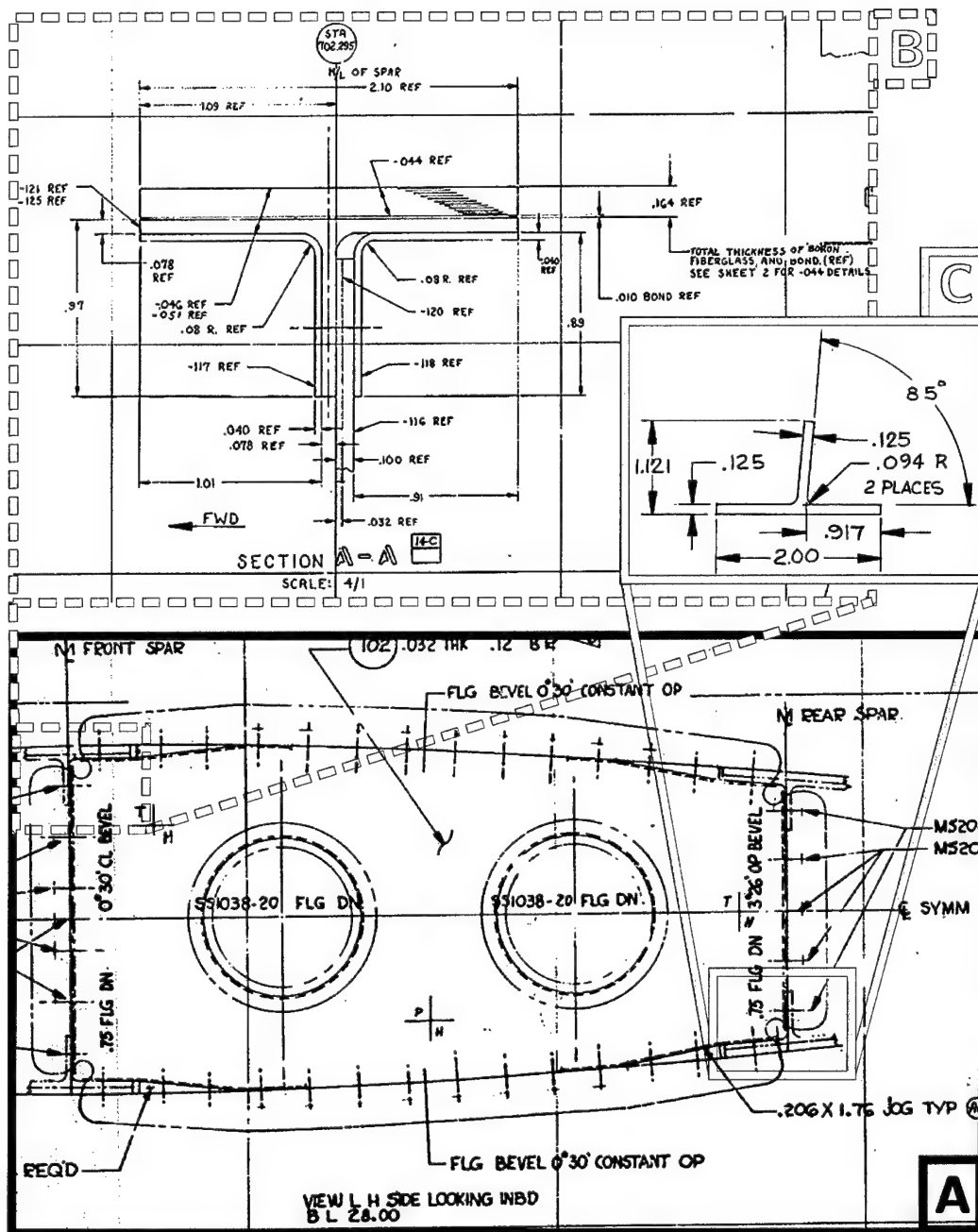


Figure 2.2: Caps of both the forward and aft spars on the horizontal stabilator. Box A shows the middle rib (along with the forward and aft spars) at BL 28. Box B shows the top cap of the forward spar at BL 9. Box C shows the bottom cap of the aft spar at BL 17.

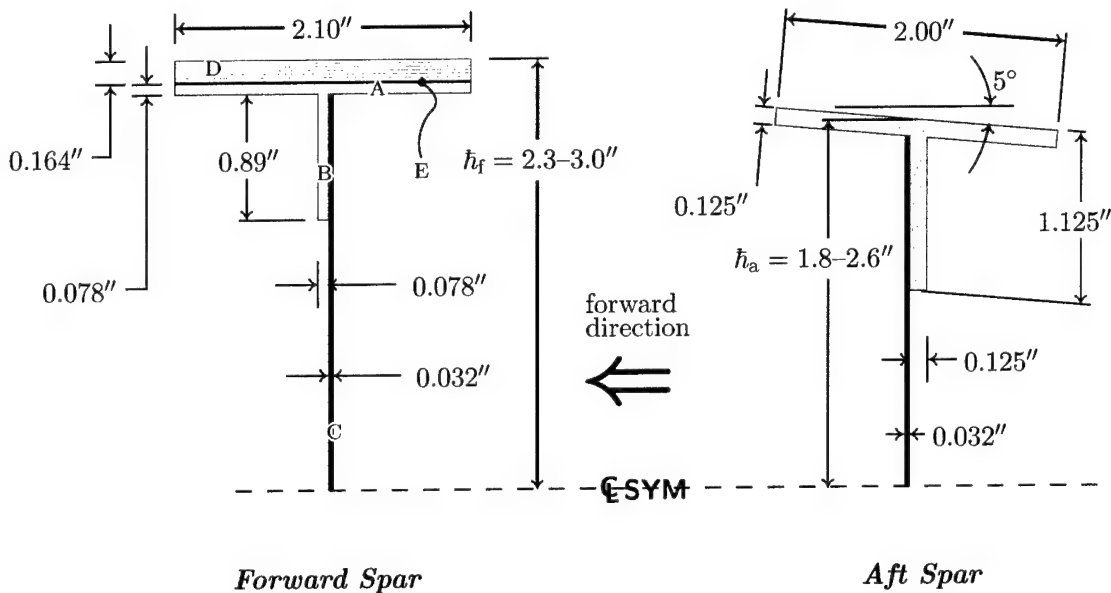


Figure 2.3: Estimated dimensions of the forward and aft spars. The heights of the two spars are given as a range, the maximum and minimum represents the heights at BL 9 and BL 66, respectively. The labelled components of the forward spar are: (A) the cap's flange, (B) the cap's web, (C) the spar's web, (D) the boron composite stiffener, and (E) the adhesive bond.



Assumption 4 The dimensions of the forward and aft spars are as shown in Figures 2.3. Both the forward and aft spars have vertical symmetry about the shown centreline. The thickness of the adhesive bond (which is 0.010") was absorbed into the thickness of the boron composite stiffener. The fillets between the cap's web and flange were ignored. The top of the spar's web is assumed to be flush with the bottom of the cap's flange. The web of the aft spar is the same thickness as the web of the forward spar. The skins of the stabilators were ignored. The heights of both spars vary linearly with spanwise location.

The dimensions shown in Figure 2.3 were obtained from the spar sections shown in Figure 2.2.

Due to a lack of information, the aft spar's web was assumed to be the same thickness as the forward spar's web. Ignoring the fillets and skins reduced the cross-sectional area, and hence we obtain an over-estimation of the true stress. Conversely, increasing the height of the spar's web (so that it's flush with the flange) increases the cross-sectional area marginally. However, the overall area should still decrease because the skin and fillets were ignored, and hence we end up with a conservative estimate of stress.

It was unclear from the available drawings whether the aft spar also had a boron composite stiffener attached to it. Given that the aft spar was considerably thicker than the forward spar, we assumed there was no additional stiffener on top of the aft spar.

The cap height of the aft spar shown in Figures 2.2 (which is 1.121") is slightly different to the corresponding length shown in Figure 2.3 (which is 1.125"). This difference is due to the 5° declination of the cap, which increases this length by 0.38%.

The heights of the spars were measured from the forward and aft spar drawings (see Figures A5 and A6 on pages 56 and 57, respectively). Only two spar heights were taken on each of these drawings: one at BL 9 and the other at BL 66. Both these spar drawings appear to suggest that the spar's height tapers linearly from the stabilators inboard edge (at BL 9) to its outboard edge (at BL 82). Thus using the linearly tapering conjecture (made in Assumption 4), we can calculate the spar heights at the five bending bridge locations (see Table 2.1).

Table 2.1: *Stabilator spar heights (both forward and aft spars) at the five bending bridge locations.*

Bending Bridge Number		-	0	1	2	3	4	-
Butt Line (inch)		9.00	22.4	18.2	25.0	37.5	64.4	66.0
$2h_f =$	Forward spar height (inch)	6.1	5.8	5.9	5.7	5.4	4.7	4.7
$2h_a =$	Aft spar height (inch)	5.2	4.8	4.9	4.8	4.4	3.6	3.6

3 Stabilator Loading

In this section the vertical and spanwise loading on the spars is approximated using the bending stress information available from the Flight Loads Survey. First we make some assumptions about the external loading on the stabilator. The vertical force on the stabilator is then estimated assuming a particular lifting distribution, which is scaled according to the stabilator's bending stress. Finally, the horizontal loading (in the spanwise direction) is estimated using both the stabilator's bending stress and the vertical loading.

3.1 External Loads on Stabilator

The external loading on the stabilator spars is due solely to aerodynamic forces acting on the stabilator's skin. Hence, the external forces on the stabilator act in both the vertical (due to lift) and chordwise (due to drag) directions.

Due to the limited amount of stress information, we make several assumptions about how the load is transmitted through the stabilator.



Assumption 5 *Both the forward and aft spars experience only vertical loading through their respective shear centres (that is, there is no drag load). This vertical loading is evenly distributed between the two spars. There is no secondary structure (such as ribs) between the two spars. The skins do not take any loading (not even in shear).*

Normally the stabilator would act as a shear box, however, due to the limited amount of information available, there is no way to resolve the different types of loading. Drag (that is, chordwise loading) on the stabilator was also ignored. For shapes with aerofoil cross-sections, and provided that the angle of attack is not too far from zero, the drag is typically an order of magnitude lower than lift (see, for example, Gerhart and Gross [10, p. 548]). The design loading used by Sikorsky [9] supports this order of magnitude assumption, so ignoring drag is a reasonable assumption. In essence, Assumption 5 says that any loading experienced by the bending bridges mounted on the stabilator are solely due to the independent vertical loading experienced by each spar.

Unfortunately, using only the Flight Loads Survey measurements very little (if any) accuracy can be gained by refining Assumption 5. We saw in Assumption 2 (on page 8) that the bending stress from the Flight Loads Survey is an average of the bending stresses at the forward and aft spars. There is no way we can deconvolute this average stress into the individual bending stresses on the forward and aft spars, and hence no overall accuracy is gained from the refinement of Assumption 5.

Consider the spars as determinant structures, which is itself a mild assumption because the upper and lower receiving lugs would make the spar statically indeterminant. In particular, we choose to model them as simply supported beams. Drawing a free-body diagram through one of the gauges results in the diagram shown in Figure 3.1. The cross-section of the beam, highlighted by the dashed circle, shows the profile of the tensile stress resulting from the bending moment. The three-dimensional cross-section (on the right-hand side of Figure 3.1) shows this stress profile in perspective. Note that the vertical force V does *not* affect the bending bridge, but we will need it when calculating the vertical loading on the lugs.

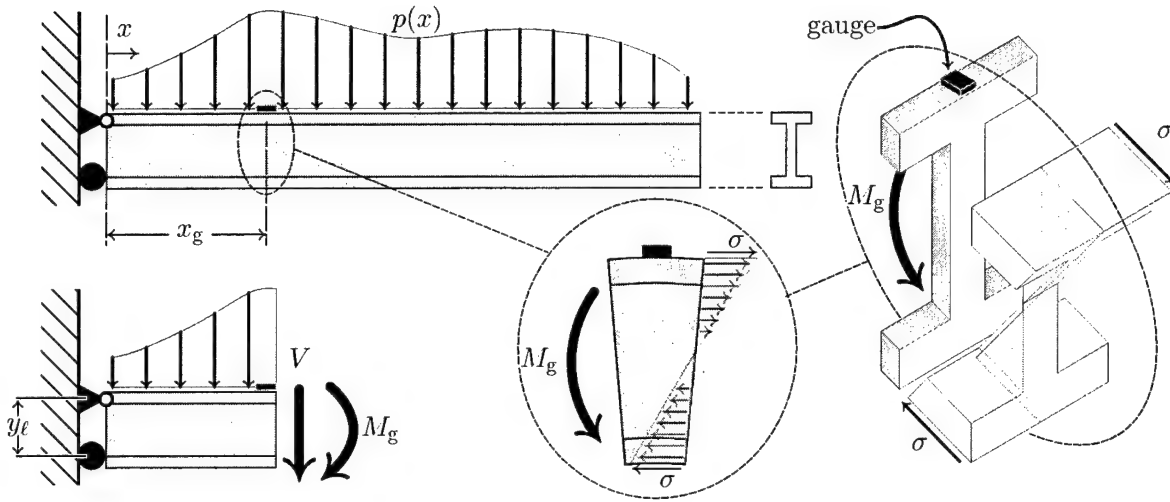


Figure 3.1: Using a free-body diagram to calculate the loads on the spar's cross-section. The free-body slice is taken at $x = x_g$, which is the location of the strain gauge. The distributed load $p(x)$ is unknown, and is the only external load the spar experiences.

3.2 Vertical Load on Stabilator Spars

In this section we estimate the vertical loading using the stress on a bending bridge and an assumed lifting distribution for the stabilator.

Using a bending moment to determine the vertical load results in a non-unique problem. In other words, an infinite number of different loading distributions could produce the same bending moment at a particular location.

Consider, for example, a simple horizontal cantilever beam with two vertical loads. Let us say that these two loads, f_1 and f_2 (located 1.1 m and 2.5 m, respectively, from the fixed end), produce a 7.8 N m bending moment at the root. In mathematical notation, we need to solve for the loads f_1 and f_2 in the equation $1.1f_1 + 2.5f_2 = 7.8$. In other words, we are solving for two unknowns with one equation, which results in an infinite number of solutions. Even worse, changing the location of these vertical loads would still yield sensible solutions; for example, there exist pairs (f_1, f_2) such that $0.3f_1 + 1.5f_2 = 7.8$. Distributed loadings are even more indeterminate³ than this simple point load example.

Choosing a particular loading distribution *shape* results in a unique vertical load—but there is little evidence to validate this choice, especially in an airflow subject to disturbance from main rotor downwash. Elliptic loading distributions are often used in simple aerofoil theory (see, for example, Houghton and Carruthers [13]), which is why we make the following assumption:

³This greater indeterminacy is more easily seen if a distributed load is modelled as a large number of point loads. This model results in the equation $\sum_{i=1}^n x_i f_i = M$, where n is the number of point loads f_i at locations x_i , and M is the resulting bending moment. The degree of indeterminacy is given by the number of point loads n . Letting n tend to infinity and the $\max |x_i - x_j| \rightarrow 0$ for any $1 \leq i, j \leq n$, produces a distributed load—together with an infinite degree of indeterminacy.



Assumption 6 *The vertical loading acting on each spar is elliptic, and is given by $p(x) = P\sqrt{1 - (x/L)^2}$, where x is the spanwise location along the spar, P is a load scaling constant, and L is the spar's length.*

Sikorsky appears to also use an elliptic loading distribution in their design analysis [9, Fig. 7].

Both the forward and aft spars begin at BL 9 and end at approximately BL 83. Thus the spar length is $L = 74$ inches and x is measured from the inboard edge of the stabilator at BL 9 (that is, $x = 0$ at BL 9 and $x = 74$ at BL 83). The unknown constant P not only scales the elliptic loading, but is also this loading's maximum, which occurs at the spar's root.

One way to improve Assumption 6 is by using the bending stresses at all five stabilator locations. The elliptic lifting distribution in Assumption 6 (or a more complex distribution) could then be scaled based on some weighted combination of these five bending stresses. For expediency we avoided this weighted combination approach.

Referring to Figure 3.1, the bending moment at the gauge location is given by

$$M_g = \int_{x_g}^L (x - x_g)p(x) dx, \quad (3.1)$$

where x_g is the distance of the bending bridge gauge from the spar's root. Substitute the elliptic loading distribution given by Assumption 6 into Equation (3.1); then solving the integral gives

$$M_g = P(\chi - \psi), \quad (3.2)$$

where the constants χ and ψ are given by

$$\chi = \frac{1}{6L} (2L^2 + x_g^2) \sqrt{L^2 - x_g^2} \quad \text{and} \quad \psi = \frac{x_g L}{4} \left[\pi - 2 \tan^{-1} \left(\frac{x_g}{\sqrt{L^2 - x_g^2}} \right) \right]. \quad (3.3)$$

As a simple check of this equation, consider the case where the gauge is located at the root of the spar, that is, $x_g = 0$. The vertical loading (that is, area of the quarter-ellipse) is $\pi PL/4$ and the horizontal centroid (of the quarter-ellipse) occurs at a distance $4L/(3\pi)$ from the root. Multiplying the loading by the centroidal distance gives the bending moment at the root $M_r = PL^2/3$, which is the same solution that Equation (3.2) together with Equation (3.3) gives.

Using simple beam bending theory (see, for example, Hall [11] or Roark [28]), the fibre stress at a point that is a height y above the beam's neutral axis is given by

$$\sigma = \frac{My}{I}, \quad (3.4)$$

where M is the bending moment on and I is the second moment-of-area of the beam's cross-sectional face passing through the point. This linear (with height) stress profile is shown in Figure 3.1, along with the resulting stress profile (shown in perspective) on the beam's cross-section.

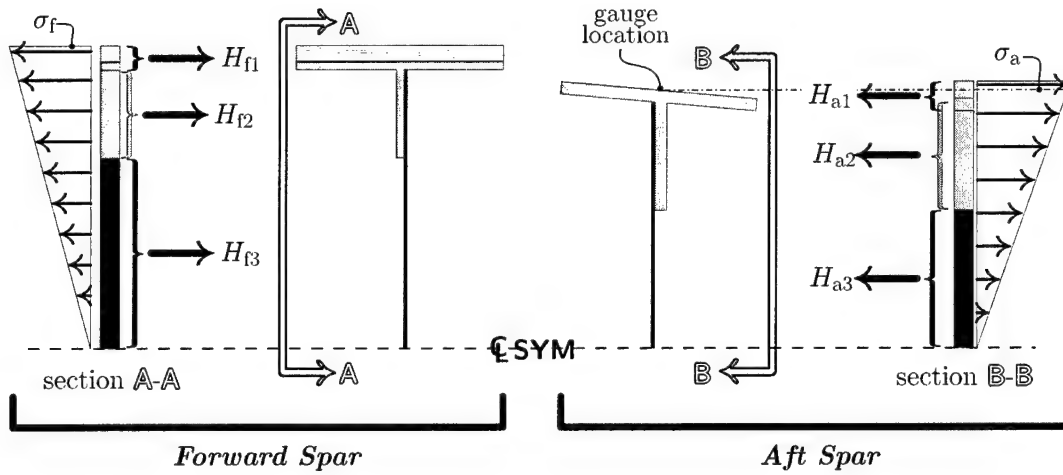


Figure 3.2: Horizontal (spanwise) loading, a product of stress and area.

Use Equation (3.4) to substitute the stress measured at the bending bridge σ_g for the bending moment M_g . Then for a given bending moment M_g we can solve Equation (3.2) for the maximum load on the spar

$$P = \frac{\sigma_g I}{\bar{h}(\chi - \psi)}, \quad (3.5)$$

where I is the spar's second moment of area and \bar{h} is the vertical distance from the spar's neutral axis to the skin (which is where the bending bridge is located).

The forward spar was partitioned into three rectangular regions (shown in Figure 3.2 by the curly braces) in order to calculate the second moment of area of (and later the horizontal load on) a particular cross-section. In the forward spar:

- the upper rectangular region contains the boron composite, the adhesive bond, and the cap's flange;
- the middle rectangular region contains the cap's web and part of the spar's web; and
- the lower rectangular region contains only the remainder of the spar's web.

A similar partitioning of the aft spar was needed to calculate the second moment of area on it. In the aft spar:

- the upper rectangular region contains only the cap's flange;
- the middle rectangular region contains the cap's web and part of the spar's web; and
- the lower rectangular region contains only the remainder of the spar's web.

Due to the 5° declination of the cap's flange, the upper and middle rectangular regions overlap. Again due to the declination, the maximum stress that the aft spar experiences

will be greater than the stress at the bending bridge gauge. In Figure 3.2, the gauge measuring stress is depicted as occurring 0.087" from the top of the spar, this length was obtained by simple geometry $2'' \times \sin(5^\circ) \div 2 = 0.087''$.

Using Roark [28] the second moment of area of a rectangular region about its centroid is given by $I = bd^3/12$, where b and d are the rectangle's width and height, respectively. The second moment of area for the three rectangular regions (defined in Figure 3.2) about their centroids are as follows.

For the forward spar

$$\begin{aligned} I_{f1} &= 2.48 \times 10^{-3} \text{ in}^4, \\ I_{f2} &= 6.46 \times 10^{-3} \text{ in}^4, \quad \text{and} \\ I_{f3} &= 0.032(h_f - 1.132)^3/12 \text{ in}^4, \end{aligned}$$

where h_f and h_a respectively denote *half* the height of the forward and aft spars, see Figure 2.3 on page 12. (Thus the values shown in Table 2.1 on page 13 represent $2h_f$ and $2h_a$.)

For the aft spar

$$\begin{aligned} I_{a1} &= 956 \times 10^{-6} \text{ in}^4, \\ I_{a2} &= 13.1 \times 10^{-3} \text{ in}^4, \quad \text{and} \\ I_{a3} &= 0.032(h_a - 0.125)^3/12 \text{ in}^4, \end{aligned}$$

where we have used the formula $I_\theta = bd(d^2 \cos^2 \theta + b^2 \sin^2 \theta)/12$ (see Roark [28]) to derive the second moment of area for rectangular Region 1 of the aft spar. This formula was required because Region 1 was aligned at a $\theta = 5^\circ$ declination to the horizontal axis.

The formula $I_x = I_l + Ay^2$ (see Roark [28]) relates the second moment of area about two axes separated by a perpendicular distance y . Using this formula, summing the three different regions, and doubling the result (to account for the lower half of the spars) gives the second moment of area for the *forward spar*

$$\begin{aligned} I_f &= 2 \left([2.48 \times 10^{-3} + 0.508(h_f - 0.121)^2] \right. \\ &\quad + [6.46 \times 10^{-3} + 0.098(h_f - 0.687)^2] \\ &\quad \left. + \left\{ 0.032(h_f - 1.132)^3/12 + 0.032(h_f - 1.132)[(h_f - 1.132)/2]^2 \right\} \right) \\ &= 0.0213h_f^3 + 1.14h_f^2 - 0.433h_f + 0.0942 \end{aligned} \quad (3.6)$$

and for the *aft spar*

$$\begin{aligned} I_a &= 2 \left([956 \times 10^{-6} + 0.250(h_a - 0.063)^2] \right. \\ &\quad + [13.1 \times 10^{-3} + 0.156(h_a - 0.625)^2] \\ &\quad \left. + \left\{ 0.032(h_a - 1.125)^3/12 + 0.032(h_a - 1.125)[(h_a - 1.125)/2]^2 \right\} \right) \\ &= 0.0213h_a^3 + 0.742h_a^2 - 0.374h_a + 0.122. \end{aligned} \quad (3.7)$$

The vertical load at the spar's root is the integral of the elliptic loading, that is, $V = \pi PL/4$. (This loading is the same as the area of a quarter-ellipse with semi-axes lengths given by the spar's maximum loading and length.) From Equations (3.3)–(3.7) we have that the vertical load at the forward and aft spars' roots are respectively

$$V_f = -\frac{(0.0213h_f^3 + 1.14h_f^2 - 0.433h_f + 0.0942)(3\pi\sigma_g L^2/h_f)}{2(2L^2 + x_g^2)\sqrt{L^2 - x_g^2} - 3x_g L^2 \left[\pi - 2 \tan^{-1} \left(x_g/\sqrt{L^2 - x_g^2} \right) \right]} \quad (3.8)$$

and

$$V_a = -\frac{(0.0213h_a^3 + 0.742h_a^2 - 0.374h_a + 0.122)(3\pi\sigma_g L^2/h_a)}{2(2L^2 + x_g^2)\sqrt{L^2 - x_g^2} - 3x_g L^2 \left[\pi - 2 \tan^{-1} \left(x_g/\sqrt{L^2 - x_g^2} \right) \right]}. \quad (3.9)$$

A negative stabilator bending-stress implies tension in the cracked lug (see Assumption 2), and hence Equations (3.8) and (3.9) have negative signs in front of them.

3.3 Horizontal (Spanwise) Load on Stabilator Spars

In this section, we calculate the horizontal (spanwise) stress on the spar's cross-section using the bending stress measured on the skin.

The horizontal loading at a particular cross-section is calculated by multiplying the horizontal stress by the cross-sectional area. Figure 3.2 (on page 17) shows how the horizontal load was calculated for the forward and aft spars.

Some simple but time consuming calculations give the horizontal loads for the three rectangular regions of both the forward and aft spars. First, we need to determine the cross-sectional area of each rectangular region. Second, we need to determine the stress at the highest and lowest parts of these rectangles, which will involve the variable height of the spar's web.

The areas and maximum stresses for the rectangular Regions 1, 2, and 3 of the *forward spar* are respectively:

$$A_{f1} = 0.508, \quad \max(\sigma_{f1}) = \sigma_f, \quad (3.10)$$

$$A_{f2} = 0.098, \quad \max(\sigma_{f2}) = \sigma_f(1 - 0.242/h_f), \quad (3.11)$$

$$A_{f3} = 0.032(h_f - 1.132), \quad \text{and} \quad \max(\sigma_{f3}) = \sigma_f(1 - 1.132/h_f), \quad (3.12)$$

where A_{fi} and $\max(\sigma_{fi})$ respectively denote the area and maximum stress of the i th rectangular region of the forward spar. The symbols σ_f and σ_a denote the stresses measured by the bending bridges on the forward and aft spars, respectively (see the tops of the stress profiles in Figure 3.2).

The areas and maximum stresses for the rectangular Regions 1, 2, and 3 of the *aft spar* are respectively:

$$A_{a1} = 0.250, \quad \max(\sigma_{a1}) = \sigma_a(1 + 0.087/h_a), \quad (3.13)$$

$$A_{a2} = 0.157, \quad \max(\sigma_{a2}) = \sigma_a(1 - 0.125/h_a), \quad (3.14)$$

$$A_{a3} = 0.032(h_a - 1.125), \quad \text{and} \quad \max(\sigma_{a3}) = \sigma_a(1 - 1.125/h_a), \quad (3.15)$$

where A_{ai} and $\max(\sigma_{ai})$ respectively denote the area and maximum stress of the i th rectangular region of the aft spar.

The minimum stress in a rectangular region is the same as the maximum stress in the region immediately below it. Mathematically, the minimum stress of the three rectangular regions belonging to the aft spar are

$$\min(\sigma_{ai}) = \begin{cases} \max[\sigma_{a(i+1)}] & \text{if } i = 1, 2, \\ 0 & \text{if } i = 3. \end{cases} \quad (3.16)$$

An analogous equation arises for the minimum stresses of the forward spar. The minimum stress of rectangular Region 3 (in both spars) is zero because this point is the centre line of symmetry, and therefore the neutral axis.

Within any of these rectangular regions, the stress varies linearly between the region's maximum and minimum stress. All of the rectangular regions in the forward and aft spars are either symmetric or antisymmetric about the horizontal line passing through each rectangle's vertical midpoint. In other words, the centroid coincides with the vertical midpoint. Thus the equation for the horizontal load in the i th region is simply given by the stress in each region's midpoint,

$$H_i = A_i \left[\frac{\max(\sigma_i) + \min(\sigma_i)}{2} \right], \quad (3.17)$$

where A_i is the area of the i th region, and $\max(\sigma_i)$ and $\min(\sigma_i)$ are the maximum and minimum stress on the i th region.

Using Equations (3.10)–(3.12) and Equation (3.17) we obtain the horizontal loads on the three rectangular regions of the *forward spar*:

$$H_{f1} = -0.508\sigma_f(1 - 0.121/h_f), \quad (3.18)$$

$$H_{f2} = -0.098\sigma_f(1 - 0.687/h_f), \quad \text{and} \quad (3.19)$$

$$H_{f3} = -0.032\sigma_f(h_f - 1.132)(0.5 - 0.566/h_f). \quad (3.20)$$

Analogously, using Equations (3.13)–(3.15) and Equation (3.17) we obtain the horizontal loads on the three rectangular regions of the *aft spar*:

$$H_{a1} = -0.250\sigma_a(1 - 0.019/h_a), \quad (3.21)$$

$$H_{a2} = -0.157\sigma_a(1 - 0.625/h_a), \quad \text{and} \quad (3.22)$$

$$H_{a3} = -0.032\sigma_a(h_a - 1.125)(0.5 - 0.563/h_a). \quad (3.23)$$

A negative stabilator bending-stress implies tension in the cracked lug (see Assumption 2), and hence Equations (3.18)–(3.23) have negative signs in front of them.

The horizontal loads given by Equations (3.18)–(3.23) under-estimate the stress on the cracked lug for the following reason: the portion of distributed loading between the spar's root and the bending bridge (used to estimate the horizontal loading) were excluded. This loading abutting the root is excluded by the fact that the bending stress is measured at some point away from the stabilator's root.

In order to correct this under-estimation the loading profile given by Assumption 6 is needed. We have already seen that the bending moment at the root, due to an elliptic loading profile, is

$$M_r = P \int_0^L x \sqrt{1 - (x/L)^2} dx = \frac{PL^2}{3}.$$

If the vertical loading between the gauge and the root is *ignored* the resulting bending moment at the root is

$$M_r^* = P \int_{x_g}^L x \sqrt{1 - (x/L)^2} dx = \frac{PL^2}{3} \left[1 - \left(\frac{x_g}{L} \right)^2 \right]^{3/2},$$

remember that x_g is the distance from the spar's root to the gauge. Taking the ratio of these two bending moments gives the *correction factor* for the horizontal loading as

$$\gamma = M_r/M_r^* = \left[1 - \left(\frac{x_g}{L} \right)^2 \right]^{-3/2}.$$

The total horizontal (spanwise) load on the top half of each spar is given by the sum of the three forces on each spar. Thus approximations to the *total horizontal load* on each spar's top half are given by

$$H_f = -0.0160 \gamma \sigma_f (\bar{h}_f - 0.189)(\bar{h}_f + 35.8)/\bar{h}_f \quad (3.24)$$

and

$$H_a = -0.0160 \gamma \sigma_a (\bar{h}_a - 0.221)(\bar{h}_a + 23.4)/\bar{h}_a \quad (3.25)$$

respectively for forward and aft spars.

As is shown next, the horizontal loading can also be calculated using information from the vertical loading. When we later calculate stress on the cracked lug (in Section 6.2), we will choose the higher of these two values for horizontal loading.

3.4 Using Vertical Load to Calculate Horizontal Load on Stabilator Spars

We can use the estimate of vertical loading given by Equations (3.8) and (3.9) to calculate the horizontal (spanwise) load on the spar's root. Below are the calculations used to obtain this horizontal load estimate.

It is possible to determine the bending moment (and hence horizontal load) at the spar's root using the estimate of vertical load. Multiplying the vertical load V and the centroidal distance of the loading from the root (namely, $4L/(3\pi)$) gives the bending moment at the root

$$M_r = \frac{4L}{3\pi} V,$$

where L is the length of the spar. In the above bending moment equation we have implicitly used the elliptic loading profile given by Assumption 6.

It is clear from Figure 3.1 that any bending moment at the spar's root is reacted out as a couple by the spar's supporting lugs. Let y_ℓ be the distance between the upper and lower supports, that is, upper and lower clevis lugs (see Figure 3.1). From Figures A4 and A12 (on pages 55 and 63, respectively) the distance between the upper lug and lower lug is $y_\ell = 5''$. Summing moments about the lower support, we obtain the horizontal load on the upper support as

$$\begin{aligned} H &= M_r/y_\ell \\ &= \frac{4L}{3\pi y_\ell} V \\ &= 6.28V, \end{aligned} \tag{3.26}$$


where V is given by either Equation (3.8) or Equation (3.9) respectively for either the forward or aft spar.

4 Information from Flight Loads Survey

All the loading information used in this report was derived from the measurements taken during the Flight Loads Survey. In order to make some approximations about the “typical” loading experienced by the cracked lug we must first aggregate the Flight Loads Survey data into loading groups. Instead of using the raw data for the fatigue analysis, the Survey’s statistically reduced data set was used. This reduced data set is explained in the second part of this section.

4.1 Partitioning 526 Manoeuvres into 12 Groups

All up, there were 526 individually named manoeuvres (and approximately 3800 runs) in the Flight Loads Survey. To gain some appreciation of whether particular manoeuvres induced high stress in the stabilators, these 526 manoeuvres were partitioned into 12 groups. And so we make the following assumption:

 **Assumption 7** *All manoeuvres within a particular group result in comparable bending stresses on the two stabilator spars.*

This assumption merely states that we can sensibly group manoeuvres together, which is reasonable as far as determining general trends goes.

The 526 manoeuvres were initially partitioned according to the work of King and Lombardo [15, pp. 62–4], who list 21 groups. These groups were then further aggregated into 12 groups. (The individual manoeuvres in each group are listed in Tables B1–B12 on pages 69–74.) This modification of the King and Lombardo (K-L) grouping was carried to (i) have approximately a dozen groups (instead of the 21 groups K-L formulated) and (ii) obtain sensible stress plots (see Section 5.3).

As can be seen from Table 4.1, which compares the groupings of this report with K-L, approximately half of the groups K-L used were absorbed into the *miscellaneous* group in this report. On the other hand, the *pullouts* group of K-L was partitioned into two groups in this report. The K-L groupings were modified for one of two reasons, either a group contained too few or too many manoeuvres. The groups that contained too few manoeuvres were absorbed into the *miscellaneous* group. In contrast, the *pullouts* group from the K-L report contained too many manoeuvres, and so it was partitioned into two groups: *symmetric pullouts* and *rolling pullouts*.

A few of the groups formulated by King and Lombardo could not be mapped onto the set of manoeuvres from the Flight Loads Survey for one of two reasons:

- The group contained no manoeuvres from the Flight Loads Survey (for example, the droop-stop pounding manoeuvre).
- The group was not explicitly named in the Flight Loads Survey (for example, the ground-air-ground cycles were decomposed into their intermediate manoeuvres).

Manoeuvres were partitioned into the 12 groups with a clear goal in mind—to estimate the stress on the cracked stabilator lug. As such, caution should be exercised when using

Table 4.1: Comparing the manoeuvre groupings used by King and Lombardo (K-L) and This report. The symbol \approx denotes approximately the same group, \nexists a non-existent group, and \emptyset a group with no manoeuvres. The symbols \odot^n and \ominus^n denote a group containing n manoeuvres that was absorbed into the miscellaneous or climb group, respectively.

K-L report	This report
autos	\approx
break turn	\emptyset
climb	\approx
dive	\odot^2
droop-stop pounding	\emptyset
ground run	\emptyset
ground-air-ground cycles	\nexists
heavy manoeuvres	\emptyset
hover	\odot^{15}
landing	\odot^2
level flight	\approx
\nexists	miscellaneous
nap of earth	\odot^2
partial power descent	\ominus^5
pullouts	$\left\{ \begin{array}{l} \text{symmetric pullouts} \\ \text{rolling pullouts} \end{array} \right.$
reversals	\approx
rotor start/stop	\odot^9
side/rearward flight	\approx
sideslip	\approx
take off	\odot^5
taxi	\odot^{15}
turns	\approx

these manoeuvre groups for any other purpose. Appendix B lists the twelve groups into which the manoeuvres from the Flight Loads Survey were partitioned.

4.2 Statistically Reduced Data Set of Flight Loads Survey

Instead of using the time-history data from the Flight Loads Survey, a statistically reduced data set⁴ of the Survey was used. This reduced data contained ten parameters (see Table 4.2) that described the time-history data set. We denote the steady and vibratory components of the stress measurements respectively by the symbols “ σ ” and “ ν ”, and the direct stress measurements by the symbol “ s ”. On any of these three symbols, the subscripts “min”, “avg”, “max”, “5%”, and “95%” respectively denote the minimum, average, maximum, and 5th and 95th percentile stress.

Table 4.2: *The ten statistical parameters that describe the time-history data set for the Flight Loads Survey. The maximum and minimum stresses are not shown in this section’s stress plots, and hence were not assigned symbols. The mnemonics shown were assigned by GTRI.*

	Symbol	Mnemonic	Parameter description
steady	σ_{\min}	MIN_STDY	minimum of steady stress component
	σ_{avg}	AVG_STDY	average of steady stress component
	σ_{\max}	MAX_STDY	maximum of steady stress component
vibratory	ν_{avg}	AVG_VIB	average of vibratory stress component
	ν_{\max}	MAX_VIB	maximum of vibratory stress component
	$\nu_{95\%}$	PCL_VIB	95th percentile of vibratory stress component
direct	-	ABMIN_STDY	minimum directly measured stress
	-	ABMAX_STDY	maximum directly measured stress
	$s_{5\%}$	PCC_DIR	5th percentile of directly measured stress
	$s_{95\%}$	PCL_DIR	95th percentile of directly measured stress

According to King and Boykett [14], one way to calculate the steady and vibratory components of stress from the time-history data is as follows:

- Determine all stress *cycles*, which are defined as two consecutive turning points (S_1 and S_2) from the time-history data.
- The *steady* component of the stress is defined as the mean of these two turning points, that is, $\sigma = (S_1 + S_2)/2$.
- The *vibratory* component of the stress is defined as half the difference (in modulus) of these two turning points, that is, $\nu = |S_1 - S_2|/2$.

In contrast, before performing the steps described above Sikorsky⁵ pre-process the data for each flight run to reduce the number of turning points. This pre-processing

⁴The time-history data set was approximately 300 GB in size and was stored on 25 CDs. In contrast, the statistically reduced data set was approximately 0.1 GB in size and fits on a single CD.

⁵Sikorsky calculated these statistical parameters for a GTRI report.

determined the peaks and troughs inside fixed time windows. Sikorsky chose the tail rotor frequency (which is 19.8 Hz) as the most important loading frequency, and hence used time windows of 0.051 seconds (which is the inverse 19.8 Hz). Compared to the raw sampling rate of 833 Hz used during the Flight Loads Survey, Sikorsky's pre-processing results in a reduction in the number of turning points. This turning point reduction yields larger (and hence more conservative) vibratory stresses, which are used to derive fatigue damage.

Like King and Boykett [14], we have *not* used Sikorsky's data pre-processing technique to determine the GTRI statistical parameters.

Table 4.3 compares the results obtained by GTRI with the results obtained using the more accurate procedure outlined above. If "s" is a direct, vibratory, or steady stress, then the percentage difference shown in this table was calculated as follows:

$$\% \text{-diff} = (s_G - s_R)/s_G,$$

where s_G and s_R are the stresses calculated respectively by *GTRI* and *this report*.

Table 4.3: *Percentage difference of statistical parameters obtained by GTRI and this report (which are labelled Our). All units are in psi, except for the error which is percentage error. The stress on bulkhead FS308 was measured during a 45° left turn. The stress on the stabilator was measured during level flight.*

Parameter		Bulkhead (psi)			Stabilator (psi)		
		GTRI	Our	Diff.	GTRI	Our	Diff.
steady	σ_{\min}	-8237	-8832	-7.2%	-18102	-24016	-33%
	σ_{avg}	-7903	-7844	0.75%	-16644	-16520	0.75%
	σ_{\max}	-7460	-7133	4.4%	-15120	-9062	40%
vibratory	ν_{avg}	621	265	57%	6664	1636	75%
	ν_{\max}	1104	1064	3.6%	9569	8799	8.0%
	$\nu_{95\%}$	880	565	36%	8527	4808	44%
direct	ABMIN.STDY	-8988	-8988	0%	-26853	-26853	0%
	ABMAX.STDY	-6669	-6669	0%	-7042	-7042	0%
	$s_{5\%}$	-7311	-7324	-0.18%	-11594	-11755	-1.4%
	$s_{95\%}$	-8483	-8474	0.11%	-21640	-21564	0.35%

The statistical parameters were compared with the GTRI results for two manoeuvres:

- a 45° left turn from run 46 of flight 28 (RECOVERY_LT_TN, 45DEG) and
- level flight from run 82 of flight 24 (LEV.FLT_FORWARD, 0.9VH).

The left turn manoeuvre was chosen to compare results with King and Boykett [14]. For this left turn manoeuvre, measurements were taken from a strain gauge on the FS308

bulkhead⁶ (see the description given by Friend [8, p. 44] for gauge **BEAMAS1**). The level flight manoeuvre was chosen randomly as an additional check. For this level flight manoeuvre, measurements were taken from the right-hand side bending bridge Number 1 (see Figure 2.1 and the description for gauge **STBNBM1R** in Section 2.1).

As can be seen from Table 4.3, the two results are identical for the absolute maximum and minimum of the direct stress. The 5th and 95th percentile are within 1% error, as is the average steady component (σ_{avg}). The remaining parameters are significantly different. These large differences are explained by the definition of a turning point.

We have used the mathematical definition of a turning point, that is, either a local maximum or minimum. Using this definition of a turning point, the magnitudes of the steady and vibratory components are respectively over- and under-estimated as compared to the GTRI magnitudes (see Table 4.3). This over- and under-estimation show that GTRI ignored certain intermediate turning points that they considered insignificant for the fatigue analysis. As an example, in Figure 5.2 (on page 33) the red points (which denote turning points) were determined using the mathematical definition of a turning point. The arrow in this figure marks a pair of turning points GTRI may be ignoring when calculating the statistical parameters.

⁶On the lower face of the upper flange of the BL34.5 longeron, just aft of FS308 on the left-hand side.

5 Bending Stress on Stabilator Spar

In this section we determine the stress experienced by the stabilator spars in three different ways. The first method assumes the worst-case scenario and determines the spar bending stress by considering the combination of maximum stress and alternating stress that yield the highest fatigue. As an alternative, the second method considers a typical high-loading case and determines the bending stress that more closely approximates the cracked lug's fatigue. Unlike the worst-case scenario, however, this high-loading case is *not necessarily* conservative. The final method assumes the best-case scenario and determines the spar bending stress by considering the median loading for both the steady and vibratory components of stress.

5.1 Fatigue Equation for 7075 Aluminium Alloy

Before we can determine the worst-case stress combination, we need to know the fatigue properties of the cracked lug's material, which is 7075-T7 aluminium alloy [6].

According to Higdon et al. [12, p. 573], the stress concentration factor to use in the fatigue analysis of a lug with the geometry of the cracked lug is approximately 2 (see, in particular, Figure 11-9(c) in Higdon et al. [12]). Thus the correct fatigue curve to use in the fatigue analysis is an S-N curve for notched specimens with $K_t = 2$.

Let S_{\max} and S_{\min} respectively denote the maximum and minimum stresses of the loading cycles (given in ksi) and

$$R = S_{\min}/S_{\max} \quad (5.1)$$

denote the stress ratio. Using MIL-HDBK-5 [7, p. 3-411], which is the abbreviation for Volume 5 of the Military Handbook for Metallic Materials, the equation⁷ for cycles to failure of $K_t = 2$ notched 7075-T6 aluminium alloy is given by

$$N_f = 31.6 \times 10^6 (S_{eq} - 18.6)^{-2.46}, \quad (5.2)$$

where S_{eq} is the equivalent stress defined by

$$S_{eq} = S_{\max}(1 - R)^{0.54}. \quad (5.3)$$

Equations (5.1) and (5.3) were developed using net stresses. See the MIL-HDBK-5 for restrictions on using Equation (5.2).

Since MIL-HDBK-5 does not contain fatigue information on 7075-T7 aluminium alloy (the material of the cracked lug) we make the following assumption:



Assumption 8 *The cycles to failure formula given by Equation (5.2) for 7075-T6 aluminium alloy is also valid for 7075-T7 aluminium alloy.*

As a comparison of these two alloys, the ultimate and yield tensile strengths for these two temperings are:

⁷In MIL-HDBK-5, Equation (5.2) is shown in logarithmic (base 10) form.

- $F_{tu} = 74$ ksi and $F_{ty} = 63$ ksi for the T6 tempering treatment [7, p. 3-371] and
- $F_{tu} = 67$ ksi and $F_{ty} = 56$ ksi for the T7 tempering treatment [7, p. 3-373].

Thus we might expect that Equation (5.2) results in a slight under-estimation of cycles for the T7 tempering. This expectation is supported by experimental data [19, Fig. 3.0552] comparing T6 and T7 tempering. Hence Assumption 8 appears to be conservative.

The cycles to failure formula is based on experimental data with bounded stress ratios, and thus the following assumption is required:



Assumption 9 *The cracked lug is not pre-stressed in tension and the cycles to failure formula given by Equation (5.2) can be extrapolated into the ranges $R < -1$ and $0.5 < R < 1$.*

Assuming that the stabilator lugs are *not* pre-stressed in tension, then the purely compressive load cycles ($S_{\max} < 0$ and $R > 1$) can be ignored in the fatigue analysis. Hence Assumption 9 is not affected by the range $R > 1$. We are considering the worst-case scenario, and hence assuming that the most fatiguing combination of S_{\max} and R is acting during all manoeuvres. Provide we can extrapolate the cycle-to-failure contours, then from the zoomed section in Figure 5.1 (on page 30) it is clear that the highest equivalent stress occurs outside the ranges $R < -1$ and $0.5 < R < 1$.

5.2 Worst-Case Bending Stress from Flight Loads Survey

One way to determine the loading for the worst-case loading scenario is to consider the maximum equivalent stress, which is given by Equation (5.3). Plotting S_{\max} versus R and then superimposing contours of constant equivalent stress on this plot we can determine the worst-case loading combination of S_{\max} and R .

A log-like⁸ plot of the maximum stress S_{\max} versus the stress ratio R is shown in Figure 5.1, where we have taken $S_{\min} = s_{5\%}$ and $S_{\max} = s_{95\%}$. In other words, for each run from the Flight Loads Survey, we have taken the minimum and maximum stress to be the 5th and 95th percentile of the directly measured stress for that run. These 3765 runs were partitioned into the twelve groups described in Section 4.1. The short horizontal lines (on the plot's right) show the S_{\max} distribution of each group.

A negative bending stress in the stabilator spars generates a tensile stress in the cracked lug (see Assumption 2 on page 8). Thus to obtain the correct combination of S_{\max} and R for the fatigue analysis of the cracked lug, the sign of the bending stresses were reversed in Figure 5.1.

The zoomed section in Figure 5.1 shows contours of cycles-to-failure, which were calculated from Equation (5.2). This cycles-to-failure equation is derived from coupons tested at stress ratios of $-1 \leq R \leq 0.5$, and hence the contours in this zoomed section were restricted to this same range of stress ratios.

⁸The horizontal axis of Figure 5.1 is on an *arcsinh* scale, which is approximately linear about zero and logarithmic elsewhere (as illustrated by the tickmarks).

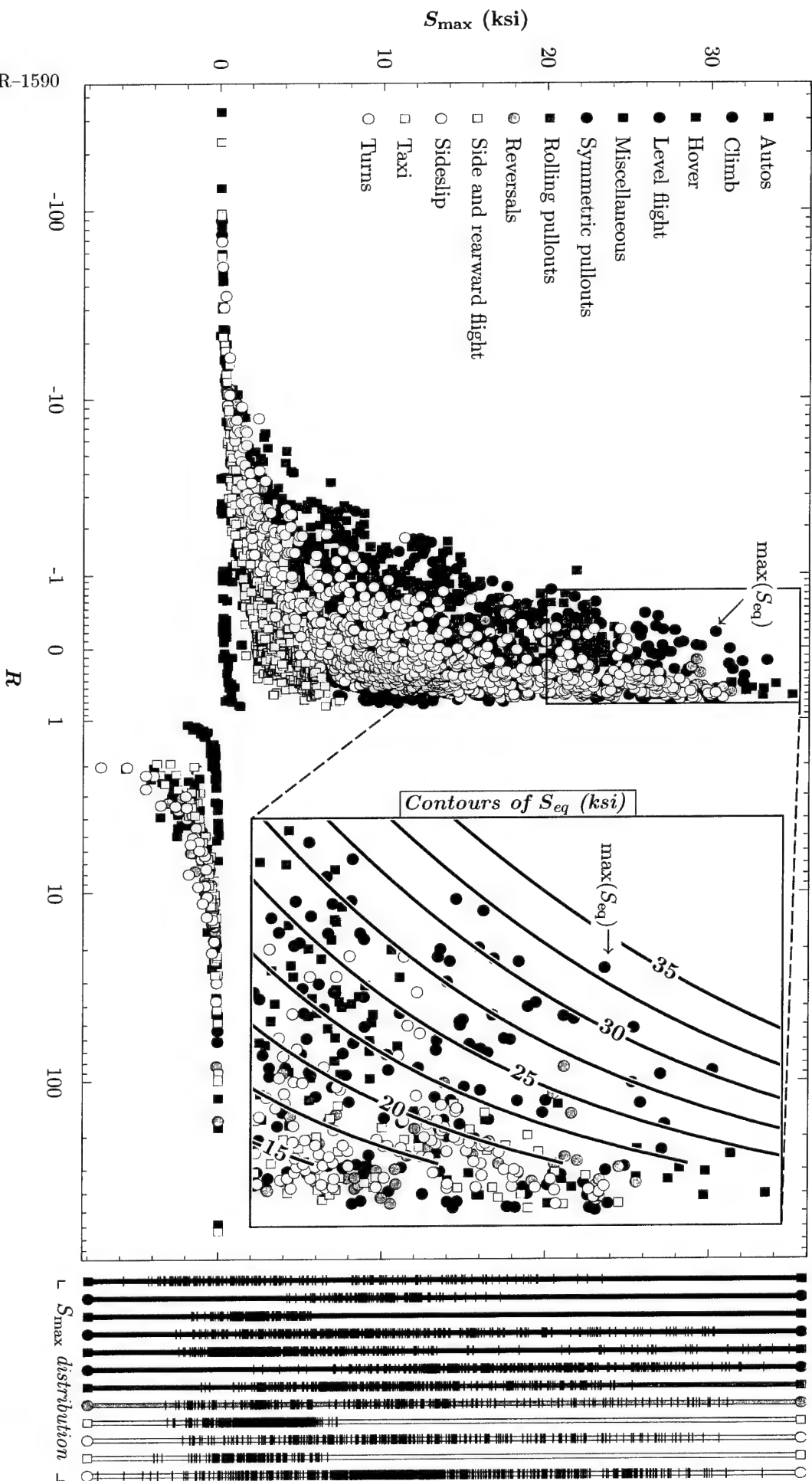


Figure 5.1: Plot of maximum stress (at bending bridge Number 1) versus stress ratio for all runs of the Flight Loads Survey. The “minimum” and “maximum” stresses were taken as $s_{5\%}$ and $s_{95\%}$ (that is, 5th and 95th percentile of the directly measured stress). The short horizontal lines to the right of the plot show the S_{max} distribution for each group. Contours of equivalent stress S_{eq} are superimposed onto the zoomed inset.

For expediency, we chose $s_{5\%}$ and $s_{95\%}$ to calculate fatigue, and so we require the following assumption:



Assumption 10 *The 5th and 95th percentile of stabilator stress measured during the Flight Loads Survey characterise the fatigue loading that the stabilator lug experiences.*

For a quick-and-dirty analysis, we require a single loading amplitude to calculate fatigue. Alternative ways to determine the single loading amplitude (listed in order of increasing fatigue severity) include:

- Using the *average steady* stress combined with the *average vibratory* stress; that is,

$$S_{\min} = \max_i(\sigma_{\text{avg}i}) - \max_i(\nu_{\text{avg}i}) \quad \text{and} \quad S_{\max} = \max_i(\sigma_{\text{avg}i}) + \max_i(\nu_{\text{avg}i}),$$

where i is the run number and the maximum is taken over all runs.

- Using the *maximum and minimum steady* stress combined with the *maximum vibratory* stress; that is,

$$S_{\min} = \max(\sigma_{\min i}) - \max(\nu_{\max i}) \quad \text{and} \quad S_{\max} = \max(\sigma_{\max i}) + \max(\nu_{\max i}).$$

- Using the *maximum and minimum direct* stress measured; that is,

$$S_{\min} = \max(s_{0\%i}) \quad \text{and} \quad S_{\max} = \max(s_{100\%i}).$$

Intuitively, we thought the stress given by the first alternative would yield results that were unconservative; while the stresses given by the remaining two alternatives would yield results that were too conservative.

The single load amplitude resulting from Assumption 10 yields a coarse approximation, which was required to produce timely results. Without this assumption we would need to carefully analyse the usage spectrum of the helicopter in order to say *approximately* how it is used. Assumption 10 can be refined by assumptions that are successively better models of reality. Two examples of more refined assumptions are:

- Determine approximately what percentage of time the helicopter spends in each manoeuvre group and then calculate approximate stresses for each of these groups.
- Or even more realistically, determine approximately what percentage of time the helicopter spends in each individual manoeuvre and then calculate approximate stresses for each of these manoeuvres.

Both of these refined assumptions head towards the goal of recalculating the fatigue life of the cracked lug based on data from the Flight Loads Survey. It must be remembered, however, that the stress at the lug is approximated using the bending stress on the stabilator's spar. Hence it would be questionable to aim for the higher accuracy suggested by the recommended refinements listed above when the other aspects of the fatigue analysis were of a lower accuracy.

From Equation (5.3) and Figure 5.1 the most fatiguing run was a symmetric pushover manoeuvre, which had a maximum stress of $S_{\max} = -30.3$ ksi and a stress ratio of $R = -0.186$. Substituting these values into Equation (5.3) gives the equivalent stress as

$$S_{\text{eq}} = -33.2 \text{ ksi} \quad (\text{worst-case loading}), \quad (5.4)$$

which comes from run 9 of flight 75 (with run mnemonic SYMM_PUSHOVER, VH, .25G). This maximum equivalent stress is singled-out by the arrow in Figure 5.1. Remember that the sign of the stresses in Figure 5.1 were reversed to obtain the correct stress in the cracked lug. This sign reversal explains the negative sign of the equivalent stress value in Equation (5.4).

5.3 High Bending Stress from Flight Loads Survey

As will be seen later, the fatigue life predicted by the worst-case scenario is very short. To gain some appreciation for how over-conservative this worst-case is, a typical fatigue life (based on high loading) is now calculated. The difference between this section and the previous section is that we are now using a *high* loading (based on a typical level flight run) and not the *worst-case* loading (determined over all runs). The strong caveat is that stresses obtained in this section are *not necessarily* conservative, and hence should only be used in making comparisons with the worst-case scenario.

In this section we determine a “typically high” stress on the stabilator at a location that is 9” outboard of the cracked lug. This typically high stress is determined using information from the Flight Loads Survey and engineering judgements as to what constitutes typically high. (More precise definitions of “typically high” are given later.) In this section these engineering judgements are typeset as assumptions and explained when they are introduced.

Figure 5.2 shows a legend for the stress plot in this section (and the stress plots in Appendix D). The time-history data in this plot are taken from a level flight manoeuvre (run 82 of flight 24, LEV.FLT_FORWARD, 0.9VH). Only the first 0.481 seconds of this 15.5 second manoeuvre are shown, that is, approximately 3% of the time-history data are shown. The stress for the remainder of this manoeuvre has a similar structure to the stress encountered in the first 3% of the manoeuvre. The complete 15.5 second time-history data (*not* just the first 3%) was used to calculate the statistical parameters in the colour coded legend of this example.

The legend in Figure 5.2 summarises the most relevant statistical parameters calculated for the data from the Flight Loads Survey. The definitions of the different symbols found in this legend are given in Table 4.2 (on page 25). The upper and lower halves of this legend are not exactly symmetric. The uppermost and lowermost points of the red region are over-conservative bounds on the true maximum and minimum, respectively. Although possibly unconservative, better approximations to the maximum and minimum stresses are given by the extreme points of the green section; namely, $\sigma_{\max} + \nu_{\text{avg}}$ and $\sigma_{\min} - \nu_{\text{avg}}$, respectively.

The stress for the *level flight* group is shown in Figure 5.3 (for further details, and the plots for other groups, see Appendix D on page 83). This figure shows the stress

for all manoeuvres that were categorised as level flight. The stress is sorted by average steady stress for each run, which explains why the average steady stress (depicted by the white line) is monotonically increasing. The vertical axis measures stress (in ksi) and the horizontal axis enumerates the sorted runs (for the level flight group there were 338 runs). These stress measurements were for bending bridge Number 1 on the right-hand stabilator, which is 9.2" from the stabilator inboard edge and has mnemonic STBNBM1R (see Figure 2.1 on page 9).

As can be seen from Figure 5.3, the average of the steady component σ_{avg} varies from approximately -25 ksi to +5 ksi, while 90% of the directly measured stresses (that is, $s_{5\%}$ to $s_{95\%}$) ranged from approximately -30 ksi to +8 ksi.

In order to estimate the stress on the cracked stabilator lug we make two assumptions. The first assumption essentially defines a "typical" stress.



Assumption 11 *The stresses experienced by the helicopter (at least in the stabilator) during level flight are typical of normal flying.*

This assumption of a single load amplitude yields a coarse approximation, which could be refined analogously to the suggested refinements of Assumption 10.

The second assumption goes on to say that the manoeuvres within this typical group are homogeneous in stress:

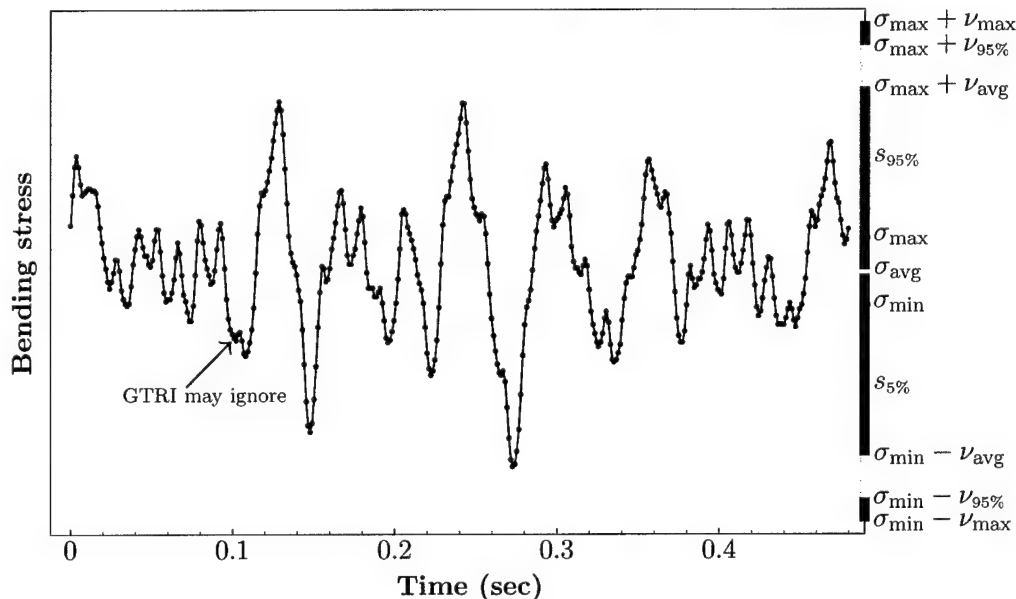


Figure 5.2: Legend for the statistical parameter plots of bending stress. Time-history data for first 0.481 seconds of the 15.5 seconds it took to complete this level flight manoeuvre. The symbols " σ " and " ν " respectively denote the steady and vibratory component of the stress, while the symbol " s " denotes the direct measurement of stress.

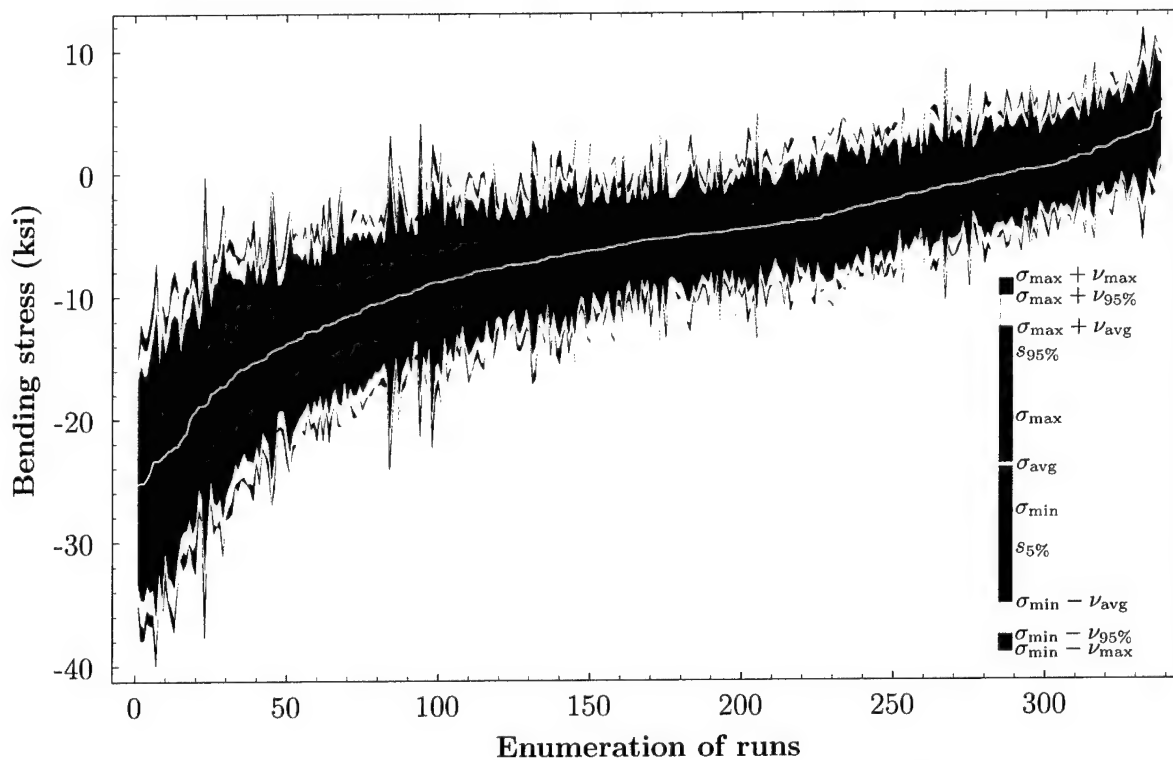


Figure 5.3: Plot of stabilator spar bending stress for the level flight manoeuvre group. These stresses were sorted by the average steady stress for each run. These stress measurement were taken at bending bridge Number 1, which is located 9.2" from the stabilator root.



Assumption 12 The helicopter spends the same amount of time in each manoeuvre within the level flight group and each of these manoeuvres experiences the same stress.

Again, this coarse assumption was required to produce timely results. The suggested refinements given for Assumption 10 are also valid for Assumption 12.

A fatigue strength analysis of the whole stabilator assembly⁹ by Sikorsky [1] makes simplifications similar to Assumptions 11 and 12. Sikorsky states: (i) that transient manoeuvres did not produce stresses that were significantly different to high speed level flight; and (ii) that the percentage of time spent in transient manoeuvres was small as compared to level flight. Using these two observations Sikorsky [1, p. H-10] concludes that fatigue testing could be conducted at the lug stresses observed during high speed level flight.

To be conservative in the fatigue analysis that follows, we want to obtain a typically high fatigue stress. One way to obtain this *typically-high steady-stress* is to consider the 95th percentile steady stress shown in Figure 5.3. Negative bending stresses imply tension in the lug, and hence we want the 5th percentile of σ_{\min} to use in fatigue calculations.

⁹The stabilator assembly that was fatigue tested by Sikorsky consisted of the left and right stabilators and the centre-box.

From 338 runs, the 5th percentile occurs approximately at run 17 (see Figure 5.3), which has a minimum steady stress of $\sigma_{\min} \approx -23$ ksi. Using a similar procedure to determine the 95th percentile run and its corresponding 95th percentile vibratory stress¹⁰ yields $\nu_{95\%} \approx 9$ ksi, which is the *typically-high vibratory-stress*. In summary, the typically high stress on bending bridge Number 1 has a steady component of -23 ksi and a vibratory component of 9 ksi. Substituting the resulting maximum stress $S_{\max} = -32$ ksi and stress ratio $R = 0.44$ into Equation (5.3) gives the equivalent stress as

$$S_{\text{eq}} = -23.4 \text{ ksi} \quad (\text{typically high loading}). \quad (5.5)$$

Again, remember that a negative bending stress on the stabilator implies a tensile stress on the cracked lug. This explains why the maximum stress S_{\max} is more negative than the steady stress. In other words, the operator in the calculation of maximum stress is subtraction *not* addition, that is,

$$S_{\max} = (\sigma_{\min})_{95\%} - (\nu_{95\%})_{95\%}. \quad (5.6)$$

The 95th percentile stresses were chosen based on the engineering judgement that these percentiles would best predict fatigue. In contrast, choosing average stresses or the maximum stresses would result in fatigue predictions that were respectively either unconservative or too conservative. This engineering judgement (to choose the 95th percentile) requires the following assumption:



Assumption 13 *The 95th percentile stress (for both the steady and vibratory components) yields conservative approximations of fatigue.*

This assumption was made to obtain a less conservative fatigue estimate than the worst-case scenario. The problem with Assumption 13 is that we would expect any single-amplitude estimate of fatigue loading to be close to the run-out stress of the component; that is, we expect the single-amplitude load to be at the flat-end of the fatigue curve. In this run-out region, small variations in loading can lead to large variations in cycles to failure.

The typical high stress was chosen based on percentiles, and hence there is an implicit assumption that the Flight Loads Survey [3] was representative of in-service usage. More specifically, that the number of runs for each manoeuvre carried out during the Flight Loads Survey is representative of the in-service flight-time fraction of those manoeuvres. This implicit assumption is probably reasonable, but not for the reasons that may first spring to mind. The Flight Loads Survey was carried out to obtain load estimates for critical components—and not to determine the Black Hawk's usage spectrum. Thus we might expect that this implicit assumption may not be accurate. However, the stress range obtained from the Survey is probably representative of the stress range components would experience in-service. So although the fraction of time spent in different manoeuvres during the Flight Loads Survey is not representative of in-service usage, the stress range probably is representative of in-service stress!

For expediency, we choose a single flight group to be representative of typical loads:



Assumption 14 *The “typically high” stress experienced by the stabilator during the level flight group of manoeuvres is typical of in-service flight for fatigue purposes.*

Level flight consumes most of the in-service flight time, and also consumes a fair proportion of fatigue life in dynamically loaded components from the rotor system (see Krake [16] and Polanco [22]). We would then expect, from a fatigue perspective, that using level flight to approximate typical flying is a reasonable assumption.

5.4 Best-Case Bending Stress from Flight Loads Survey

In this section, the best-case bending stress on the stabilator is determined using measurements from the Flight Loads Survey. Remember that if the cracked lug is still prone to fatigue under this “gentle” loading, then we would be concerned that other Seahawks may also be susceptible to the same centre-box lug cracking.

Using engineering judgement, the median loading should represent a gentle loading scenario. In other words, the true fatigue life of the component should be shorter than the fatigue life predicted using the median loading. Hence the median loading is used to determine this “best-case” scenario.

Since by definition the median is the 50th percentile, the analysis in this section is analogous to the analysis in the previous section. The only difference between these two sections is that we are now considering median steady and vibratory loads (as opposed to 95th percentile steady and vibratory loads used in the previous section). *The assumptions made in Section 5.3 are also required in this section’s analysis.* For brevity, however, these assumptions will not be explicitly repeated in this section.

From the bending stress plot shown in Figure 5.3, the median steady load occurs approximately at run 169 (which is half of the 338 runs shown in this plot). Analogously to the previous section, see Equation (5.6), the maximum stress is calculated as

$$S_{\max} = (\sigma_{\text{avg}})_{50\%} - (\nu_{\text{avg}})_{50\%},$$

where $(x)_{50\%}$ denotes the 50th percentile (that is, the median) of the argument x . The median steady and vibratory components are -5.5 ksi and 3.5 ksi, respectively, which give a maximum stress of $S_{\max} = -9.0$ ksi and a stress ratio of $R = 0.22$. Substituting these values for maximum stress and stress ratio into Equation (5.3) gives the equivalent stress

$$S_{\text{eq}} = -7.9 \text{ ksi} \quad (\text{best-case loading}). \quad (5.7)$$

¹⁰Unlike the high steady stress, the high vibratory stress *cannot* be easily determined from Figure 5.3. However, the procedure for the determination of the high vibratory stress is analogous to the calculation of the high steady stress.

6 Fatigue of Cracked Lug

In any fatigue analysis, the two most important pieces of information are the loading (i) frequency and (ii) amplitude. In this section we estimate both these quantities from measurements taken during the Flight Loads Survey. The loading frequency is estimated using a frequency decomposition of a level flight manoeuvre. While the loading amplitude is estimated from the geometry of the cracked lug and the bending stress on the stabilator.

6.1 Stabilator Frequency Response during Level Flight

In this section the loading frequency is estimated in order to determine the cracked lug's susceptibility to fatigue under typical loading conditions.

To determine the stabilator's frequency response at a location, both the input loading and the resulting frequency response are required. From vibration analysis (see, for example, Thomson [26, p. 380]) the *frequency response* of a system is given as the ratio of output to input

$$\mathcal{H}(\omega) = \frac{\mathcal{Y}(\omega)}{\mathcal{X}(\omega)} = \frac{\text{FT of output}}{\text{FT of input}},$$

where ω is a particular frequency and \mathcal{H} , \mathcal{X} , and \mathcal{Y} are respectively the Fourier transforms (FTs) of the response, input, and output functions.

For the Flight Loads Survey, we do *not* have the input loading; and hence cannot calculate the response function. Thus we require the following assumption:



Assumption 15 *The typical loading frequency is calculated from the stabilator's frequency response during a level flight manoeuvre from the Flight Loads Survey. The typical loading frequency is defined to be the highest frequency out of all the large amplitude loading frequencies (excluding the zero frequency). In terms of fatigue, this typical loading is assumed to be the dominant (that is, most important) loading.*

This assumption was made for expediency. A more accurate fatigue analysis would require cycle counting of the stress history, which is different to the simple frequency decomposition undertaken in this section.

Under Assumption 15 the typical loading frequency is chosen based on two requirements: (i) a large loading amplitude and (ii) the highest frequency from this large amplitude group. The highest frequency aspect of this assumption should make this assumption conservative—in fact, probably too conservative! For expediency we leave a more refined analysis for future work, and merely acknowledge the over-conservatism in this report.

We need one further assumption, this time about how the typical loading frequency varies among different manoeuvres:



Assumption 16 *The typical loading frequency is the same for all manoeuvres, and is determined from the stabilator bending stress (STBNBM1R) of a level flight manoeuvre (LEV.FLT_FORWARD, 0.9VH).*

This level flight manoeuvre was deemed to be typical because the level flight group of manoeuvres consumes the largest portion of flying time. (See Krake [16, p. 25] for the Seahawk usage spectrum, which show level flight consuming approximately 70% of the flight-time.)

The frequency responses from a level flight manoeuvre (see Figure 6.1) can be compared with that of a rolling pullout and a rough approach (see Figures E1-E2 on pages 110-111). This comparison of the highest significant frequencies adds weight to Assumption 16, namely, that the different manoeuvres are frequency homogeneous (at least in terms of significant fatigue frequency).

The frequency response of the stabilator, at bending bridge Number 1 (STBNBM1R), is shown in Figure 6.1. This response plot is for the level flight manoeuvre from run 82 of flight 24 (LEV.FLT_FORWARD, 0.9VH) of the Flight Loads Survey. During the Flight Loads Survey measurements from bending bridge Number 1 were recorded at 833 Hz, which gives the Nyquist frequency of 416 Hz shown in Figure 6.1.

The frequency response was calculated using Mathematica's [27]

`Fourier[u, FourierParameters->{-1,1}]`

command, which returns the discrete Fourier transform of the time-history data \mathbf{u} . The Fourier transform of the vector \mathbf{u} is given by

$$v_k = \frac{1}{n} \sum_{j=1}^n u_j \exp[2\pi i(k-1)(j-1)/n], \quad \text{for } k = 1, 2, \dots, n,$$

where $i = \sqrt{-1}$ and u_j and v_k are the j th and k th component of the n -dimensional complex vectors \mathbf{u} and \mathbf{v} , respectively.

Because the time-history data are real (that is, $\mathbf{u} \in \mathbb{R}^n$), we require only half of the complex vector \mathbf{v} . (The second half of this vector is the complex conjugate of the first half; see, for example, Press et al. [23, p. 497].) Except for the first element (which represents the mean of the time-history), the first half of the discrete Fourier transform \mathbf{v} was multiplied by 2 in order to compensate for the discarded second half. In summary, the frequency response figure shown in this section plots stress amplitude ($|v_1|$ and $2|v_k|$ for $k = 2, 3, \dots, n/2$) versus frequency.

The thick black line in Figure 6.1 represents a polynomial fit of the frequency data. For numerical accuracy, this polynomial of degree twenty was fitted as a Chebyshev polynomial of the first kind¹¹ and was scaled to the range of the horizontal axis.

The spikes in the top plot of Figure 6.1 occur near multiples of the tail rotor frequency ω_t , which is 19.8 Hz. Multiples of the tail rotor frequency are shown by the red vertical lines. The boxed labels attached to these lines denote which multiple of the tail rotor frequency the attached red line represents.

A close-up of the first 80 Hz (shown in the bottom plot of Figure 6.1) also shows the effect of the main rotor frequency ω_m , which is 4.3 Hz. The thick black line in this figure represents a first-kind Chebyshev polynomial fit to *only* the first 80 Hz of the frequency data.

¹¹For a definition of Chebyshev polynomials see, for example, Abramowitz and Stegun [2, p. 778]

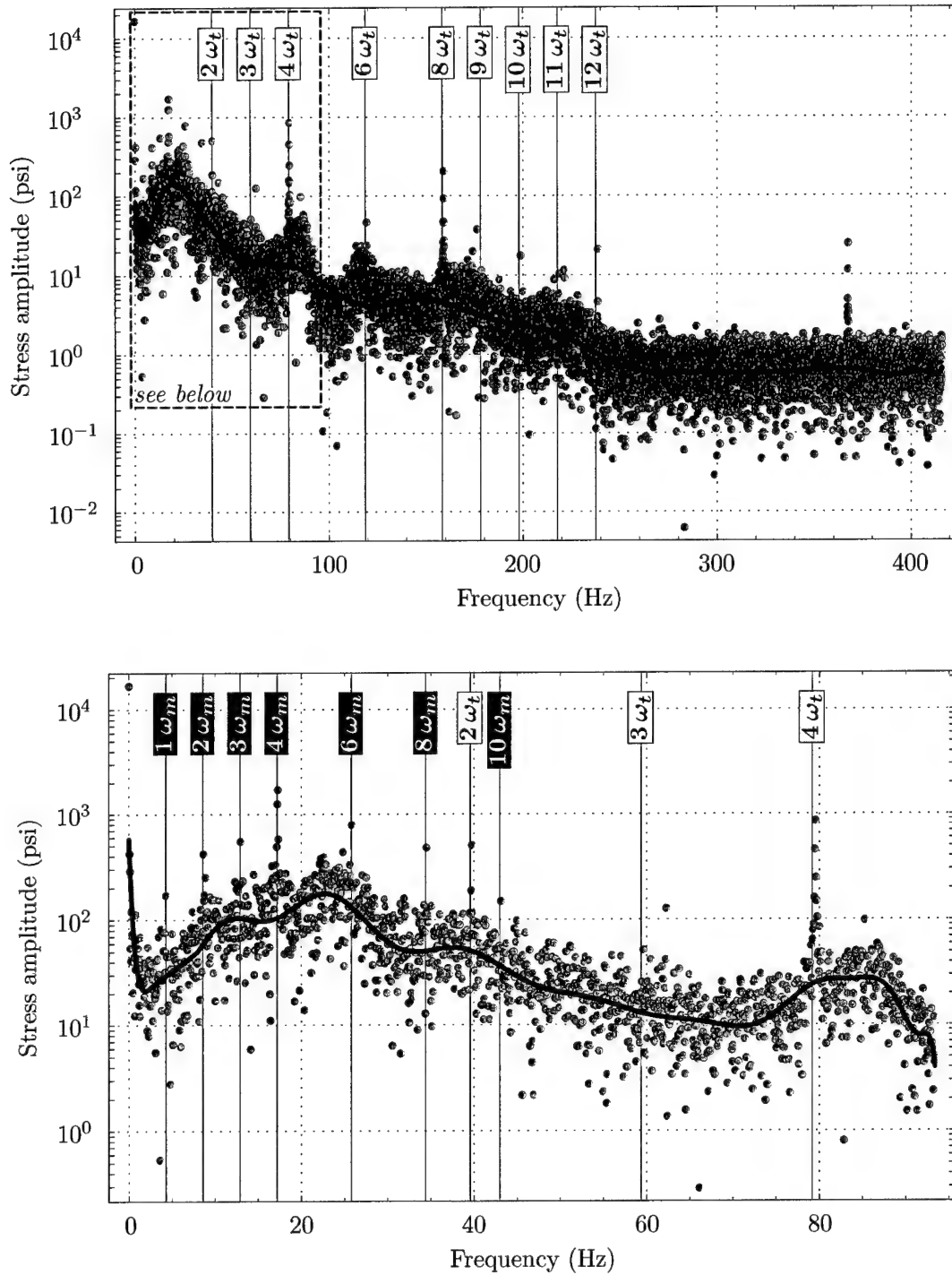


Figure 6.1: *Frequency response of stabilator during level flight. The bottom plot is a zoomed section of the dashed box in the top plot. The red vertical lines labelled with a box denote multiples of either the main or tail rotor frequencies, which are $\omega_m = 4.3$ Hz and $\omega_t = 19.8$ Hz, respectively.*

Surprisingly, the first multiple of the tail rotor frequency is almost a vibration node; that is, the vibrating amplitude at 19.8 Hz is lower than the amplitude at the surrounding frequencies. However, the stabilator does strongly resonate at the second and fourth multiple of the tail rotor frequency (that is, at $2\omega_t = 39.6$ Hz and $4\omega_t = 79.2$ Hz).

The resonating frequencies that occur at approximately 62.3 Hz and 367 Hz do not appear to coincide with multiples of either the main or tail rotor frequencies. We suspect that these resonating frequencies may be natural frequencies of the stabilator. Alternatively, these frequencies may be due to aerodynamic excitations from the main rotor blade—perhaps buffeting?

To check that the frequency response shown in Figures 6.1 was typical, two additional manoeuvres were investigated. The results for these manoeuvres (a rolling pullout and a rough approach) are shown in Appendix E on pages 110 and 111.

The highest frequency within the high loading group of frequencies in Figure 6.1 occurs at four times the tail rotor frequency

$$\begin{aligned}\phi_{hi} &= 4\omega_t = 79.2 \text{ Hz} \\ &\approx 290 \times 10^3 \text{ cycles/hour,}\end{aligned}\tag{6.1}$$

which is the frequency of the worst-case scenario. As has already been mentioned, this frequency value is probably too conservative, and so we also determine a lower frequency value to reduce this conservatism.

Figure 5.2 (on page 33) shows a time history plot of the stabilator's bending stress for a level flight manoeuvre (see Section 5.3 for further details of this plot). In this plot, the peak-to-peak timing of "significant" stresses is approximately 0.1 seconds. (A significant stress cycle is loosely defined to be a cycle that exceeds the 5th and 95th percentile of directly measured stress.) Inverting the period of this cycle gives what we term the medium frequency of a typically high loading

$$\begin{aligned}\phi_{med} &= 10 \text{ Hz} \\ &\approx 36 \times 10^3 \text{ cycles/hour.}\end{aligned}\tag{6.2}$$

To provide some perspective on the two loading frequency values given by Equations (6.1) and (6.2), the fatigue striation marks on the cracked lug were analysed fractographically.

A limited amount of fractographic data was generated by sampling five small regions on the cracked lug (see Appendix G on page 120 for further details). Extrapolating the number of visible striations found on these five sampled regions provided a lower bound on the number of loading cycles over the entire crack length, namely, 20 000 cycles. Thus a lower bound for the loading frequency that was fatigue damaging¹² is 0.01 Hz, which is three orders of magnitude below 10 Hz (the lowest of the two loading frequency estimates calculated above).

One explanation for the discrepancy between these loading frequencies is that the damage was not evenly spread over the service life of 402 hours, but instead was concentrated into a short crack life. However, the crack's contamination by lubricant suggests a crack life of weeks, rather than a crack life of hours (which would be implied by a 10 Hz loading frequency).

¹²This fractographic loading frequency was calculated as $20\,000/(402 \times 60 \times 60) \approx 0.01$ Hz.

If we consider that several of the assumptions used in this analysis had an undefined level of conservatism (particularly Assumption 11), then the fractography data suggests that these were extremely conservative. It is not within the scope of this report to reduce the level of conservatism, but it may be possible to target these reductions in future efforts.

6.2 Stress and Fatigue on Centre-Box Lug

In this section we determine the stress on the cracked lug using the loading estimates developed in earlier sections. First, the geometry of the centre-box lug (which attaches to the stabilator) is determined. Then, a simple load analysis determines the stress on this lug. Finally, the fatigue on the centre-box lug is estimated.

Figure 6.2 illustrates the two relevant (to the cracked lug) failure modes of a lug: (i) by tension and (ii) by shear tear out, see Bruhn [4, p. D1.5].

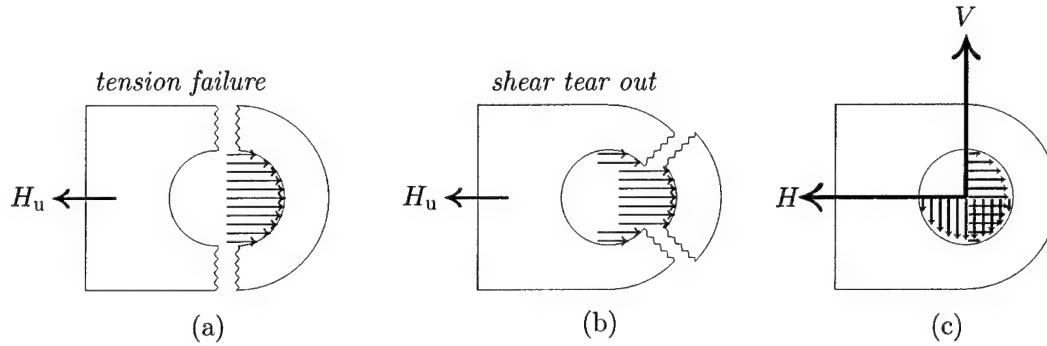


Figure 6.2: *Relevant failure modes of a lug: (a) tension and (b) shear tear out. The combined horizontal and vertical loading experienced by the lug is shown in part (c).*

As is shown in Figure 6.2(c), the stabilator lug experiences both horizontal and vertical loading. From the theory of combined stresses (see, for example, Roark [28]), the principal stress will occur either horizontally or vertically and is given by

$$\sigma_{\infty} = \frac{\max(H, V)}{A_{\ell}}, \quad (6.3)$$

where H and V are the horizontal and vertical loads experienced by the lug, and A_{ℓ} is the lug's cross-sectional area.

The areas for the two relevant failure modes (tension and shear tear out) are calculated in the same way. Figure 6.3 shows three zoomed sections from Sikorsky drawing 70209-27001 of the centre-box, see Figure A16 on page 67 (Figure A17 may also be of interest). From Figure 6.3, the relevant cross-sectional area of the top receiving clevis lug (shown in Box C) is

$$A_{\ell} = 4 \times (0.437 \times 0.440) = 0.769 \text{ in}^2. \quad (6.4)$$

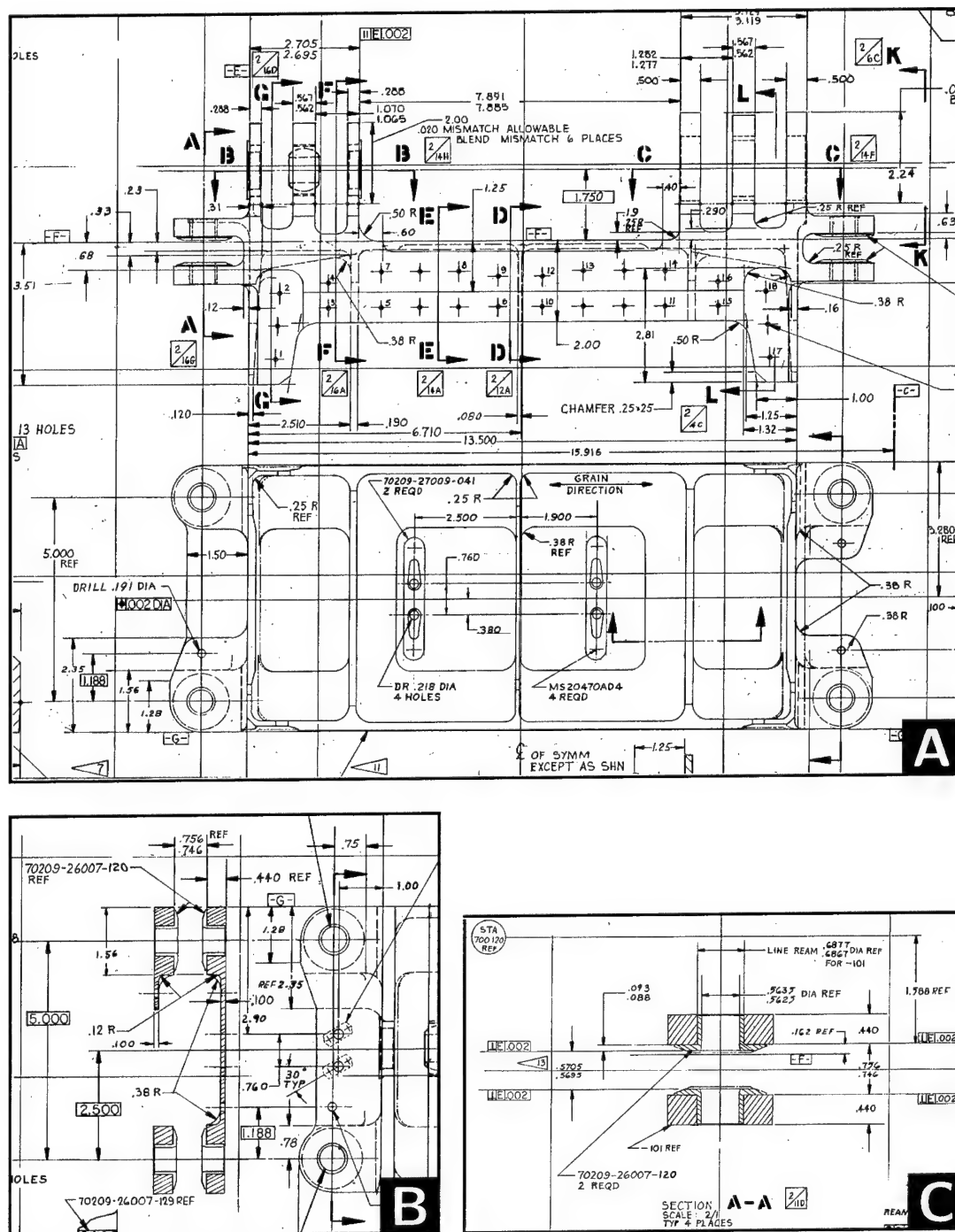


Figure 6.3: Cross-sections showing dimensions of the cracked lug (zoomed sections from Sikorsky drawing 70209-27001). Box A shows the centre-box. Box B shows a vertical cross-section of the cracked lug. Box C shows a horizontal cross-section of the cracked lug.

Concentrating on the forward spar, the horizontal and vertical loads are given respectively by Equations (3.8) and (3.24). The spar's length is $L = 74$ (see page 16), and for bending bridge Number 1, $x_g = 9.2$ (see Figure 2.1) and $h_f = 5.9/2$ (see Table 2.1). Thus the equations for the horizontal and vertical loads simplify to

$$H_f = -0.862\sigma_f \quad (6.5)$$

and

$$V_f = -0.137\sigma_f \quad (6.6)$$

Remember that σ_f is the bending stress on the forward spar (in this case at bending bridge Number 1). The cracked lug is in tension when the bending stress on the spar is negative (see Assumption 2), which explains the negative signs in Equations (6.5) and (6.6). We have used Equation (3.26) in preference to Equation (3.24) to estimate the horizontal load because the former produces the higher loads.¹³

To provide some perspective of our loading calculations we compare the vertical loading given by Equation (6.6) with the design loads that were measured by Sikorsky [9]. We will compare both the maximum and minimum vertical loads.

From Figure 5.1 we see that the maximum bending stress (at bridge Number 1) for the Flight Loads Survey occurs in a manoeuvre from the miscellaneous group. This manoeuvre was a power dive from run 22 of flight 7 (with mnemonic POWER_DIVE_1.2VH) and had a maximum bending stress of -35.0 ksi. Substituting this stress into Equation (6.6) gives the vertical loading on the forward spar as 4800 lb. In the same way¹⁴ we determine the vertical loading on the aft spar as 2470 lb. Adding these two vertical loads gives the maximum vertical loading on the stabilator, which is approximately 7270 lb. According to Sikorsky [9], however, the maximum vertical load on the right stabilator was 1848 lb, which is approximately one-quarter of the 7270 lb load we would predict. We will discuss this discrepancy below.

The minimum bending stress (at bridge Number 1) for the Flight Loads Survey occurs in a rolling pullout manoeuvre. (These minimum stresses are *not* shown in Figure 5.1.) This manoeuvre was from run 42 of flight 29 (with mnemonic ROLL_PULLOUT_0.8VH) and had a minimum bending stress of 24.0 ksi. Using the same procedure as in the previous paragraph, the minimum vertical load on the right stabilator is approximately -4980 lb. The Sikorsky [9] value for the minimum vertical load on the right stabilator was -1552 lb, which is approximately one-third of the -4980 lb load we would predict.

As a consistency check on Sikorsky's loading, two different Sikorsky reports are compared to determine the consistency of the maximum loading values used in the previous two paragraphs. Appendix F gives the details of this consistency check, which shows that the two Sikorsky reports do indeed use consistent stabilator loads.

To summarise, the different vertical loads on right stabilator (obtained by Sikorsky and derived in this report using the Flight Loads Survey) are:

¹³Using Equations (3.24) and (6.6) the alternative value for horizontal loading is $H_f = -0.594\sigma_f$, which is a lower load than the value given by Equation (6.5).

¹⁴Using Equation (3.9) and the value $h_a = 4.9/2$ (from Table 2.1) the vertical loading on the aft spar is given by $V_a = -0.0707\sigma_f$.

- +1848 lb (Sikorsky) or +7270 lb (this report) for the *maximum load* and
- -1552 lb (Sikorsky) or -4980 lb (this report) for the *minimum load*.

There are then three explanations for the different vertical loads shown above: (i) the loads estimates we derive are too conservative, (ii) the Flight Loads Survey measurements are erroneous, or (iii) the stabilator loads experienced by ADF operated Seahawks are significantly different to Sikorsky's test helicopter. It is unclear which of these options is correct, and so we merely note that a difference exists between Sikorsky's and this report's bending stresses.

The difference in maximum vertical load between this report and Sikorsky is significant because of the non-linear relationship between stress and fatigue life. It is common for the gross weight of the Seahawk to be approximately 20 000 lb, and thus the magnitude of the stabilator loads are a significant proportion of the main rotor lift. The maximum vertical loads that Sikorsky use would not fatigue damage the investigated lug. However, the intent of this report was to explore a methodology for airframe fatigue, and not to solve a specific in-service failure. We thus leave further investigation of this discrepancy (of maximum vertical load) for future work.

The "maximum"¹⁵ stress experienced by the cracked lug is determined from Equations (6.3) and (6.4), and (because the horizontal load is greater than the vertical load) from Equation (6.5),

$$\begin{aligned}\sigma_\ell &= H_\ell/A_\ell \\ &= -1.12\sigma_f.\end{aligned}\tag{6.7}$$

In Sections 5.2–5.4 we obtained values for the bending stress on the stabilator's forward spar, see Equations (5.4), (5.5) and (5.7). The stress at the cracked lug can be calculated using these values of stress in Equation (6.7). Substituting the resulting values for lug stress into the cycles to failure formula given by Equation (5.2) yields:

$$N_f = 24 \times 10^3 \quad (\text{for the worst-case loading}), \tag{6.8}$$

$$N_f = 220 \times 10^3 \quad (\text{for the typically high loading}), \tag{6.9}$$

and

$$N_f = \infty \quad (\text{for the best-case loading}). \tag{6.10}$$

Both Equations (6.8) and (6.9) show fewer cycles to failure than the run-out cycles of the MIL-HDBK-5 testing [7, p. 3-406], and hence there are fatigue implications. In contrast, Equation (6.10) shows that the lug's fatigue life is unlimited.

Substituting the loading frequencies given by Equations (6.1) and (6.2) into the cycles to failure given by Equations (6.8) and (6.9), respectively, yield lives of approximately:

- 5 minutes for the *worst-case* scenario,
- 6 hours for the *high-loading* scenario, and
- unlimited hours for the *best-case* scenario.

¹⁵Maximum stress in the sense of the 95th percentile.

It must be remembered that (unlike the worst-case scenario) the high loading scenario is *not necessarily* a conservative bound on fatigue. The life estimate given by the high loading scenario only gives us a feel for the level of conservatism inherent in the worst-case estimate.

The best-case scenario was included in case it resulted in a finite life for the cracked lug, which would have suggested the lug was susceptible to fatigue. As explained in the introduction, little can be said if the worst-case analysis results in a finite component life or if the best-case analysis results in an unlimited life. Both the worst- and best-case scenarios have resulted in the null conclusion.

7 Summary

The aim of this report was to develop a methodology for assessing the fatigue life of helicopter airframe structure. As a demonstrator, we estimated the fatigue life of a centre-box lug found on the Seahawk's stabilator.

A review of this structure's design shows that there was no fatigue damage consideration of the centre-box lug that cracked. The design appears to calculate failure margins based on static loads of the in-service worst-case. Only the stabilator assembly (composed of the wing panels and centre-box) was fatigue tested. The fatigue sensitive points within the stabilator assembly were: (i) the forward spar from the right wing panel and (ii) an aft rivet from the centre-box.

The information required for this fatigue analysis had to be determined indirectly, and so sixteen assumptions were necessary. The two *coarsest assumptions* were:

- that the worst-case loading applies all the time and
- that cycle counting (for fatigue purposes) can be approximated using the frequency decomposition of the loading.

Although probably less accurate, the frequency decomposition assumption is not as important as the worst-case loading assumption for the following reason: The cracked lug was not a lifed component. We then expected the loading estimate for the worst-case to be below the endurance limit for the cracked lug—which was not the case! For loads below the cracked lug's endurance limit, loading cycles would be irrelevant, and thus the worst-case loading assumption is more important than the frequency decomposition assumption. In comparison with these two coarse assumptions, the remaining fourteen assumptions are more accurate.

The estimated fatigue life for the worst-case scenario was low for several reasons, which are all related to the degree of conservatism inherent in the assumptions. Most of these assumptions can be improved by:

- Performing a full fatigue analysis based on loading amplitude and cycle counting of the time-history measurements.
- Or, improving the measurement information on which the fatigue analysis was based.

The first suggested improvement is where the largest gain in accuracy (for the least effort) can be achieved; namely, using a full fatigue analysis to refine the assumption that the worst-case loading is acting all the time and at a relatively high frequency.

Low and unlimited fatigue lives were obtained for the worst- and best-case scenarios, respectively. These two results are what we termed the null conclusion, and so only tentative conclusions can be drawn from these results.

The typically high loading (combined with a loading of medium frequency) increased the fatigue life as compared to the worst-case scenario. However, even under this relaxed scenario the cracked lug was still life limited. Only the best-case scenario resulted in a loading that was below the endurance limit of the cracked lug.

The results for the typically high loading suggest that the cracked lug may be susceptible to fatigue in other Seahawk aircraft. However, this fatigue susceptible conjecture must be tempered by the results from the best-case scenario, which suggest that the component may indeed have an unlimited fatigue life. From an engineering perspective, a component given an unlimited life would imply a high level of conservatism in design. The results we have obtained in this report suggest that this conservatism may *not* be present in the cracked lug. Only a more refined analysis (using the suggestions made throughout this report) could draw a sharper conclusion—either for or against the unlimited life of the cracked lug. It must be stressed, however, that within the fidelity of results obtained so far, the work carried out in this report does *not* conflict with Sikorsky's assessment of an unlimited fatigue life.

Experience of fleet service life provides some background assessment to this analysis. The ADF has a fleet of 52 Hawk-variant helicopters that share the same folding stabilator design, with the fleet leader having accumulated over 3000 flight hours since new. This failure mode in the cracked lug has *not* occurred in any other of these 52 helicopters. Furthermore, using the authors' limited access to failure data no other instance of this failure type was uncovered in the remaining worldwide fleets. This worldwide fleet is composed predominantly of the US Navy's fleet of approximately 300 helicopters, where the fleet leader has reached 10 000 flight hours.

Despite the evidence of stabilator buffeting recorded during the Flight Loads Survey, there is little available operational evidence that suggests that this buffeting commonly manifests itself in extensive fatigue damage to this part of the stabilator. In contrast, however, cracking of the trailing edge skins and excessive wear in the stabilator actuator attachment bushes are both common problems afflicting the Hawk fleet. These common problems were not evident in the fatigue test conducted by Sikorsky but could be expected to be exacerbated by buffeting.

We recommend the refinement of the *fatigue estimation methodology* developed in this report. In particular, this refinement should include:

- a detailed *fractographic study* of the lug's fracture surface (to identify crack growth behaviour), and
- a fatigue life calculation based on *cycle-counting* of the Flight Loads Survey data.

However, since both these activities are resource intensive, the scheduling for such work is dependent upon a review of current priorities.

Acknowledgements

We would like to thank some colleagues at DSTO for useful discussions during the course of this work. Both Chris Knight and Domenico Lombardo proved useful sounding boards for both general approaches and specific problems. Rohan Byrnes provided us with some of the photographs of the cracked lug, some material specifications, and the coordinates of the crack striations. Both Noel Goldsmith and Rohan Byrnes provided us with advice on material behaviour. We thank both Ian Anderson and Phil Jackson for vetting a draft of this report, and Phil Jackson for highlighting the importance of using the correct stress intensity factor in choosing the fatigue curve. Finally, we would like to extend our sincere thanks to Soon-Aik Gan for carefully checking not only the mathematical and numerical results, but also for checking our grammar and prose.

References

1. *Test report for fatigue substantiation of SH-60B structural components*, Tech. Report Revision 10, SER-520203, Sikorsky, (Revision 12 is dated 1995). (Section H: Stabilator, Stabilator Actuator and Attachment Hardware.)
2. M. ABRAMOWITZ AND I. A. STEGUN, eds, *Handbook of Mathematical Functions with Formulas, Graphs, and Mathematical Tables*, Dover, 9th edn, December 1972.
3. R. BOYKETT AND C. FEALY, *Testing 'down-under': lessons learned on Black Hawk flight loads survey*, in Proceedings of the American Helicopter Society's 57th Annual Forum, Washington, DC, May 2001.
4. E. F. BRUHN, *Analysis and Design of Flight Vehicle Structures*, Jacobs, 1973.
5. R. BYRNES, *Interim report on RAN Seahawk stabilator centre box lug failure*. Air Vehicles Division, DSTO Minute, MET/046/2003, 9 July 2003.
6. R. BYRNES, *Investigation of a failed RAN Seahawk centre stabilator forward attachment fitting lug*, Aircraft Forensic Engineering Investigation Report DSTO-DP-0827, Defence Science and Technology Organisation, October 2003.
7. DEPARTMENT OF DEFENSE, *Military Handbook: Metallic Materials and Elements for Aerospace Vehicle Structures, MIL-HDBK-5J*, January 2003.
8. D. FRIEND, *Joint USAF-ADF S-70A-9 flight test program, equipment and instrumentation installation report*, GTRI Project A-6048 (Final Report), Georgia Tech Research Institute, April 2000. (USAF contract number: F09603-99-G-0004-004.)
9. P. GALE, *RAN S-70B-2 flight loads report*, Tech. Report SER-520328, Sikorsky Aircraft, May 1986. (Contract No. 70F10009, CAPO No. C218259.)
10. P. M. GERHART AND R. J. GROSS, *Fundamentals of Fluid Mechanics*, Addison-Wesley, 1985.
11. A. S. HALL, *An Introduction to the Mechanics of Solids*, Wiley, SI edn, 1973.
12. A. HIGDON, E. H. OHLSEN, W. B. STILES, J. A. WEESE, AND W. F. RILEY, *Mechanics of Materials*, Wiley, 4th edn, 1985.
13. E. L. HOUGHTON AND N. B. CARRUTHERS, *Aerodynamics for Engineering Students*, Arnold, 3rd edn, 1982.
14. C. N. KING AND R. BOYKETT, *Potential for using flight loads survey data for identifying fatigue damaging conditions in Black Hawk and Seahawk*, technical report, Defence Science and Technology Organisation, Melbourne, Australia, to appear.
15. C. N. KING AND D. C. LOMBARDO, *Black Hawk helicopter component fatigue lives: Sensitivity to changes in usage*, Technical Report DSTO-TR-0912, Defence Science and Technology Organisation, Melbourne, Australia, December 1999.

16. L. KRAKE, *Reproduction of SH-60B Seahawk dynamic component safe-life calculations*, Technical Note DSTO-TN-0058, Defence Science and Technology Organisation, Melbourne, Australia, October 1996.
17. C. J. LAWRENCE, *S-70 stabilator center assembly failure technical advice*. Rotary Wing Section, DGTA Minute, October 2003. (References: RWS/4080/A24/07 & RWS 063/03)
18. D. C. LOMBARDO, *Helicopter structures—a review of loads, fatigue design techniques and usage monitoring*, Technical Report 15, AR-007-137, Defence Science and Technology Organisation, Melbourne, Australia, May 1993.
19. S. S. MANSON, *Nonferrous alloys*, in *Aerospace Structural Metals Handbook*, W. F. Brown, Jr., H. Mindlin, and C. Y. Ho, eds, vol. 3, Battelle Columbus Laboratories, Mechanical Properties Data Center, Department of Defense, Purdue University, 1992.
20. T. H. G. MEGSON, *Aircraft Structures for Engineering Students*, Arnold, 2nd edn, 1990.
21. A. B. MEW, *Introduction to the Use of Linear Elastic Fracture Mechanics in Estimating Fatigue Crack Growth Rates and Residual Strength of Components*, Engineering Science Data Sheet (ESDU) 80036, July 1996.
22. F. G. POLANCO, *Usage spectrum perturbation effects on helicopter component fatigue damage and life-cycle costs*, Research Report DSTO-RR-0187, Defence Science and Technology Organisation, Melbourne, Australia, November 2000.
23. W. H. PRESS, S. A. TEUKOLSKY, W. T. VETTERLING, AND B. P. FLANNERY, *Numerical Recipes in C: The Art of Scientific Computing*, Cambridge, 2nd edn, 1992.
24. ROYAL AUSTRALIAN AIR FORCE, *Illustrated Parts Breakdown Manual Black Hawk (Book 3 of 4)*, Defence Instruction (Air Force) AAP 7210.015-4B3, 10 May 1993. (File Reference: ARMYLMS/4560/A25/7210/015/4.)
25. ROYAL AUSTRALIAN AIR FORCE, *Maintenance Manual Black Hawk (Book 7 of 10)*, Defence Instruction (Air Force) AAP 7210.015-2B7, 5 July 1994. (File Reference: ARMYLMS/4560/A25/7210/015-2.)
26. W. T. THOMSON, *Theory of Vibration with Applications*, Allen & Unwin, 3rd edn, 1988.
27. S. WOLFRAM, *The Mathematica Book*, Cambridge, 4th edn, 1999.
28. W. C. YOUNG, *Roark's Formulas for Stress and Strain*, McGraw-Hill, 6th edn, 1989.

Appendix A Engineering Drawings

This appendix contains engineering drawings of some stabilator components. Each caption gives the drawing number (dn), sheet number (sht:X of Y), and filename (f) of the drawing. For example, the caption in Figure A5 has the code (dn:70202-07051, sht:1 of 2, rev:K, f:0003658A.CAL), which stands for revision *K* of sheet 1 (of two sheets) from drawing number *70202-07051*, with associated filename 0003658A.CAL.

In October 2003, these drawings were available on the Air Vehicle Division's network computer, in the directory I:\Black_Hawk_Drawings\SIKORSKY\IMAGES.

The electronic version of this report contains the complete versions of these drawings. Thus any section of these drawings may be zoomed to obtain greater detail.

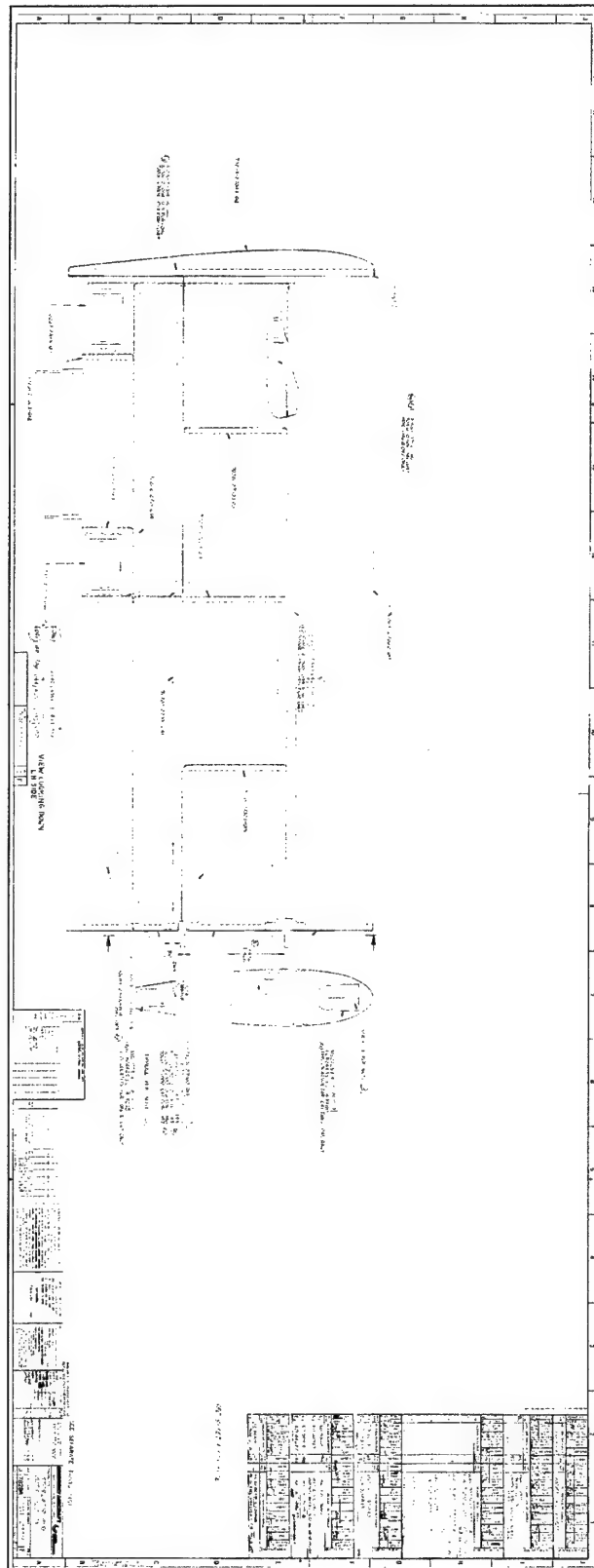


Figure A1: *Horizontal stabilator.*
(dn:70200-27001, sht:2 of 4, rev:F, f:0003513A.CAL)

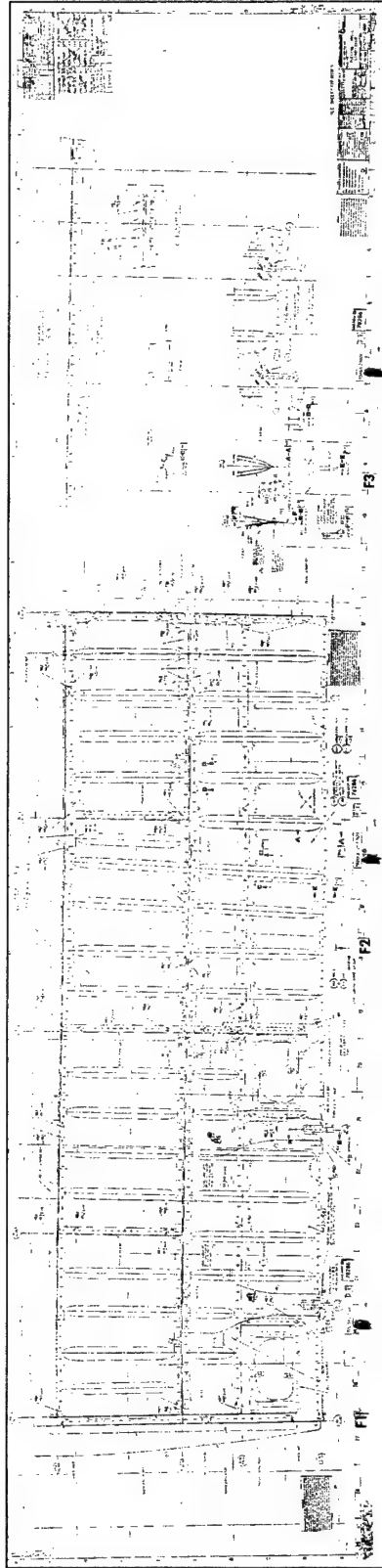


Figure A2: *Top skin of the horizontal stabilator.*
(dn:70203-27001, sht:2 of 4, rev:T, f:0003751A.CAL)

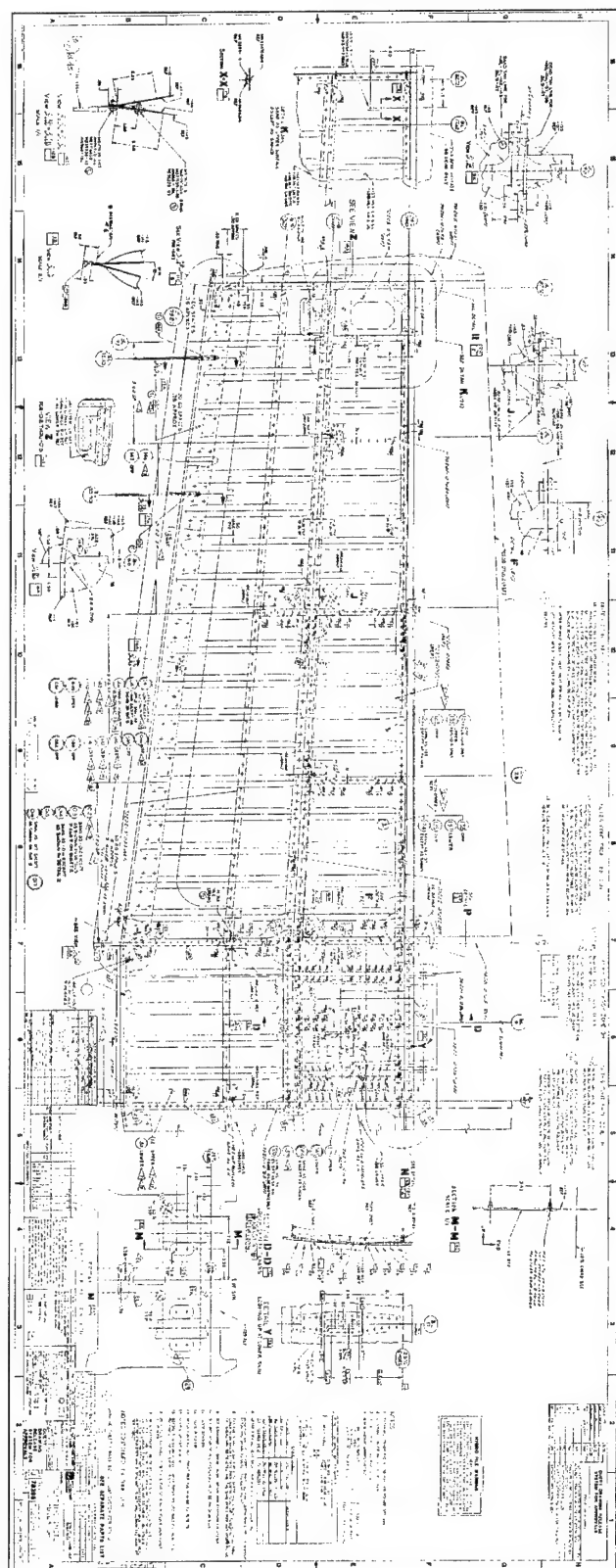
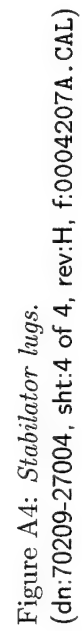


Figure A3: UH-60 (?) top skin of the horizontal stabilator.
(dn:70203-07051, sht:1 of 5, rev:U, f:0003704A.CAL)



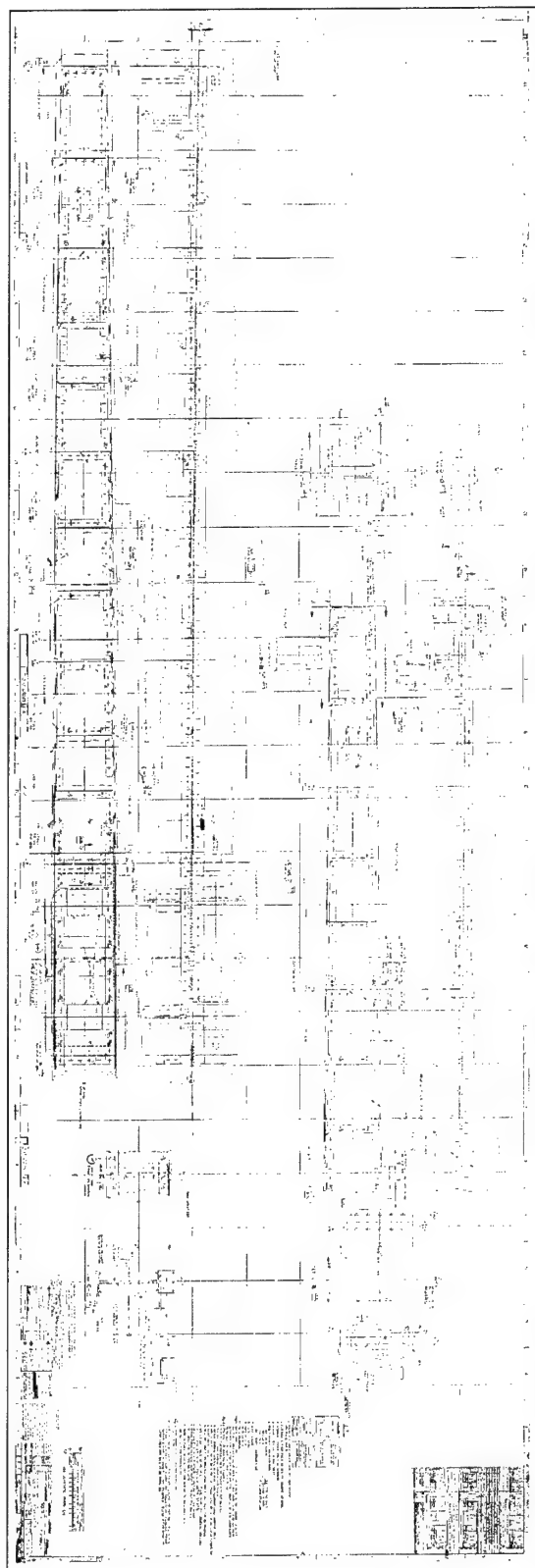


Figure A5: *Forward spar of the port side stabilator.*
(dn:70202-07051, sht:1 of 2, rev:K, f:0003658A.CAL)

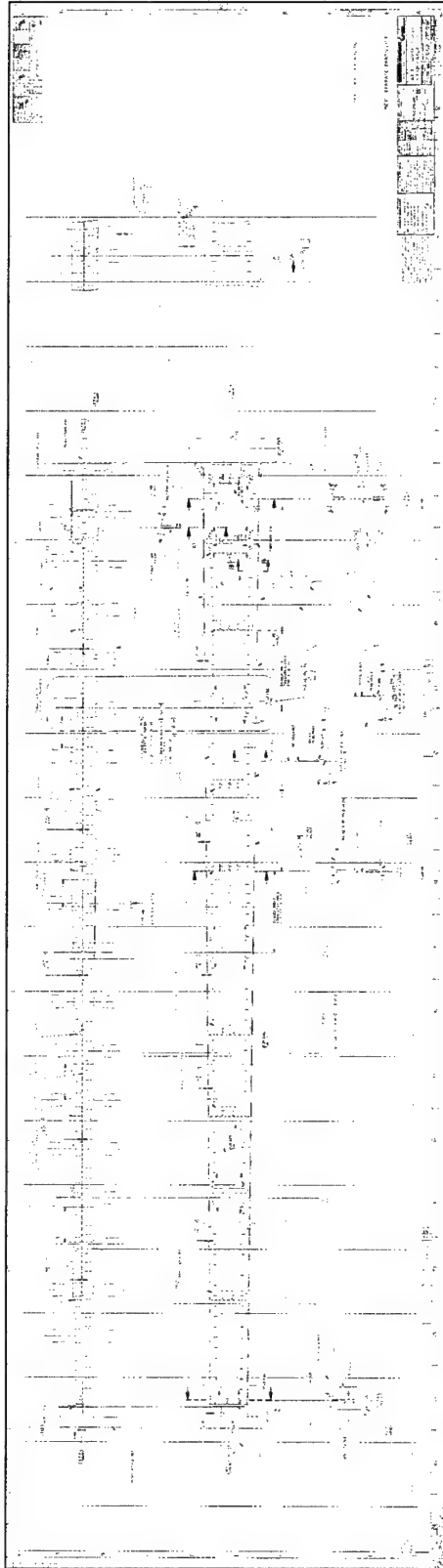


Figure A6: *Aft spar of the port side stabilizer.*
(dn:70202-27001, sht:2 of 2, rev:F, f:0003690A.CAL)

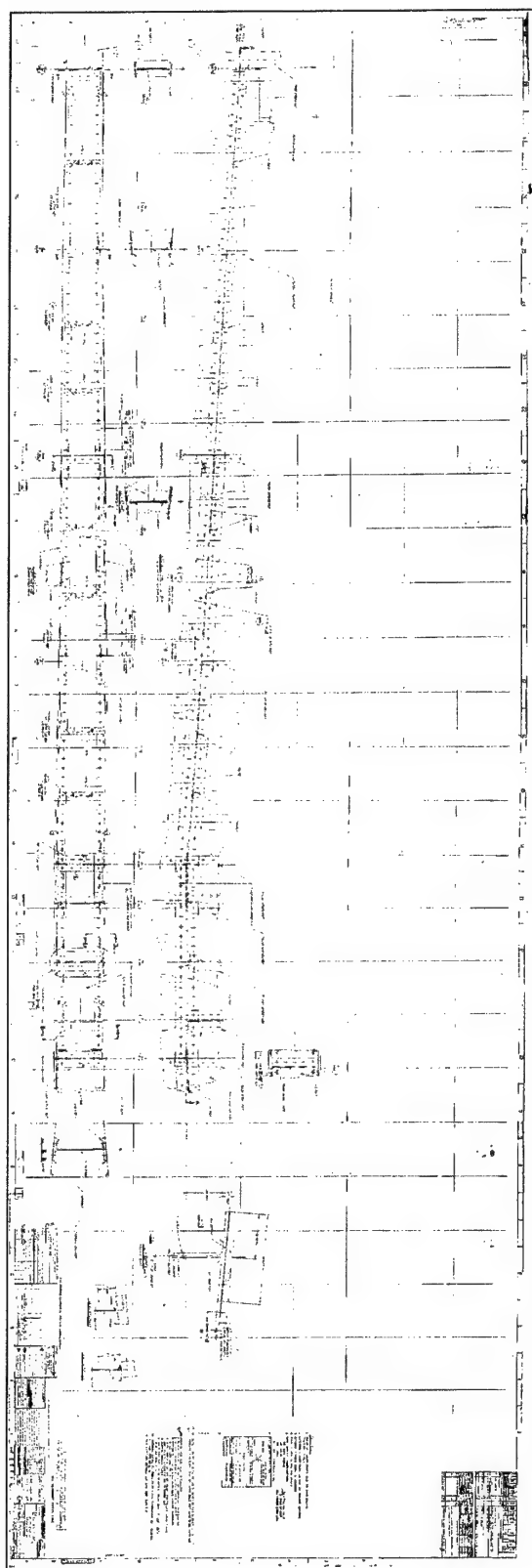
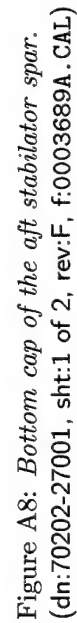


Figure A7: UH-60 (?) aft spar of the port side stabilator.
(dn:70202-07052, sht:1 of 2, rev:G, f:0003660A.CAL)



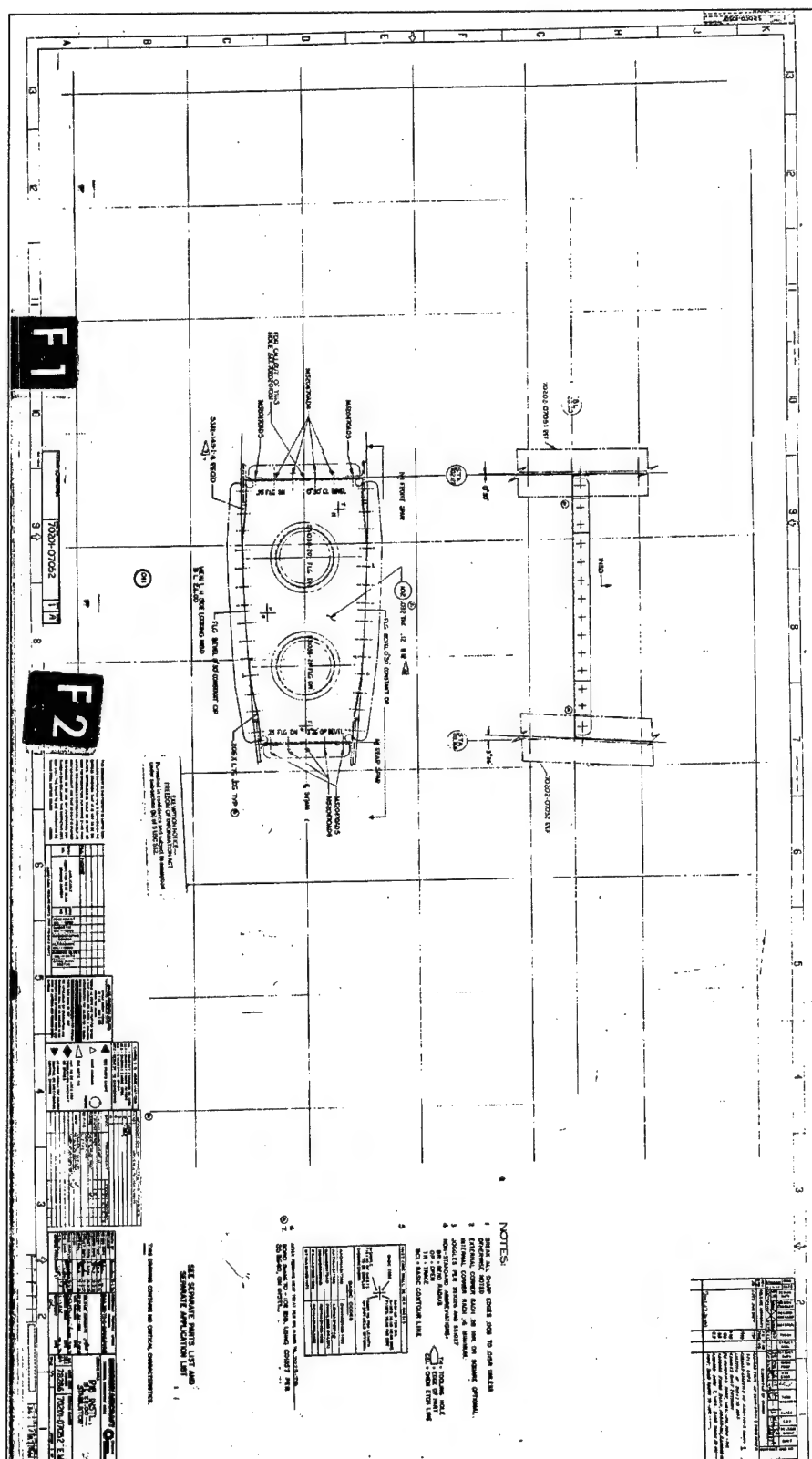


Figure A9: Rib of stabilator at BL 28.
(dn:70201-07052, sht:1 of 1, rev:A, f:0003568A.CAL)

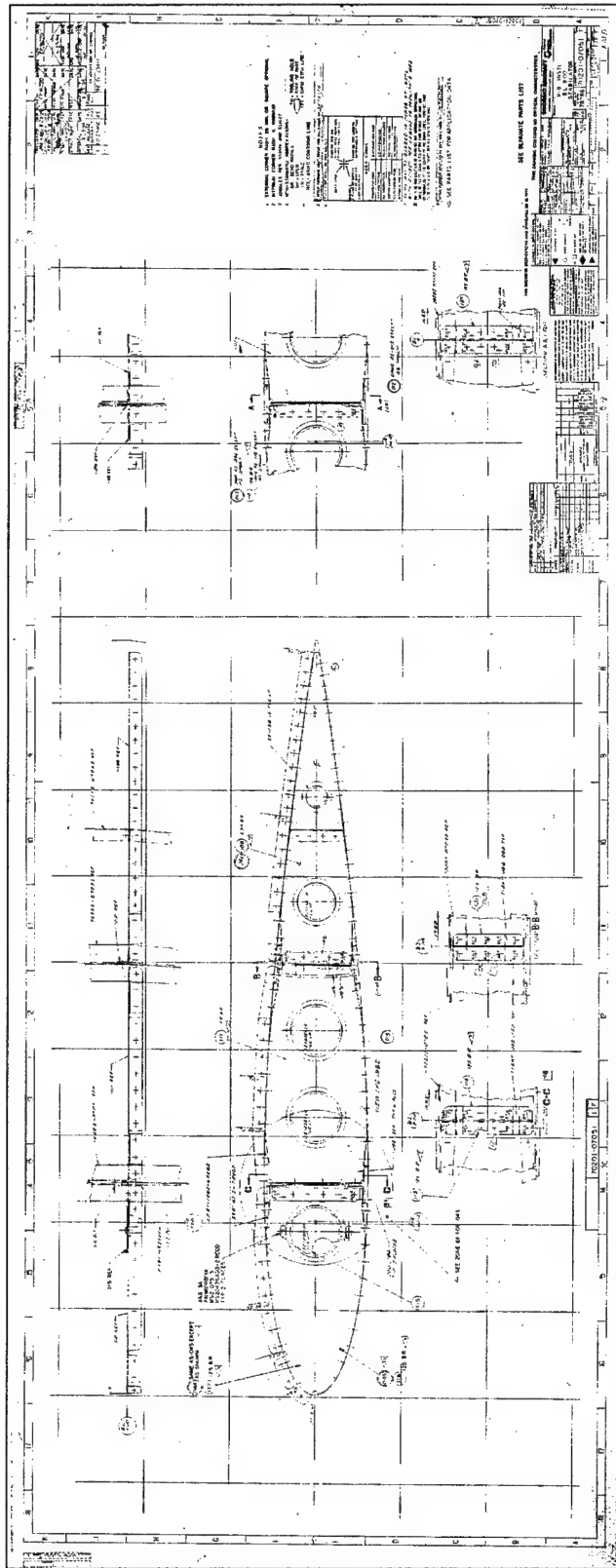


Figure A10: Rib of stabilator at BL 9.
(dn:70201-07051, sht:1 of 1, rev:F, f:0003567A.CAL)

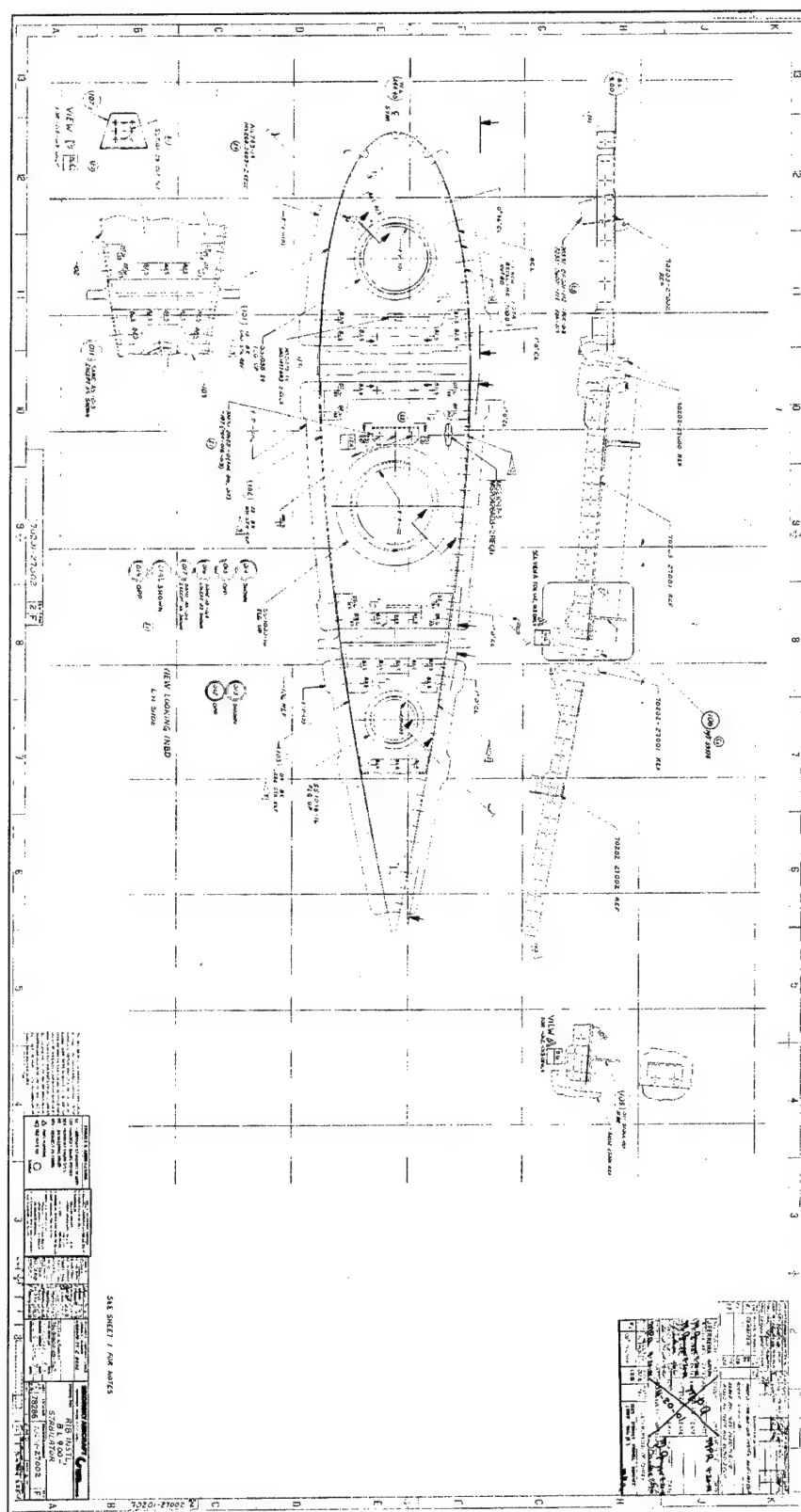


Figure A11: *Rib of stabilator at BL 9, including view of lugs.*
(dn:70201-27002, sht:2 of 2, rev:F, f:0003596A.CAL)

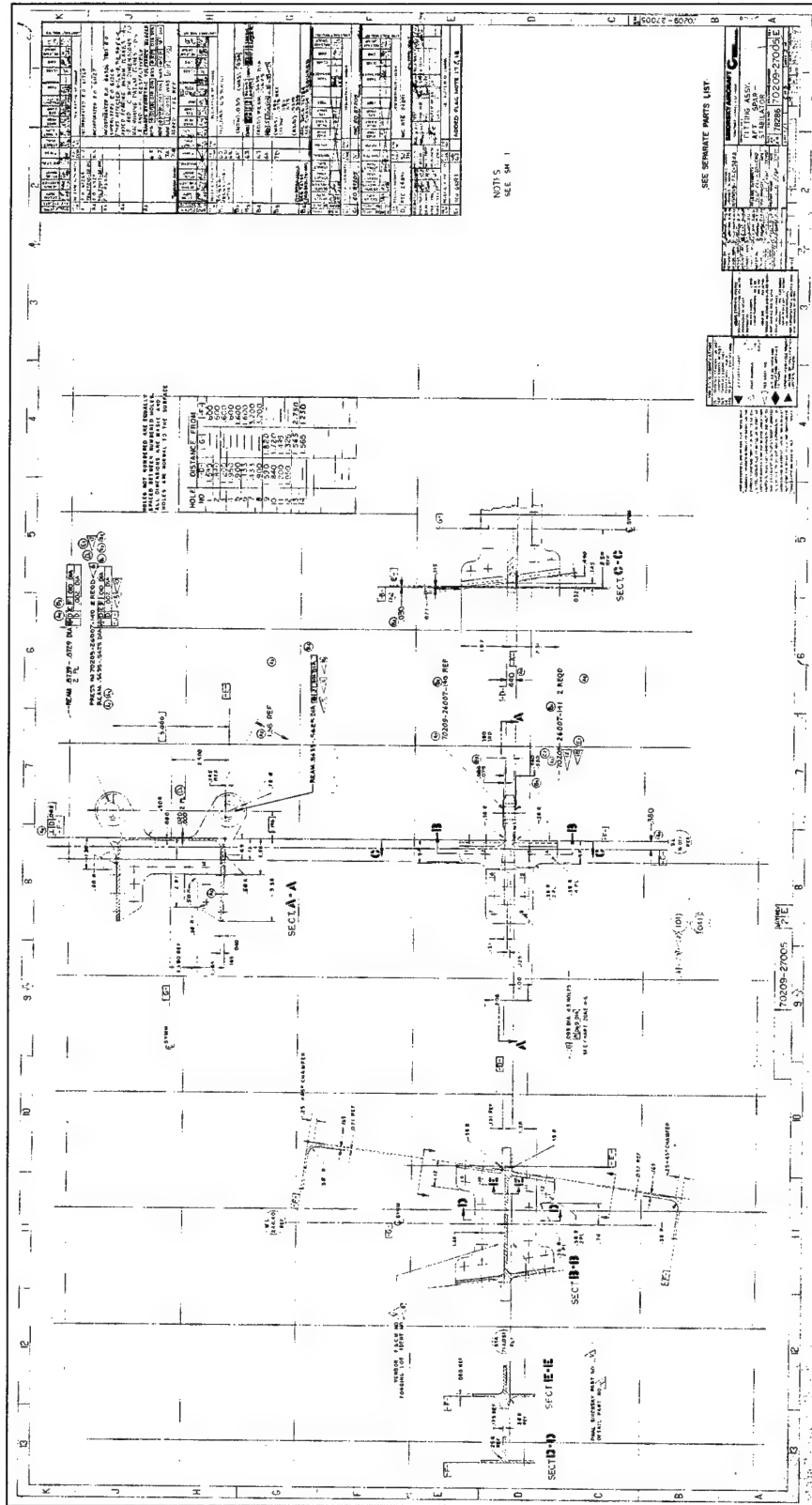
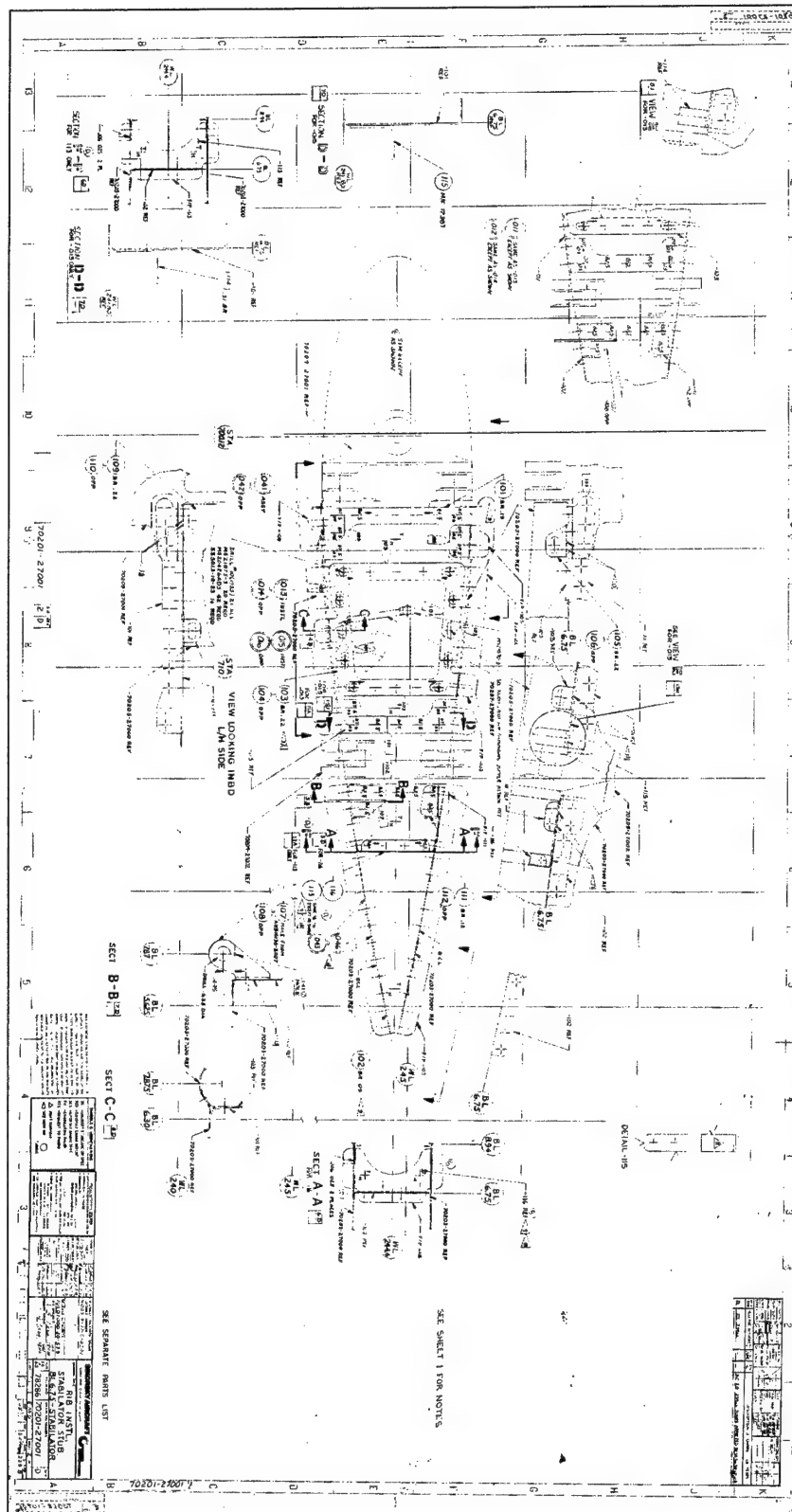


Figure A12: Lugs of aft stabilator spar.
(dn:70209-27005, sht:2 of 3, rev:E, f:0004209A.CAL)

Figure A13: *Rib of stabilator at BL 6.75 (centre-box section).*
(dn:70201-27001, sht:2 of 2, rev:D, f:0003594A.CAL)



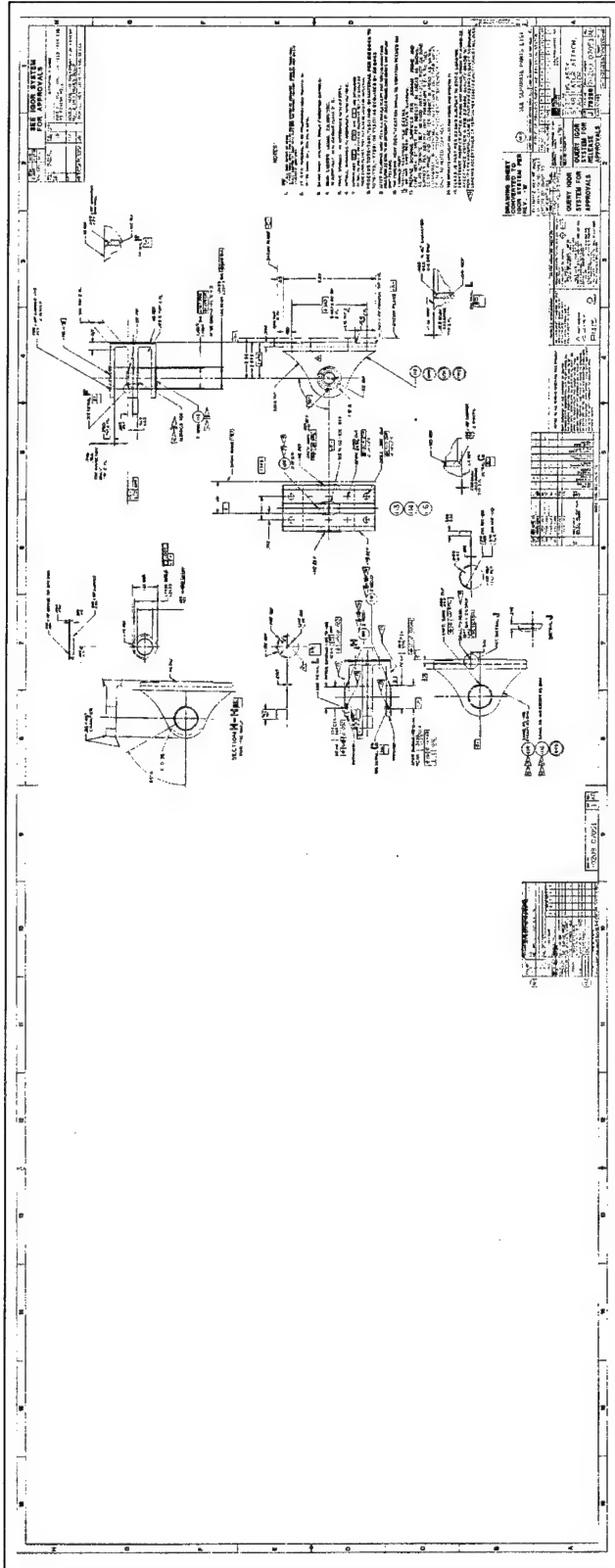


Figure A14: Stabilizer attaching lug (centre-box section).
(dn:70209-07051, sht:1 of 3, rev:AB, f:0004136A.CAL)

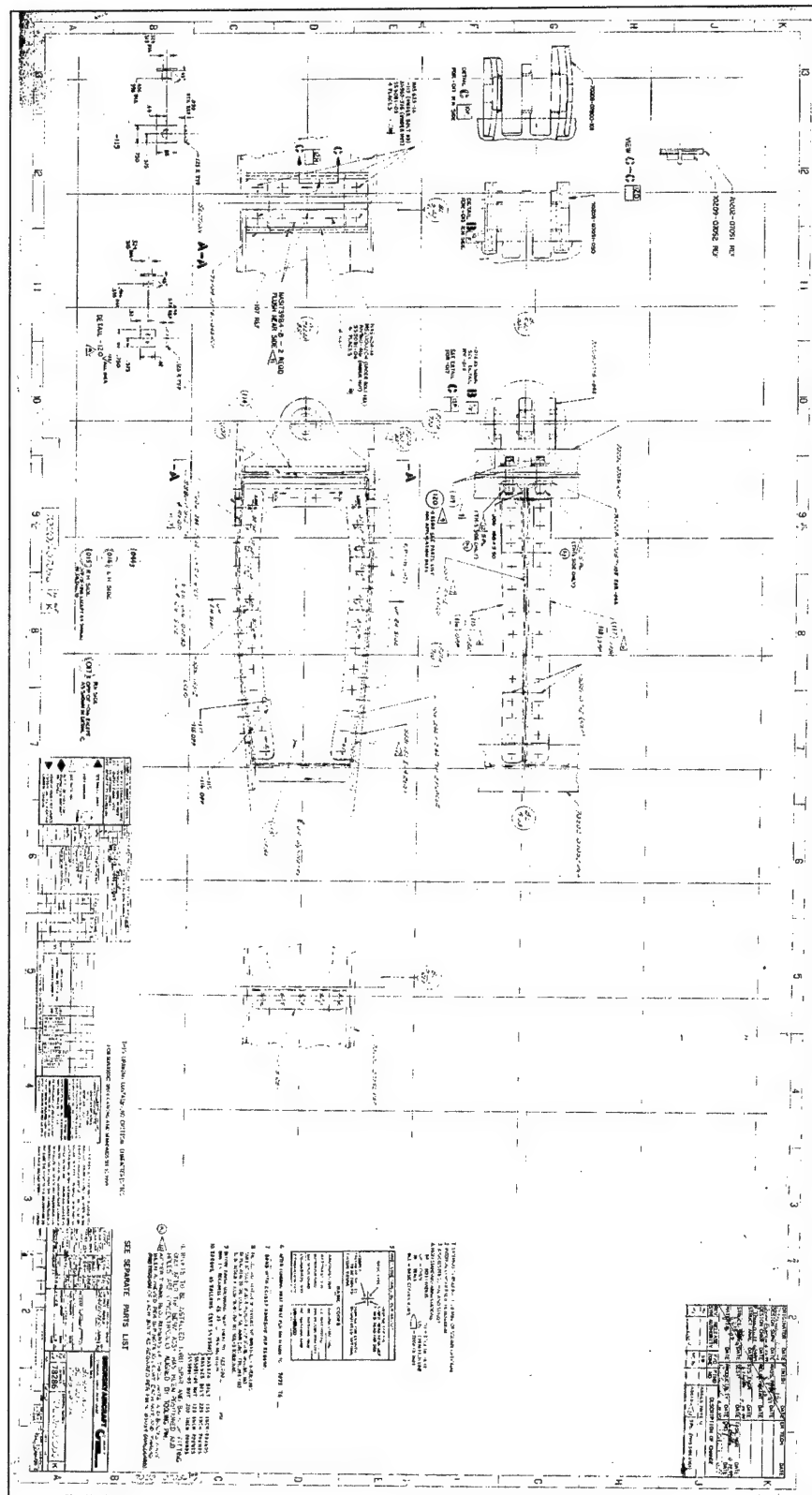


Figure A15: Stabilator beam at BL 5.40 (centre-box section).
(dn:70201-07056, sht:1 of 1, rev:K, f:0003574A.CAL)

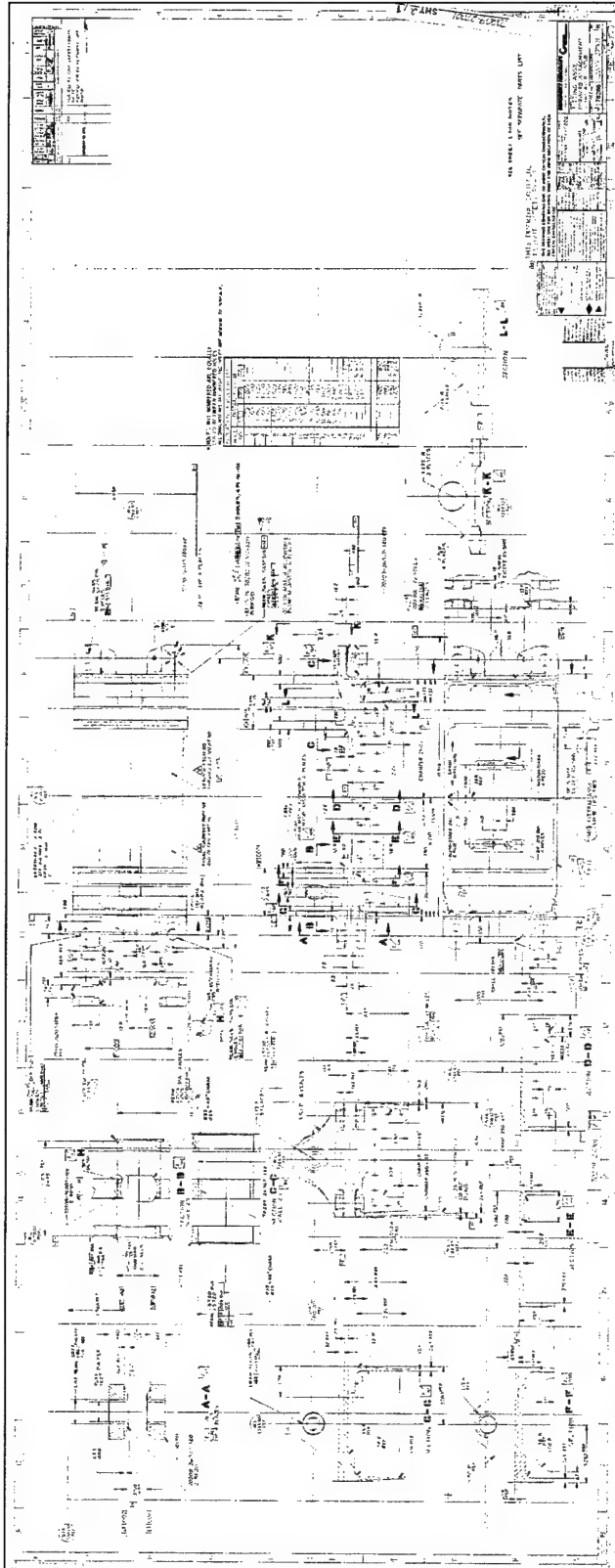


Figure A16: Centre-box attachment for forward spars (Sheet 2).
(dn:70209-27001, sht:2 of 7, rev:K, f:0004188A.CAL)



Appendix B Twelve Manoeuvre Groups

This appendix lists the twelve groups into which the manoeuvres from the Flight Loads Survey were partitioned (see Section 4.1 for further details).

Table B1: List of manoeuvres in the autos group.

Autos		
auto_desc, vbroc, 120%nr	auto_desc, vma, 120%nr	auto_turn_lt, .8vma, 30deg
auto_desc, vbroc, 92%nr	auto_desc, vma, 92%nr	auto_turn_lt, .8vma, 45deg
auto_desc, vvh, 100%nr	auto_entry, .8vh	auto_turn_lt, vma, 30deg
auto_desc, .8vh, 100%nr	auto_entry, .8vma	auto_turn_lt, vma, 45deg
auto_desc, .8vh, 116%nr	auto_entry, vvh	auto_turn_rt, .8vh, 30deg
auto_desc, .8vh, 120%nr	auto_entry, vma	auto_turn_rt, .8vh, 45deg
auto_desc, .8vh, 92%nr	auto_recvry, .8vh	auto_turn_rt, .8vma, 15deg
auto_desc, .8vma, 100%nr	auto_recvry, .8vma	auto_turn_rt, .8vma, 30deg
auto_desc, .8vma, 120%nr	auto_recvry, vvh	auto_turn_rt, .8vma, 45deg
auto_desc, .8vma, 92%nr	auto_recvry, vma	auto_turn_rt, vma, 30deg
auto_desc, vma, 100%nr	auto_turn_lt, .8vh, 30deg	auto_turn_rt, vma, 45deg
auto_desc, vma, 108%nr	auto_turn_lt, .8vh, 45deg	
auto_desc, vma, 112%nr	auto_turn_lt, .8vma, 15deg	

Table B2: List of manoeuvres in the climb group.

Climb		
climb, vbroc, irp	cltrn_lt_30, vbroc, mcp	cltrn_rt_15, vbroc+15, mcp
climb, vbroc, mcp	cltrn_lt_30, vbroc+15, mcp	cltrn_rt_30, vbroc, irp
climb, vbroc+15, irp	cltrn_lt_45, vbroc, irp	cltrn_rt_30, vbroc, mcp
climb, vbroc+15, mcp	cltrn_lt_45, vbroc, mcp	cltrn_rt_30, vbroc+15, mcp
climb, vbroc-15, irp	cltrn_lt_45, vbroc+15, irp	cltrn_rt_45, vbroc, irp
climb, vbroc-15, mcp	cltrn_lt_45, vbroc+15, mcp	cltrn_rt_45, vbroc, mcp
cltrn_lt_15, vbroc, irp	cltrn_lt_45, vbroc-15, irp	cltrn_rt_45, vbroc+15, irp
cltrn_lt_15, vbroc, mcp	cltrn_lt_45, vbroc-15, mcp	cltrn_rt_45, vbroc+15, mcp
cltrn_lt_15, vbroc+15, irp	cltrn_rt_15, vbroc, irp	cltrn_rt_45, vbroc-15, irp
cltrn_lt_15, vbroc+15, mcp	cltrn_rt_15, vbroc, mcp	cltrn_rt_45, vbroc-15, mcp
cltrn_lt_30, vbroc, irp	cltrn_rt_15, vbroc+15, irp	

Table B3: List of manoeuvres in the hover group.

Hover		
hover_lige, 100%nr	hover_loge, raise_load	hover_turn_left, 15_d/s
hover_loge, 100%nr	hover_loge, set_load	hover_turn_left, 30_d/s
hover_loge, load_extended	hover_loge, set-down_load	hover_turn_right, 15_d/s
hover_loge, lower_load	hover_loge, sling_pickup	hover_turn_right, 30_d/s
hover_loge, pickup_load	hover_loge, with_load	hover_cable_full-up

Table B4: List of manoeuvres in the level flight group.

Level flight		
lev.flt_forward, 0.3vh	lev.flt_fwd, 0.6vh, 95%nr	lev.flt_fwd, 0.9vh, 101%nr
lev.flt_forward, 0.4vh	lev.flt_fwd, 0.6vh, 97%nr	level_flight, 100_kias
lev.flt_forward, 0.5vh	lev.flt_fwd, 0.6vh, 99%nr	level_flight, 60_kias
lev.flt_forward, 0.6vh	lev.flt_fwd, 0.6vh, 101%nr	level_flight, 70_kias
lev.flt_forward, 0.7vh	lev.flt_fwd, 0.9vh, 95%nr	level_flight, 80_kias
lev.flt_forward, 0.8vh	lev.flt_fwd, 0.9vh, 97%nr	level_flight, 90_kias
lev.flt_forward, 0.9vh	lev.flt_fwd, 0.9vh, 99%nr	
lev.flt_forward, 1vh	lev.flt_fwd, 0.9vh, 100%nr	

Table B5: List of manoeuvres in the miscellaneous group.

Miscellaneous		
ambient	lhs_200lbs.&rhs_0lbs	opening_apu_door
appr.runon, 40kt, aero.brk	lhs_400lbs.&rhs_0lbs	power_dive_1.1vh
approach.&runon, 40kt	lhs_400lbs.&rhs_200lbs	power_dive_1.2vh
approach, normal	lhs_400lbs.&rhs_400lbs	ppd, 90kts, 1000fpm
approach, operational	lhs_400lbs.&rhs_600lbs	ppd, 90kts, 1500fpm
approach, rough	lhs_400lbs.&rhs_800lbs	ppd, 90kts, 500fpm
close_apu_door	lhs_400lbs.&rhs_840lbs	ppd, 1vh, 1500fpm
dash.&quickstop	lhs_600lbs.&rhs_840lbs	rcvry_from_part.pwr.desc
e/s/rlt.trn, 8vh, 30deg	lhs_800lbs.&rhs_840lbs	rotor_engagmnt, fly
esss_400l.lhs.&rhs_tank	lhs_860lbs.&rhs_840lbs	rotor_engagmnt, no.brake
esss_400l.lhs.tank	lift.off.to.hover_lige	rotor_engagmnt, brk
esss_400l.lhs/800l.rhs	lsf.accel.&quick-stop	rotor_engagmnt, brk, hard
esss_800l.lhs.&rhs_tank	maintainer.climbing_lhs	rotor_engagmnt, brk, idle
esss_empty_fuel	maintainer.climbing_rhs	rotor_shutdown, no.brake
ilhs_200l.&lrhs_0l	mntnr.stnd.clstd.#1_cowl	rotor_shutdown, brk
ilhs_400l.&lrhs_0l	mntnr.stnd.clstd.#2_cowl	rotor_shutdown, brk, 40%nr
ilhs_400l.&lrhs_200l	mntnr.stnd.lhs.apu_door	rotor_shutdown, brk, hard
ilhs_400l.&lrhs_400l	mntnr.stnd.open.#1_cowl	rsf.accel.&quick-stop
ilhs_400l.&lrhs_600l	mntnr.stnd.open.#2_cowl	rdw.accel.&quick-stop
ilhs_400l.&lrhs_800l	mntnr.stnd.rhs.apu_door	take-off_jump
ilhs_400l.&lrhs_850l	mntnr.walk.clstd.#1_cowl	take-off_normal
ilhs_600l.&lrhs_850l	mntnr.walk.clstd.#2_cowl	take-off_rolling
ilhs_800l.&lrhs_850l	mntnr.walk.on.apu.doors	takeoff, normal
ilhs_850l.&lrhs_850l	mntnr.walk.open.#1_cowl	terrain_cyclic.pull
jump.take-off	mntnr.walk.open.#2_cowl	terrain_cyclic.push
landing, ship	no.1.engine.start	vertical.landing
lhs_0lbs.&rhs_0lbs	no.2.engine.start	

Table B6: List of manoeuvres in the symmetric pullouts group.

Symmetric pullouts		
incl_sym_po,.8vh,lt,2.1g	symm_pullout,.8vh,.1.35g	symm_pushover,.vh,.45g
incl_sym_po,.8vh,lt,2.4g	symm_pullout,.8vh,.1.3g	symm_pushover,.vh,.4g
incl_sym_po,.8vh,lt,2.5g	symm_pullout,.8vh,.1.4g	symm_pushover,.vh,.55g
symm_pullout,.8vh,.1.5g	symm_pullout,.8vh,.1.51g	symm_pushover,.vh,.57g
symm_pullout,.8vh,.1.6g	symm_pullout,.8vh,.1.55g	symm_pushover,.vh,.5g
symm_pullout,.8vh,.1.8g	symm_pullout,.8vh,.1.5g	symm_pushover,.vh,.6g
symm_pushover,.8vh,.25g	symm_pullout,.8vh,.1.65g	symm_pushover,.vh,.75g
symm_pushover,.8vh,.4g	symm_pullout,.8vh,.1.68g	symm_pushover,.vh,.7g
symm_pushover,.8vh,.6g	symm_pullout,.8vh,.1.6g	symm_pushover,.vh,.8g
symm_pullout,.vh,.1.3g	symm_pullout,.8vh,.1.75g	symm_pushover,.8vh,.15g
symm_pullout,.vh,.1.45g	symm_pullout,.8vh,.1.7g	symm_pushover,.8vh,.1g
symm_pullout,.vh,.1.4g	symm_pullout,.8vh,.1.85g	symm_pushover,.8vh,.21g
symm_pullout,.vh,.1.55g	symm_pullout,.8vh,.1.8g	symm_pushover,.8vh,.25g
symm_pullout,.vh,.1.5g	symm_pullout,.8vh,.1.91g	symm_pushover,.8vh,.2g
symm_pullout,.vh,.1.65g	symm_pullout,.8vh,.1.95g	symm_pushover,.8vh,.35g
symm_pullout,.vh,.1.6g	symm_pullout,.8vh,.1.9g	symm_pushover,.8vh,.38g
symm_pullout,.vh,.1.73g	symm_pullout,.8vh,.2.0g	symm_pushover,.8vh,.3g
symm_pullout,.vh,.1.75g	symm_pullout,.8vh,.2.1g	symm_pushover,.8vh,.45g
symm_pullout,.vh,.1.85g	symm_pullout,.8vh,.2.2g	symm_pushover,.8vh,.47g
symm_pullout,.vh,.1.8g	symm_pushover,.vh,.1g	symm_pushover,.8vh,.4g
symm_pullout,.vh,.1.9g	symm_pushover,.vh,.21g	symm_pushover,.8vh,.57g
symm_pullout,.vh,.2.0g	symm_pushover,.vh,.25g	symm_pushover,.8vh,.5g
symm_pullout,.vh,.2.1g	symm_pushover,.vh,.2g	symm_pushover,.8vh,.6g
symm_pullout,.8vh,.1.25g	symm_pushover,.vh,.35g	symm_pushover,.8vh,.7g
	symm_pushover,.vh,.3g	

Table B7: List of manoeuvres in the rolling pullouts group.

Rolling pullouts		
roll_po_(verify)	roll_po.lt,.8vh,.1.3g	roll_po.rt,.8vh,.1.8g
roll_po.lt,.8vh	roll_po.lt,.8vh,.1.45g	roll_po.rt,.8vh,.1.95g
roll_po.lt,.8vh,.1.25g	roll_po.lt,.8vh,.1.4g	roll_po.rt,.8vh,.1.9g
roll_po.lt,.8vh,.1.35g	roll_po.lt,.8vh,.1.55g	roll_po.rt,.8vh,.2.0g
roll_po.lt,.8vh,.1.3g	roll_po.lt,.8vh,.1.5g	roll_po.rt,.8vh,.2.1g
roll_po.lt,.8vh,.1.4g	roll_po.lt,.8vh,.1.65g	roll_po.rt,.8vh,.2.2g
roll_po.lt,.8vh,.1.55g	roll_po.lt,.8vh,.1.6g	roll_po.rt,.8vh,.2.3g
roll_po.lt,.8vh,.1.5g	roll_po.lt,.8vh,.1.75g	roll_po.rt,.8vh,.2.4g
roll_po.lt,.8vh,.1.65g	roll_po.lt,.8vh,.1.7g	roll_po.rt,.8vh,.1.25g
roll_po.lt,.8vh,.1.6g	roll_po.lt,.8vh,.1.85g	roll_po.rt,.8vh,.1.2g
roll_po.lt,.8vh,.1.75g	roll_po.lt,.8vh,.1.8g	roll_po.rt,.8vh,.1.35g
roll_po.lt,.8vh,.1.7g	roll_po.lt,.8vh,.1.95g	roll_po.rt,.8vh,.1.3g
roll_po.lt,.8vh,.1.85g	roll_po.lt,.8vh,.1.9g	roll_po.rt,.8vh,.1.45g
roll_po.lt,.8vh,.1.8g	roll_po.lt,.8vh,.2.0g	roll_po.rt,.8vh,.1.4g
roll_po.lt,.8vh,.1.95g	roll_po.lt,.8vh,.2.2g	roll_po.rt,.8vh,.1.55g
roll_po.lt,.8vh,.1.9g	roll_po.rt,.8vh,.1.25g	roll_po.rt,.8vh,.1.56g
roll_po.lt,.8vh,.2.0g	roll_po.rt,.8vh,.1.3g	roll_po.rt,.8vh,.1.5g
roll_po.lt,.8vh,.2.12g	roll_po.rt,.8vh,.1.45g	roll_po.rt,.8vh,.1.65g
roll_po.lt,.8vh,.2.1g	roll_po.rt,.8vh,.1.4g	roll_po.rt,.8vh,.1.6g
roll_po.lt,.8vh,.2.25g	roll_po.rt,.8vh,.1.55g	roll_po.rt,.8vh,.1.75g
roll_po.lt,.8vh,.2.2g	roll_po.rt,.8vh,.1.5g	roll_po.rt,.8vh,.1.77g
roll_po.lt,.8vh,.2.3g	roll_po.rt,.8vh,.1.65g	roll_po.rt,.8vh,.1.7g
roll_po.lt,.8vh,.2.4g	roll_po.rt,.8vh,.1.6g	roll_po.rt,.8vh,.1.85g
roll_po.lt,.8vh,.1.25g	roll_po.rt,.8vh,.1.75g	roll_po.rt,.8vh,.1.8g
roll_po.lt,.8vh,.1.2g	roll_po.rt,.8vh,.1.77g	roll_po.rt,.8vh,.2.0g
roll_po.lt,.8vh,.1.35g	roll_po.rt,.8vh,.1.7g	rt.roll_pullup.vh.1.5g

Table B8: List of manoeuvres in the reversal group.

Reversal		
col.rev.auto,.8vh,100%nr	lat.rev.lev.flt,.8vh	long.rev.hover
col.rev.auto,vma,100%nr	lat.rev.lev.flt,.8vh	rud.rev.auto,.8vh,100%nr
col.rev.lev.flt,.8vh	lat.rev.hover	rud.rev.auto,vma,100%nr
col.rev.lev.flt,.8vh	lng.rev.auto,.8vh,100%nr	rudd.rev.lev.flt,.8vh
col.rev.hover	lng.rev.auto,vma,100%nr	rudd.rev.lev.flt,.8vh
lat.rev.auto,.8vh,100%nr	long.rev.lev.flt,.8vh	rudd.rev.hover
lat.rev.auto,vma,100%nr	long.rev.lev.flt,.8vh	

Table B9: List of manoeuvres in the side and rearward flight group.

Side and rearward flight		
lt_side_flt_accel, 10kts	rearward_flt, 20kts	rt_side_flt_accel, 45kts
lt_side_flt_accel, 20kts	rearward_flt, 30kts	side_flt_left, 10kts
lt_side_flt_accel, 30kts	rearward_flt, 35kts	side_flt_left, 20kts
lt_side_flt_accel, 35kts	rearward_flt, 40kts	side_flt_left, 30kts
lt_side_flt_accel, 40kts	rearward_flt, 45kts	side_flt_left, 35kts
lt_side_flt_accel, 45kts	recovry_left_side_flt	side_flt_left, 40kts
rear_flt_accel, 10kts	recovry_rearward_flight	side_flt_left, 45kts
rear_flt_accel, 20kts	recovry_right_side_flt	side_flt_right, 10kts
rear_flt_accel, 25kts	rt_side_flt_accel, 10kts	side_flt_right, 20kts
rear_flt_accel, 30kts	rt_side_flt_accel, 20kts	side_flt_right, 25kts
rear_flt_accel, 35kts	rt_side_flt_accel, 25kts	side_flt_right, 30kts
rear_flt_accel, 40kts	rt_side_flt_accel, 30kts	side_flt_right, 35kts
rear_flt_accel, 45kts	rt_side_flt_accel, 35kts	side_flt_right, 40kts
rearward_flt, 10kts	rt_side_flt_accel, 40kts	side_flt_right, 45kts

Table B10: List of manoeuvres in the sideslip group.

Sideslip		
sideslip_lt, 0.6vh, 10deg	sideslip_lt, 0.9vh, 5deg	sideslip_rt, 0.8vh, 20deg
sideslip_lt, 0.6vh, 15deg	sideslip_lt, 0.9vh, 10deg	sideslip_rt, 0.8vh, 25deg
sideslip_lt, 0.6vh, 20deg	sideslip_lt, 0.9vh, 15deg	sideslip_rt, 0.8vh, 30deg
sideslip_lt, 0.6vh, 25deg	sideslip_rt, 0.6vh, 10deg	sideslip_rt, 0.9vh, 10deg
sideslip_lt, 0.6vh, 30deg	sideslip_rt, 0.6vh, 15deg	sideslip_rt, 0.9vh, 15deg
sideslip_lt, 0.8vh, 10deg	sideslip_rt, 0.6vh, 20deg	sideslip_trim, 0.6vh
sideslip_lt, 0.8vh, 15deg	sideslip_rt, 0.6vh, 25deg	sideslip_trim, 0.8vh
sideslip_lt, 0.8vh, 20deg	sideslip_rt, 0.6vh, 30deg	sideslip_trim, 0.8vh
sideslip_lt, 0.8vh, 22deg	sideslip_rt, 0.8vh, 5deg	sideslip_trim, 0.9vh
sideslip_lt, 0.8vh, 25deg	sideslip_rt, 0.8vh, 10deg	
sideslip_lt, 0.8vh, 30deg	sideslip_rt, 0.8vh, 15deg	

Table B11: List of manoeuvres in the taxi group.

Taxi		
air_taxi_accel, 20kts	air_taxi_fwd, ige, 20kts	taxi_start
air_taxi_accel, 30kts	air_taxi_fwd, ige, 30kts	taxi_stop
air_taxi_accel, 40kts	air_taxi_fwd, ige, 40kts	taxi_straight
air_taxi_accel, 50kts	air_taxi_fwd, ige, 50kts	taxi_turn_left
air_taxi_fwd, ige, 10kts	air_taxi_recovry	taxi_turn_right

Table B12: List of manoeuvres in the turns group.

Turns		
desc_trn_lt,90kts,15deg	entry_rt_tn,vh,50deg	recovry_rt_tn,vh,55deg
desc_trn_lt,90kts,30deg	entry_rt_tn,vh,55deg	recovry_rt_tn,vh,60deg
desc_trn_lt,90kts,45deg	entry_rt_tn,vh,60deg	stdyturn_lt,.8vh,15deg
desc_trn_rt,90kts,15deg	rapid_decel_turn,left	stdyturn_lt,.8vh,30deg
desc_trn_rt,90kts,30deg	rapid_decel_turn,right	stdyturn_lt,.8vh,45deg
desc_trn_rt,90kts,45deg	recovry_lt_tn,.8vh,15deg	stdyturn_lt,.8vh,50deg
entry_lt_tn,.8vh,15deg	recovry_lt_tn,.8vh,30deg	stdyturn_lt,.8vh,55deg
entry_lt_tn,.8vh,30deg	recovry_lt_tn,.8vh,45deg	stdyturn_lt,.8vh,60deg
entry_lt_tn,.8vh,45deg	recovry_lt_tn,.8vh,50deg	stdyturn_lt,vh,15deg
entry_lt_tn,.8vh,50deg	recovry_lt_tn,.8vh,55deg	stdyturn_lt,vh,30deg
entry_lt_tn,.8vh,55deg	recovry_lt_tn,.8vh,60deg	stdyturn_lt,vh,45deg
entry_lt_tn,.8vh,60deg	recovry_lt_tn,vh,15deg	stdyturn_lt,vh,50deg
entry_lt_tn,vh,15deg	recovry_lt_tn,vh,30deg	stdyturn_lt,vh,55deg
entry_lt_tn,vh,30deg	recovry_lt_tn,vh,45deg	stdyturn_lt,vh,60deg
entry_lt_tn,vh,45deg	recovry_lt_tn,vh,50deg	stdyturn_rt,.8vh,15deg
entry_lt_tn,vh,50deg	recovry_lt_tn,vh,55deg	stdyturn_rt,.8vh,30deg
entry_lt_tn,vh,55deg	recovry_lt_tn,vh,60deg	stdyturn_rt,.8vh,45deg
entry_lt_tn,vh,60deg	recovry_rt_tn,.8vh,15deg	stdyturn_rt,.8vh,50deg
entry_rt_tn,.8vh,15deg	recovry_rt_tn,.8vh,30deg	stdyturn_rt,.8vh,55deg
entry_rt_tn,.8vh,30deg	recovry_rt_tn,.8vh,45deg	stdyturn_rt,.8vh,60deg
entry_rt_tn,.8vh,45deg	recovry_rt_tn,.8vh,50deg	stdyturn_rt,vh,15deg
entry_rt_tn,.8vh,50deg	recovry_rt_tn,.8vh,55deg	stdyturn_rt,vh,30deg
entry_rt_tn,.8vh,55deg	recovry_rt_tn,.8vh,60deg	stdyturn_rt,vh,45deg
entry_rt_tn,.8vh,60deg	recovry_rt_tn,vh,15deg	stdyturn_rt,vh,50deg
entry_rt_tn,vh,15deg	recovry_rt_tn,vh,30deg	stdyturn_rt,vh,55deg
entry_rt_tn,vh,30deg	recovry_rt_tn,vh,45deg	stdyturn_rt,vh,60deg
entry_rt_tn,vh,45deg	recovry_rt_tn,vh,50deg	

Appendix C Mathematica Code for Bending Stress Plots

This appendix contains the code used to generate the bending stress plots shown in Section 5.3 and in Appendix D. The Mathematica code is listed in Figures C1–C7. In both the group plots (shown in Figure C6) and the manoeuvre plots (shown in Figure C7) only the first plot from the set of twelve plots is shown. Each of these cells was collapsed since these plots are shown elsewhere in this report (see Appendix D).

stabStrain2.nb

1

Plots of Stabilator Bending Strain (using data from Black Hawk Flight Loads Survey)

Work carried out for Stabilator lug cracking on Seahawk (Jul -- Aug 2003)

```
In[1]:= << LinearAlgebra`MatrixManipulation`;
        << Graphics`Colors`;
        << Graphics`Graphics3D`;
        << myColors.m;

In[5]:= Off[General::spell1]

In[6]:= SetDirectory[ToFileName[Extract[
        "FileName" /. NotebookInformation[EvaluationNotebook[]], {1}, FrontEnd`FileName]]]

Out[6]:= C:\Data, Black Hawk strain survey\Stabilator\StatData
```

■ Importing Manoeuvre Groups (grouping according to influence on dynamic components)

```
In[7]:= manvDyn = Map[DeleteCases[#, ""] &, Transpose[Import["manvDyn.csv", "CSV"]]];
        Map[Length, manvDyn]

Out[8]:= {38, 33, 16, 23, 81, 75, 79, 21, 43, 32, 16, 81}
```

■ Partitioning Manoeuvres into Groups

```
In[9]:= fnPos[v_, man_] := Module[{pos},
        pos = Position[v, man];
        Flatten[{First[pos], Last[pos]}]
    ]

In[10]:= partitionManv[mtx_, manv_] := Module[{manvCol},
        (* Partitions a matrix into manoeuvres *)
        manvCol = Transpose[mtx][[1]];
        Table[Take[mtx, fnPos[manvCol, manv[i]]], {i, Length[manv]}]
    ]

In[11]:= readGauge[file_] := Module[{srt},
        (* Reading in comma-separated data file *)
        srt[v_] := Sort[v, (#1[[5]] < #2[[5]]) &];
        dat = Map[Take[#, 13] &, Import[file, "CSV"]];
        colNam = dat[[1]];
        Print[TableForm[Transpose[{Range[Length[colNam]], colNam}]]];
        dat = Rest[dat];
        Print["Number of manoeuvres=", Length[manvNam = Union[Transpose[dat][[1]]]]];
        Print["dimensions=", Dimensions[dat]];
        dat = DeleteCases[dat, {a_, "", b_}, ∞];
        statDat = Map[srt, partitionManv[dat, manvNam]];
        Length[statDat]
    ]
```

17:27:53 Thursday, August 7, 2003

Figure C1: Mathematica code for stress plots, Page 1.

stabStrain2.nb

2

```
In[12]:= readGauge["stbnbmlr.csv"]
```

```
1  MANEUVER_DESC
2  AVG_VIB
3  MAX_VIB
4  PCL_VIB
5  AVG_STDY
6  MIN_STDY
7  MAX_STDY
8  ABMIN_STDY
9  ABMAX_STDY
10 PCL_DIR
11 PCC_DIR
12 FLIGHTTEST_NUM
13 RUN_NUM
```

```
Number of manoeuvres-526
```

```
dimensions-{3796, 13}
```

```
24.445 Second
```

```
Out[12]= 526
```

■ Generic Plot for Set of Data

```
In[13]:= ptPoly[pTop_, pBot_, x_, dx_] := Module[{npts, ptsTop, ptsBot},
  npts = Length[pTop];
  ptsTop = Table[{x + i dx, pTop[[i]]}, {i, npts}];
  ptsBot = Table[{x + i dx, pBot[[i]]}, {i, npts}];
  Join[ptsTop, Reverse[ptsBot]]
];
ptLine[pts_, x_, dx_] := Module[{npts},
  npts = Length[pts];
  Table[{x + i dx, pts[[i]]}, {i, npts}]
]
```

```
In[15]:= {
  maxVibCol, percVibCol, avgVibCol, percDirCol, maxStdCol, avgStdCol
} = {
  Red, Yellow, Green, RoyalBlue, Black, White
};
```

17:27:54 Thursday, August 7, 2003

Figure C2: Mathematica code for stress plots, Page 2.

stabStrain2.nb

3

```

In[16]:= picManv[mtx_, x_, dx_] :=
(* Draws the statistical data for a manoeuvre *)
Module[{man, avgVib, maxVib, percVib, avgStd, minStd, maxStd,
  absMinStd, absMaxStd, percDirMax, percDirMin, flgtNum, runNum},
{man, avgVib, maxVib, percVib, avgStd, minStd, maxStd, absMinStd, absMaxStd,
  percDirMax, percDirMin, flgtNum, runNum} = Transpose[mtx] / 1000.;
If[Length[mtx] == 1,
{Thickness[0.001], PointSize[0.002],
maxVibCol, Line[ptPoly[maxStd+maxVib, minStd-maxVib, x, dx]],
percVibCol, Line[ptPoly[maxStd+percVib, minStd-percVib, x, dx]],
avgVibCol, Line[ptPoly[maxStd+avgVib, minStd-avgVib, x, dx]],
Dashing[{(*0.05,0.01*)}], percDirCol,
Line[ptPoly[percDirMax, percDirMin, x, dx]],
Dashing[{(*0.003,0.0075*)}], maxStdCol,
Point[ptLine[maxStd, x, dx][[1]], Point[ptLine[minStd, x, dx][[1]],
Dashing[{}], avgStdCol, Point[ptLine[avgStd, x, dx][[1]]]
},
{Thickness[0.001],
maxVibCol, Polygon[ptPoly[maxStd+maxVib, minStd-maxVib, x, dx]],
percVibCol, Polygon[ptPoly[maxStd+percVib, minStd-percVib, x, dx]],
avgVibCol, Polygon[ptPoly[maxStd+avgVib, minStd-avgVib, x, dx]],
Dashing[{(*0.05,0.01*)}], percDirCol,
Polygon[ptPoly[percDirMax, percDirMin, x, dx]],
(*Line[ptLine[percDirMax,x,dx]],Line[ptLine[percDirMin,x,dx]],*)
Dashing[{(*0.003,0.0075*)}], maxStdCol,
Line[ptLine[maxStd, x, dx]], Line[ptLine[minStd, x, dx]],
Dashing[{}], avgStdCol, Line[ptLine[avgStd, x, dx]]
}}
]

```

17:27:54 Thursday, August 7, 2003

Figure C3: Mathematica code for stress plots, Page 3.

stabStrain2.nb

4

■ Legend for Plots

```

In[17]:= legnd = Module[{avgVib, maxVib, percVib, avgStd, minStd, maxStd, absMinStd,
  absMaxStd, percDirMax, percDirMin, x = 400, dx = 5, vec, p1, p2},
  vec = {6663.813`, 9568.719`, 8526.507`, -16644.44`, -18101.65`,
    -15120.44`, -26852.94`, -7042.328`, -11593.64`, -21639.94`};
  {1800, 4000, 3000, 8000, 6000, 9400, 3400, 11400, 10000, 4700};
  {avgVib, maxVib, percVib, avgStd, minStd, maxStd, absMinStd,
    absMaxStd, percDirMax, percDirMin} = Transpose[{vec, vec}];
  p2 = Show[Graphics[{
    Text["maxVibMax", {x + 2 dx, (maxStd + maxVib)[[1]], {-1, 0}},
    Text["percVibMax", {x + 2 dx, (maxStd + percVib)[[1]], {-1, 0}},
    Text["avgVibMax", {x + 2 dx, (maxStd + avgVib)[[1]], {-1, 0}},
    Text["percDirMax", {x + 2 dx, percDirMax[[1]], {-1, 0}},
    Text["maxStd", {x + 2 dx, maxStd[[1]], {-1, 0}},
    Text["avgStd", {x + 2 dx, avgStd[[1]], {-1, 0}},
    Text["minStd", {x + 2 dx, minStd[[1]], {-1, 0}},
    Text["percDirMin", {x + 2 dx, percDirMin[[1]], {-1, 0}},
    Text["avgVibMin", {x + 2 dx, (minStd - avgVib)[[1]], {-1, 0}},
    Text["percVibMin", {x + 2 dx, (minStd - percVib)[[1]], {-1, 0}},
    Text["maxVibMin", {x + 2 dx, (minStd - maxVib)[[1]], {-1, 0}},
    Thickness[0.001],
    maxVibCol, Polygon[ptPoly[maxStd + maxVib, minStd - maxVib, x, dx]],
    percVibCol, Polygon[ptPoly[maxStd + percVib, minStd - percVib, x, dx]],
    avgVibCol, Polygon[ptPoly[maxStd + avgVib, minStd - avgVib, x, dx]],
    Dashing[{(0.05, 0.01*)}], percDirCol,
      Polygon[ptPoly[percDirMax, percDirMin, x, dx]],
    Dashing[{(0.003, 0.0075*)}], maxStdCol,
      Line[ptLine[maxStd, x, dx]], Line[ptLine[minStd, x, dx]],
    Dashing[{}], avgStdCol, Line[ptLine[avgStd, x, dx]]
  }], DisplayFunction -> Identity];
Print["time history=",
  Dimensions[datTimHist = ReadList["stbnbmlrTimeHistoryT24R082.dat"]]];
(* Choosing the first 400 pts to show trend only *)
p1 =
  ListPlot[Take[datTimHist, 400], PlotJoined -> True, DisplayFunction -> Identity];
Show[{p1, p2}, Frame -> True, FrameLabel -> {"time", "BndStrnPSI", "", ""},
  DisplayFunction -> $DisplayFunction,
  PlotRange -> All, Axes -> False, FrameTicks -> None]
]

time history: {12907}

```

17:27:54 Thursday, August 7, 2003

Figure C4: Mathematica code for stress plots, Page 4.

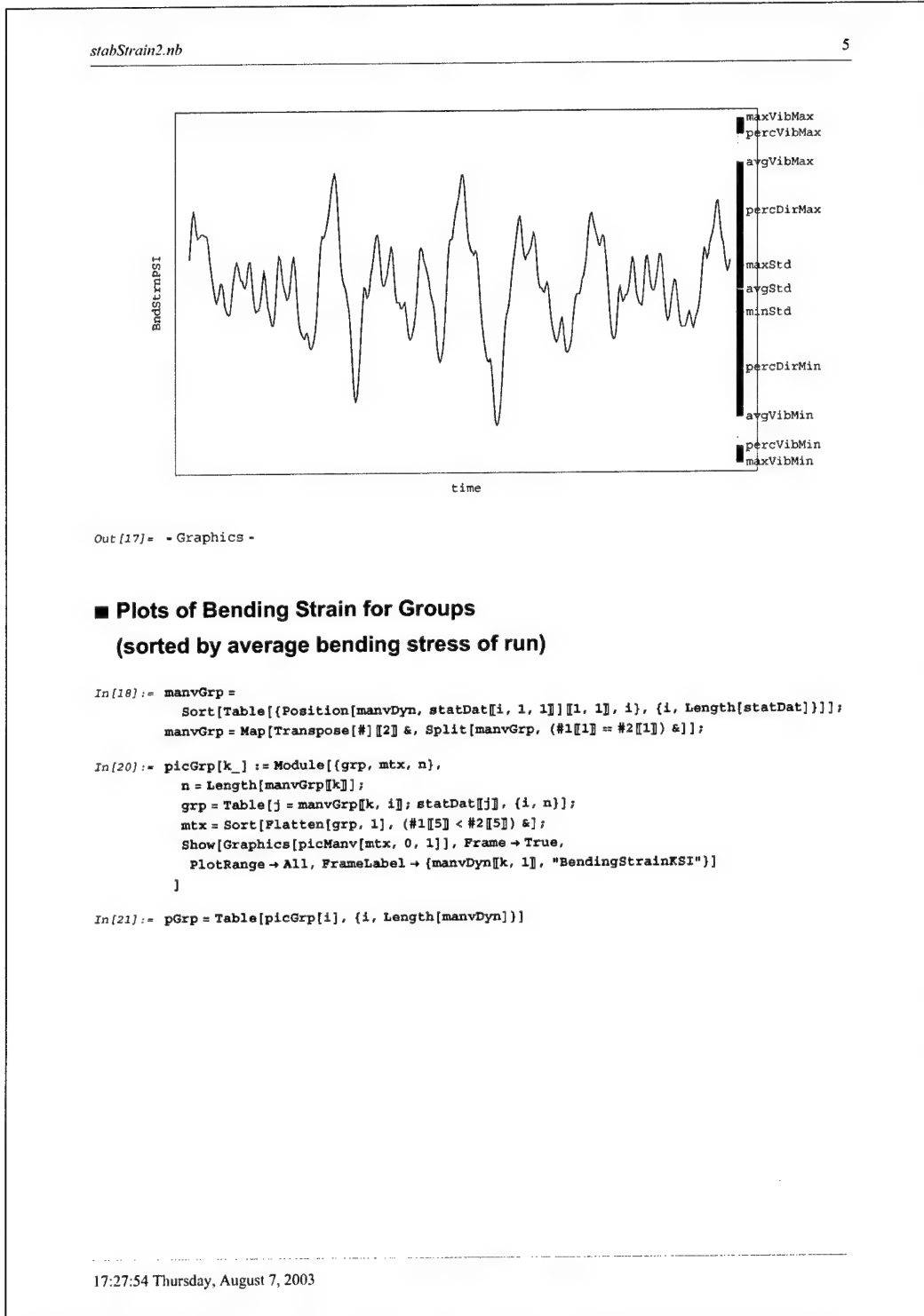


Figure C5: Mathematica code for stress plots, Page 5.

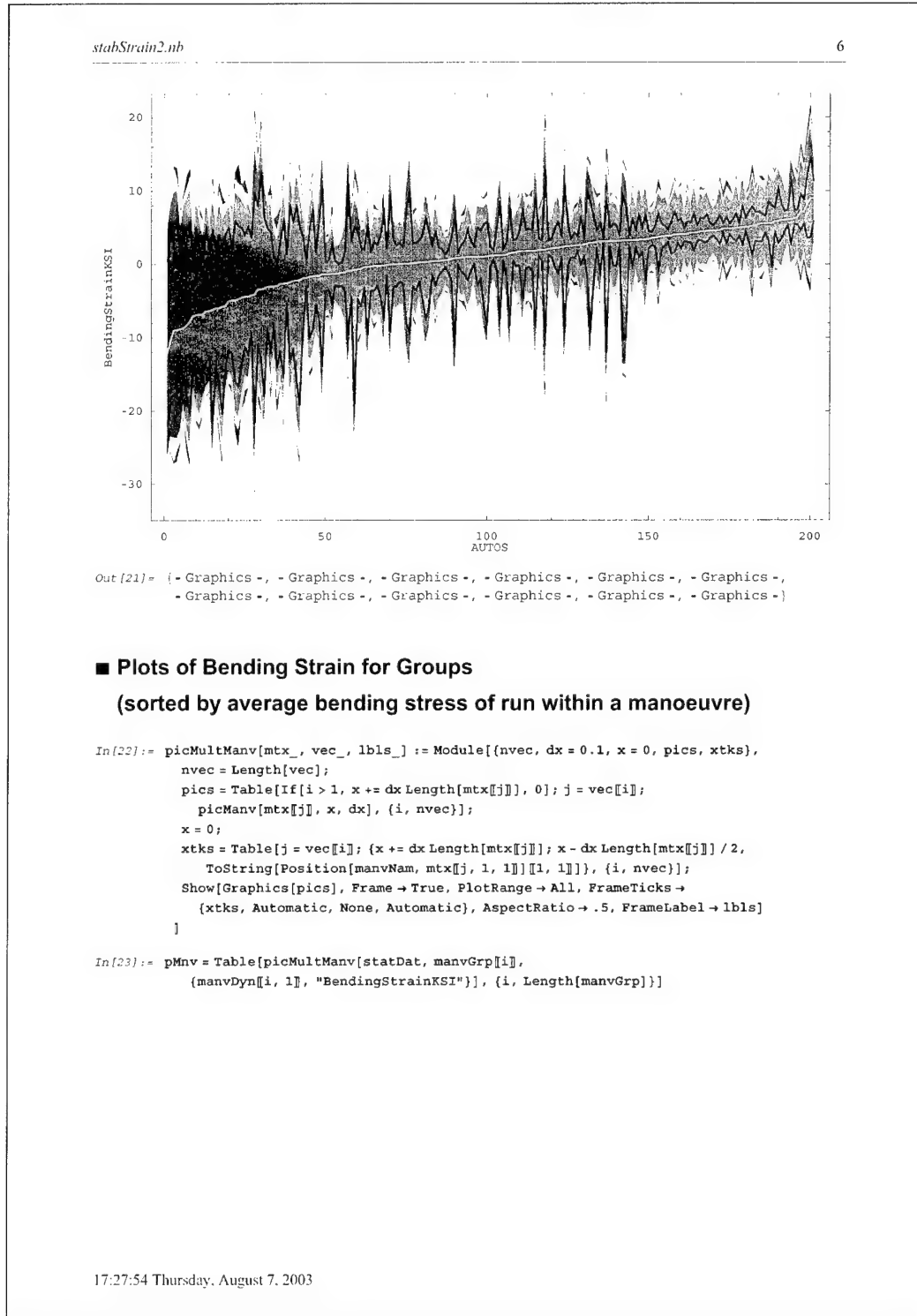


Figure C6: Mathematica code for stress plots, Page 6.

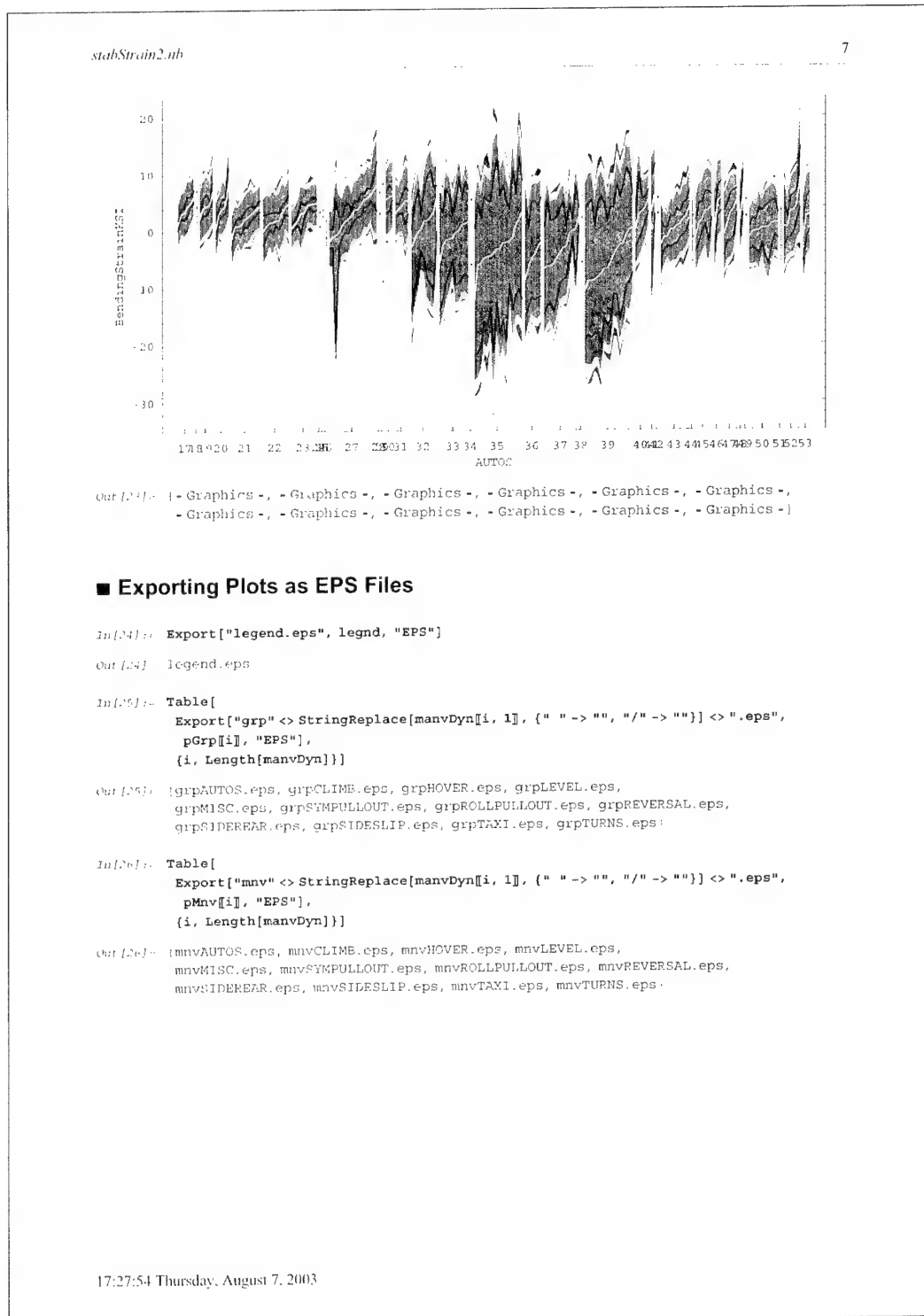


Figure C7: Mathematica code for stress plots, Page 7.

Appendix D Bending Stress from Flight Loads Survey

This Appendix contains plots of the stabilator bending strain at a location that is 9.2" from the root. These "statistical summaries" of stress were obtained from the Flight Loads Survey of the Black Hawk [8]. By statistical summaries we mean, for example, the average steady, maximum vibratory, and 95% percentile stress. For a legend to these plots and further details of these statistical summaries see Section 5.3, which begins on page 32. In particular, for an illustration of the legend see Figure 5.2.

Most of the 526 manoeuvres contain multiple runs, but a few manoeuvres contain only one run. There were some missing data in these statistical summaries, in particular, of the 3796 runs there were 31 runs that were missing all the statistical data except for the 95% and 5% percentile of the direct stress measurement. The list of manoeuvres with incomplete data is shown in Table D1. Note that the stresses in this table are given in *psi* (and have been rounded to three significant figures), whereas the stresses in all the plots within this appendix are given in *ksi*.

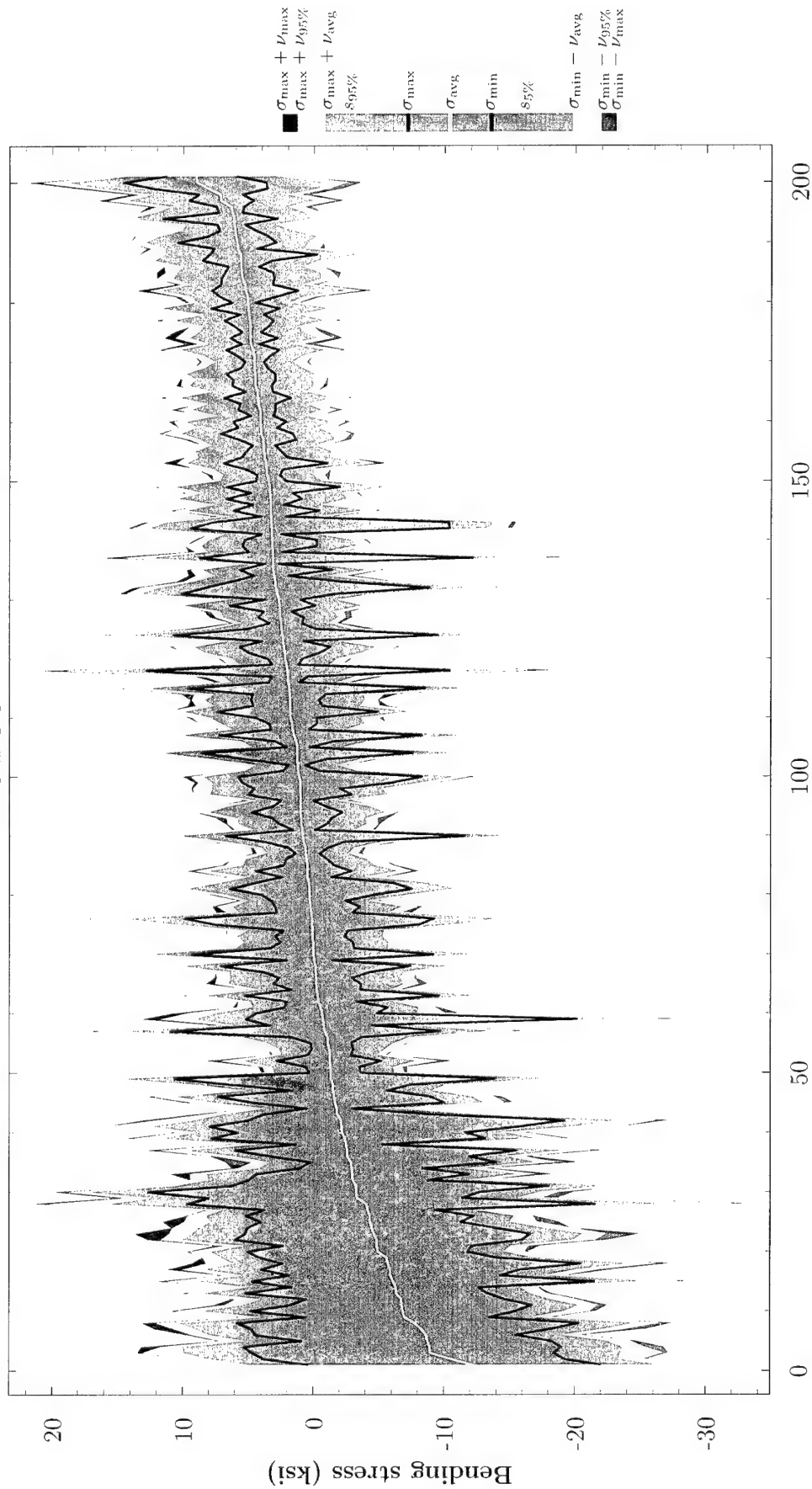
The first twelve plots in this appendix, Figures D1–D12, show the bending stresses sorted by the average steady stress for each run of the Flight Loads Survey. All manoeuvres were partitioned into one of twelve groups. The horizontal axis in these plots enumerates each run within a particular group, which gives us an idea of the number of runs within a group.

The next twelve plots, Figures D13–D24, show the bending stresses partitioned into manoeuvres, and then sorted by the average steady stress for each run within a manoeuvre. In these plots, the tick marks on the *x*-axis denote the manoeuvre. Each of these tick marks has been labelled with the manoeuvre name in a very small font (which was necessary to avoid overlap of the manoeuvre names). These manoeuvre names will be illegible when the plots are printed on a standard A4 page. However, these names are legible when the electronic version of this report is viewed in a zoomed mode.

Table D1: *List of the 31 runs that were deleted in the plots contained in this appendix. These runs were deleted because they were missing statistical data for the steady and vibratory components of the run. Only the 5% and 95% percentile direct stress measurements ($s_{5\%}$ and $s_{95\%}$, respectively) were available for these manoeuvres.*

<i>Flight</i>	<i>Run</i>	<i>Manoeuvre</i>	$s_{5\%}$ (psi)	$s_{95\%}$ (psi)
22	4	ambient	178	354
24	8	ambient	940	1230
25	4	ambient	1050	1240
26	4	ambient	-2.44	286
28	4	ambient	-554	-295
29	4	ambient	568	857
30	4	ambient	1010	1270
32	4	ambient	277	445
34	4	ambient	-290	-97
36	4	ambient	-77.8	211
37	4	ambient	-508	-316
39	4	ambient	-304	853
40	4	ambient	456	840
41	4	ambient	1160	1350
42	4	ambient	207	378
43	6	ambient	325	517
44	4	ambient	536	708
45	4	ambient	24.3	313
46	4	ambient	-453	-164
48	4	ambient	961	1150
48	16	air taxi fwd, ige, 10kts	-3460	845
48	18	air taxi fwd, ige, 20kts	-3320	967
48	19	air taxi accel, 30kts	-3420	767
49	4	ambient	766	958
50	4	ambient	182	471
52	4	ambient	474	666
52	33	roll po rt, .8vh, 1.5g	-2330	7430
52	34	roll po rt, .8vh, 1.5g	-1410	6870
52	35	roll po rt, .8vh, 1.5g	-3080	7180
52	36	roll po rt, .8vh, 1.5g	-3770	9080
53	4	ambient	59.0	237

AUTOS



Enumeration of runs

Figure D1: Plot of stabilator spar bending stress for the manoeuvre group of *autos*. These stresses were sorted by the average steady stress for each run. These strain measurement were taken at the zeroth gauge, which is located 9.2" from the stabilator root.

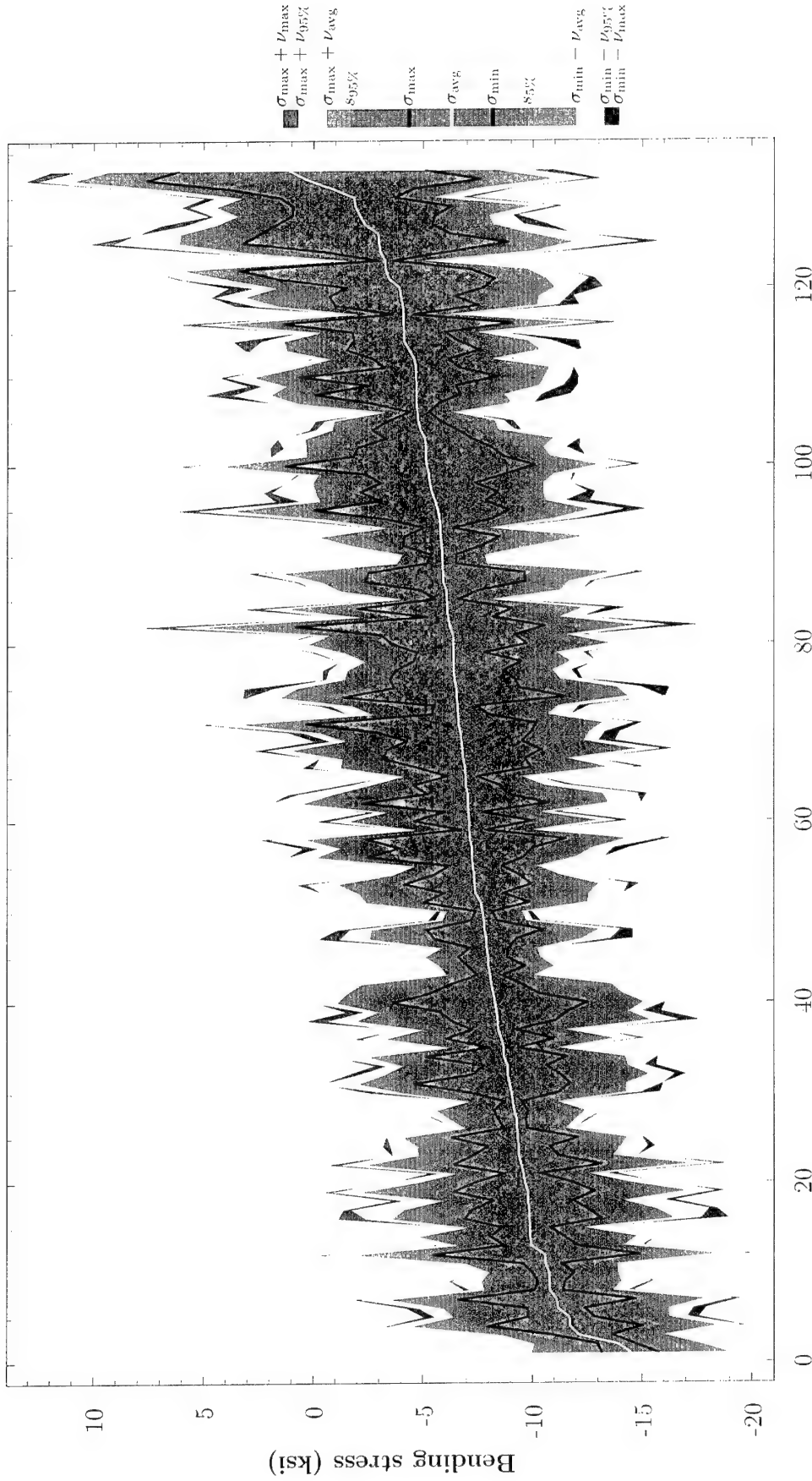
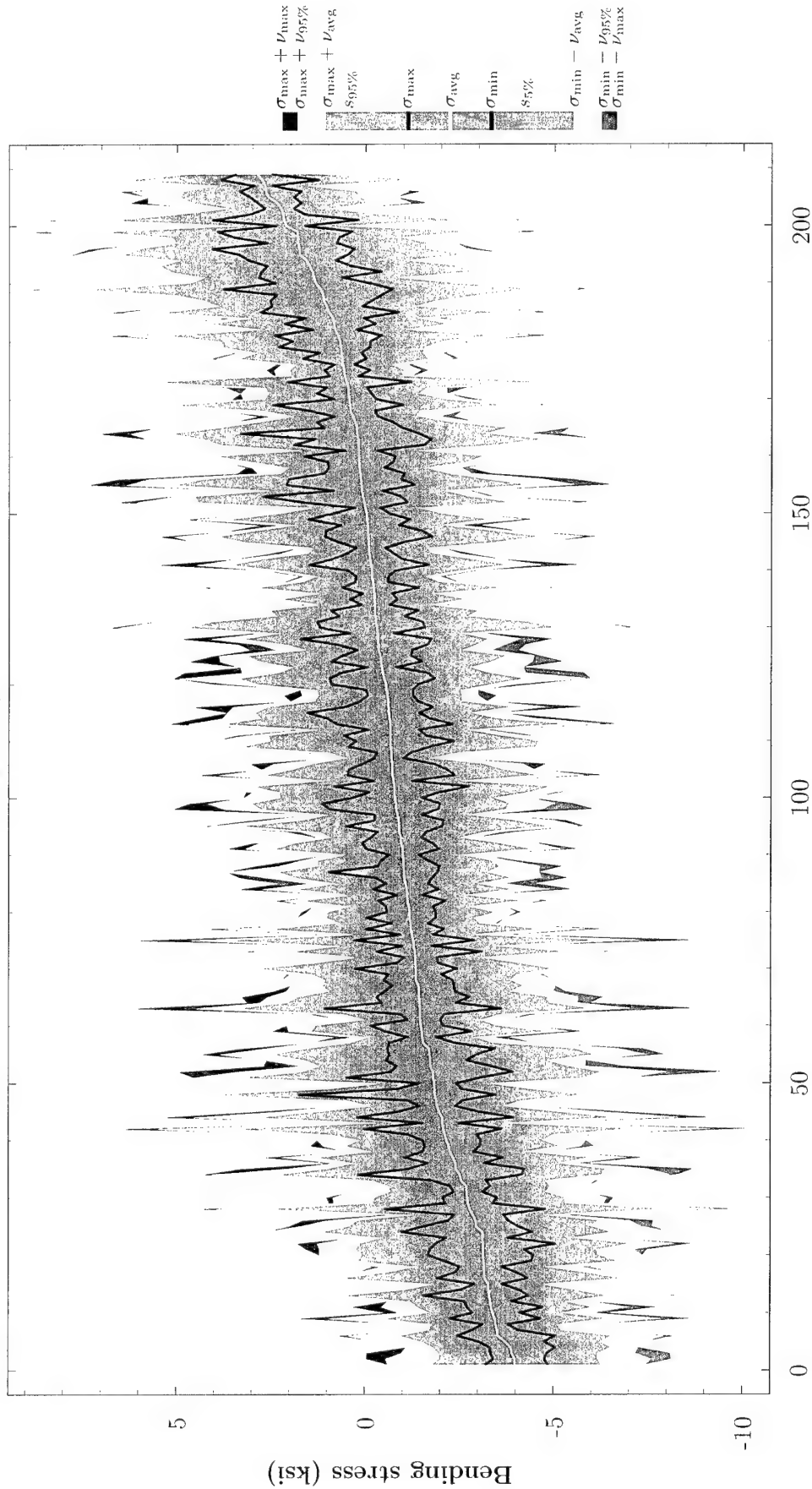


Figure D2: Plot of stabilator spar bending stress for the manoeuvre group of *climb*. These stresses were sorted by the average steady stress for each run. These strain measurement were taken at the zeroth gauge, which is located 9.2" from the stabilator root.

HOVER

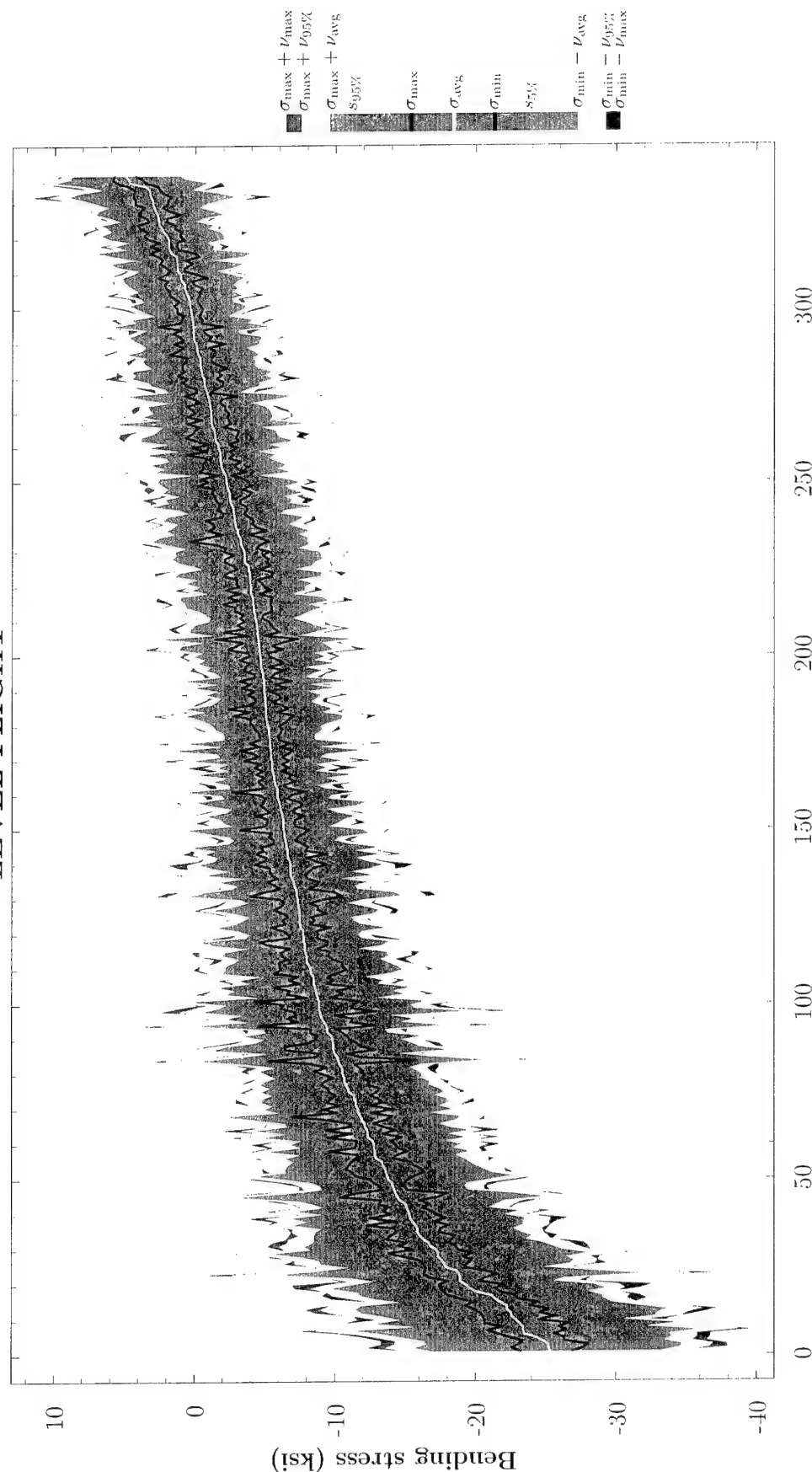


DSTO-TR-1590

Enumeration of runs

Figure D3: Plot of stabilator spar bending stress for the manoeuvre group of *hover*. These stresses were sorted by the average steady stress for each run. These strain measurement were taken at the zeroth gauge, which is located 9.2" from the stabilator root.

LEVEL FLIGHT



DSTO TR 1590

Figure D4: Plot of stabilator spar bending stress for the manoeuvre group of **level flight**. These stresses were sorted by the average steady stress for each run. These strain measurement were taken at the zeroth gauge, which is located 9.2" from the stabilator root.

MISCELLANEOUS

DSTO-TR-1590

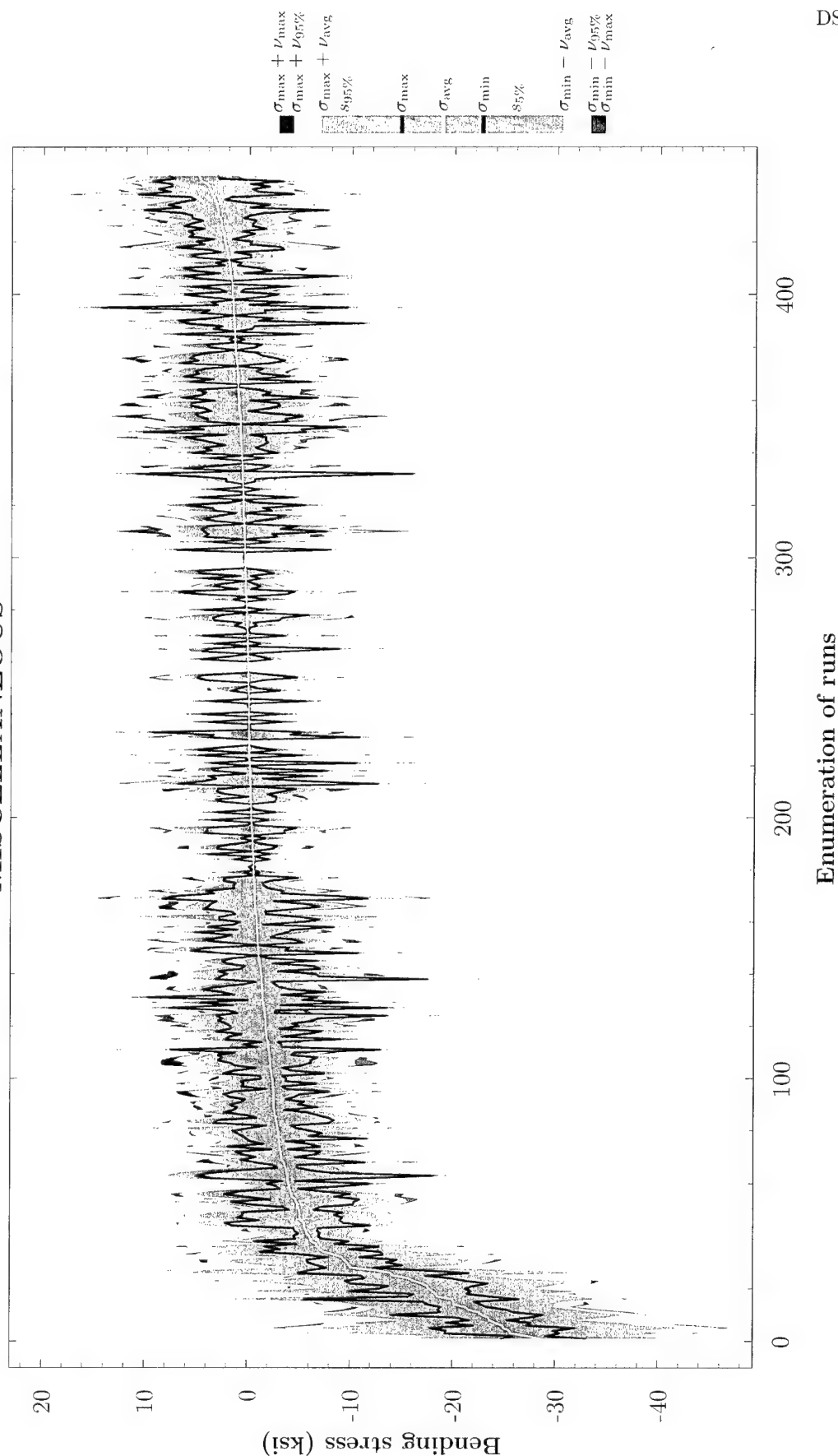


Figure D5: Plot of stabilator spar bending stress for the manoeuvre group of miscellaneous. These stresses were sorted by the average steady stress for each run. These strain measurement were taken at the zeroth gauge, which is located 9.2" from the stabilator root.

REVERSALS

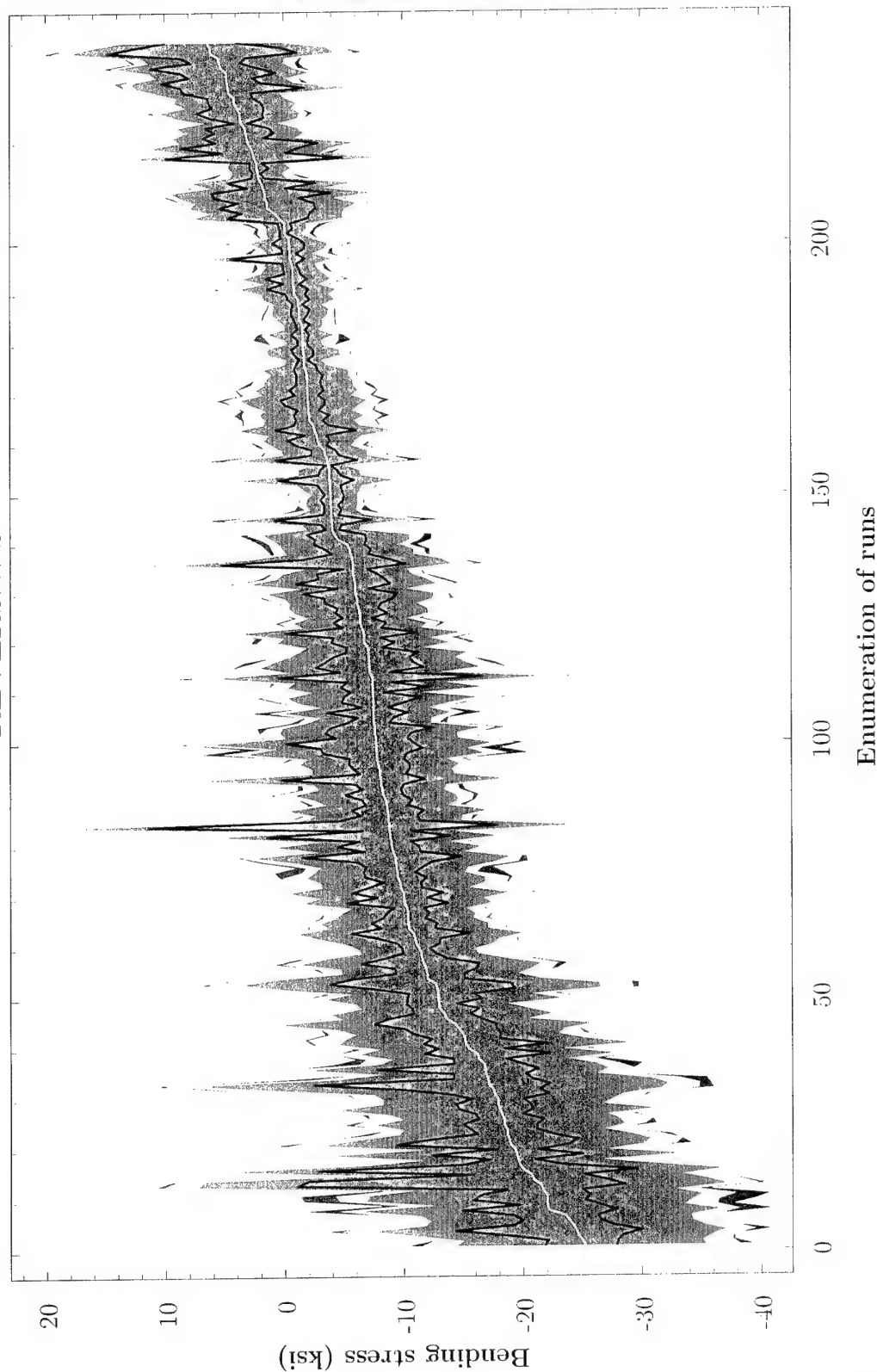
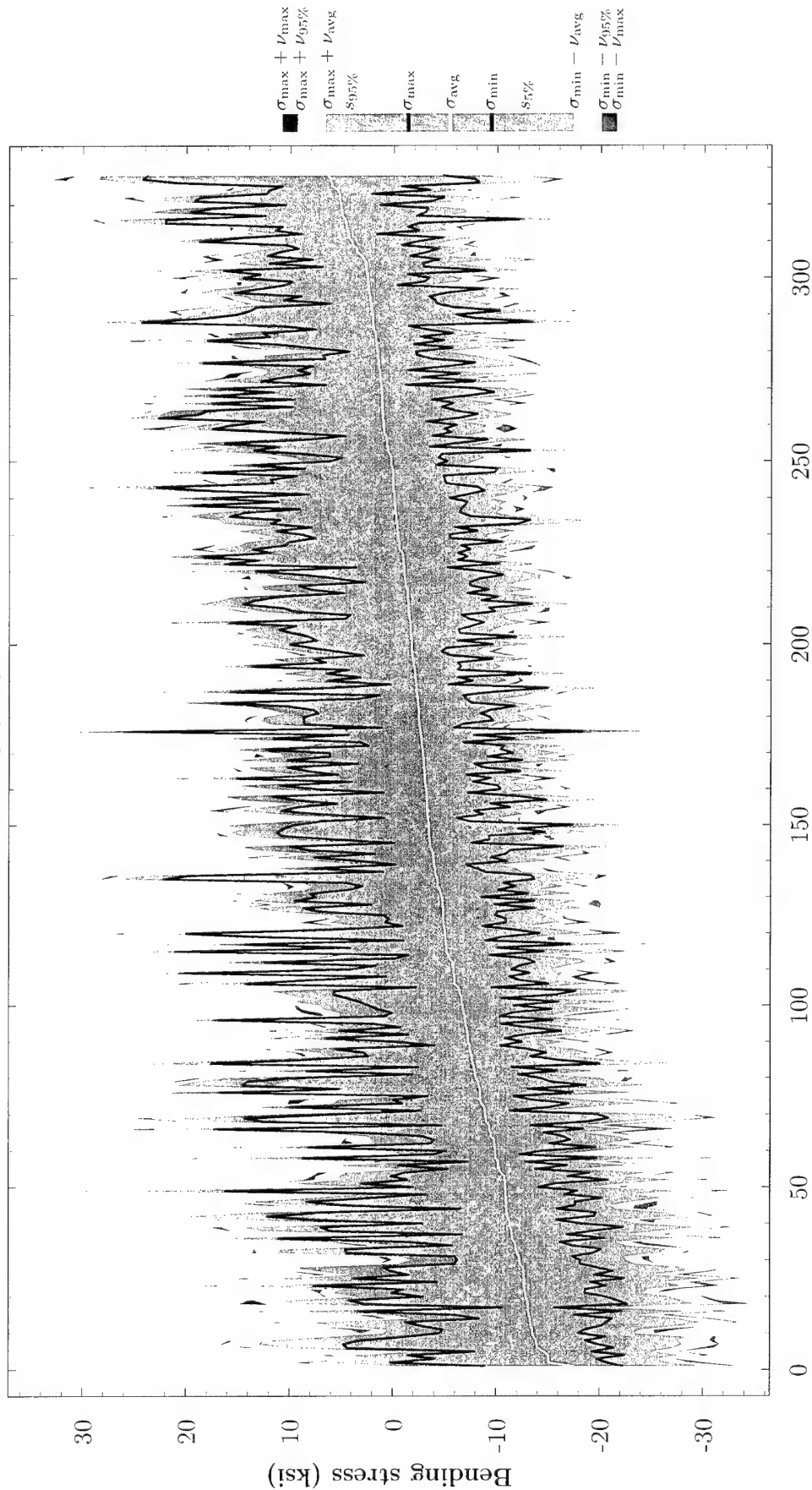


Figure D6: Plot of stabilator spar bending stress for the manoeuvre group of **reversals**. These stresses were sorted by the average steady stress for each run. These strain measurement were taken at the zeroth gauge, which is located 9.2" from the stabilator root.

PULLOUTS

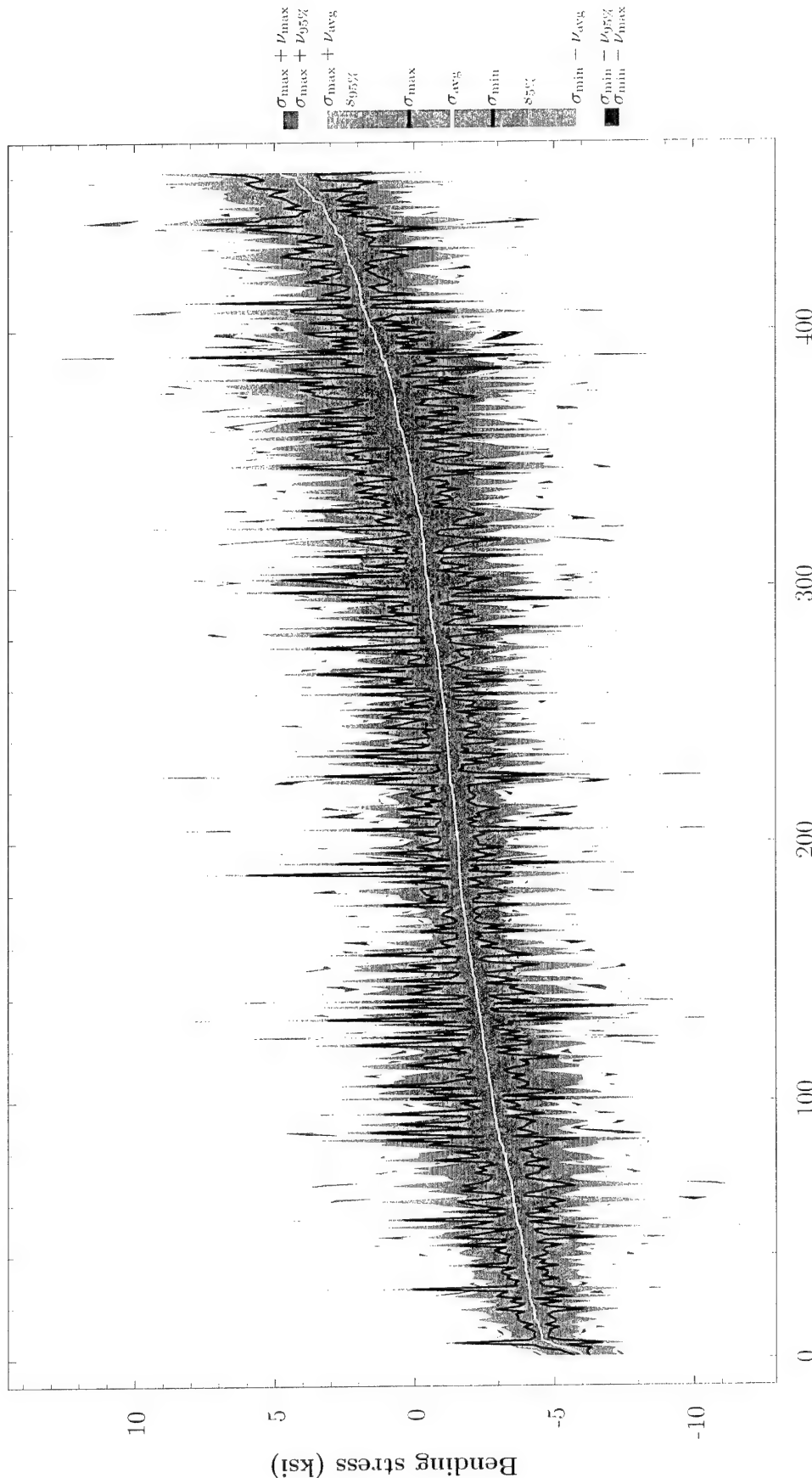


DSTO TR-1590

Enumeration of runs

Figure D7: Plot of stabilator spar bending stress for the manoeuvre group of **pullouts**. These stresses were sorted by the average steady stress for each run. These strain measurement were taken at the zeroth gauge, which is located 9.2" from the stabilator root.

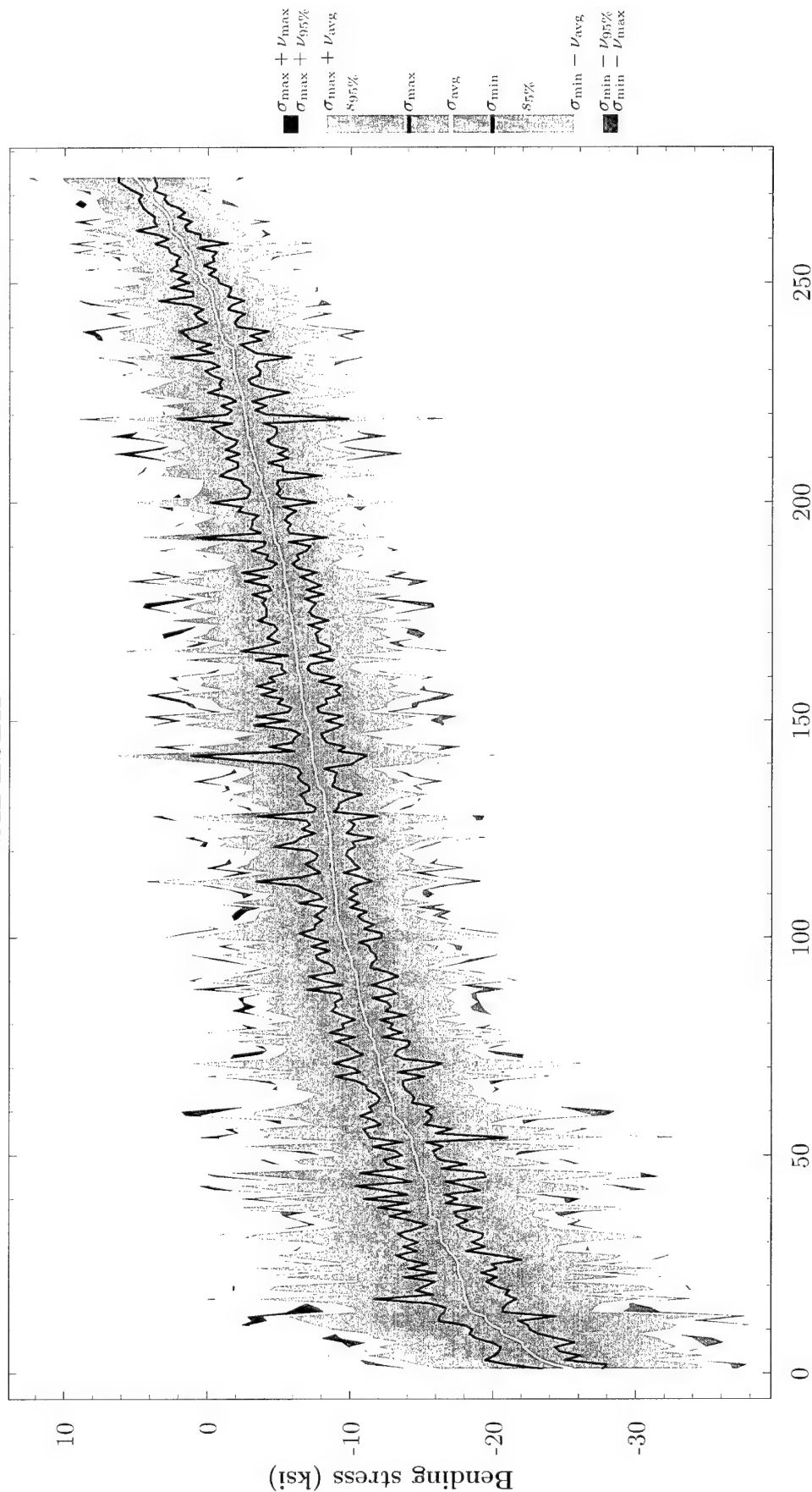
SIDE AND REAR FLIGHT



DSTO TR 1590

Figure D8: Plot of stabilator spar bending stress for the manoeuvre group of *side and rear flight*. These stresses were sorted by the average steady stress for each run. These strain measurement were taken at the zeroth gauge, which is located 9.2" from the stabilator root.

SIDESLIP

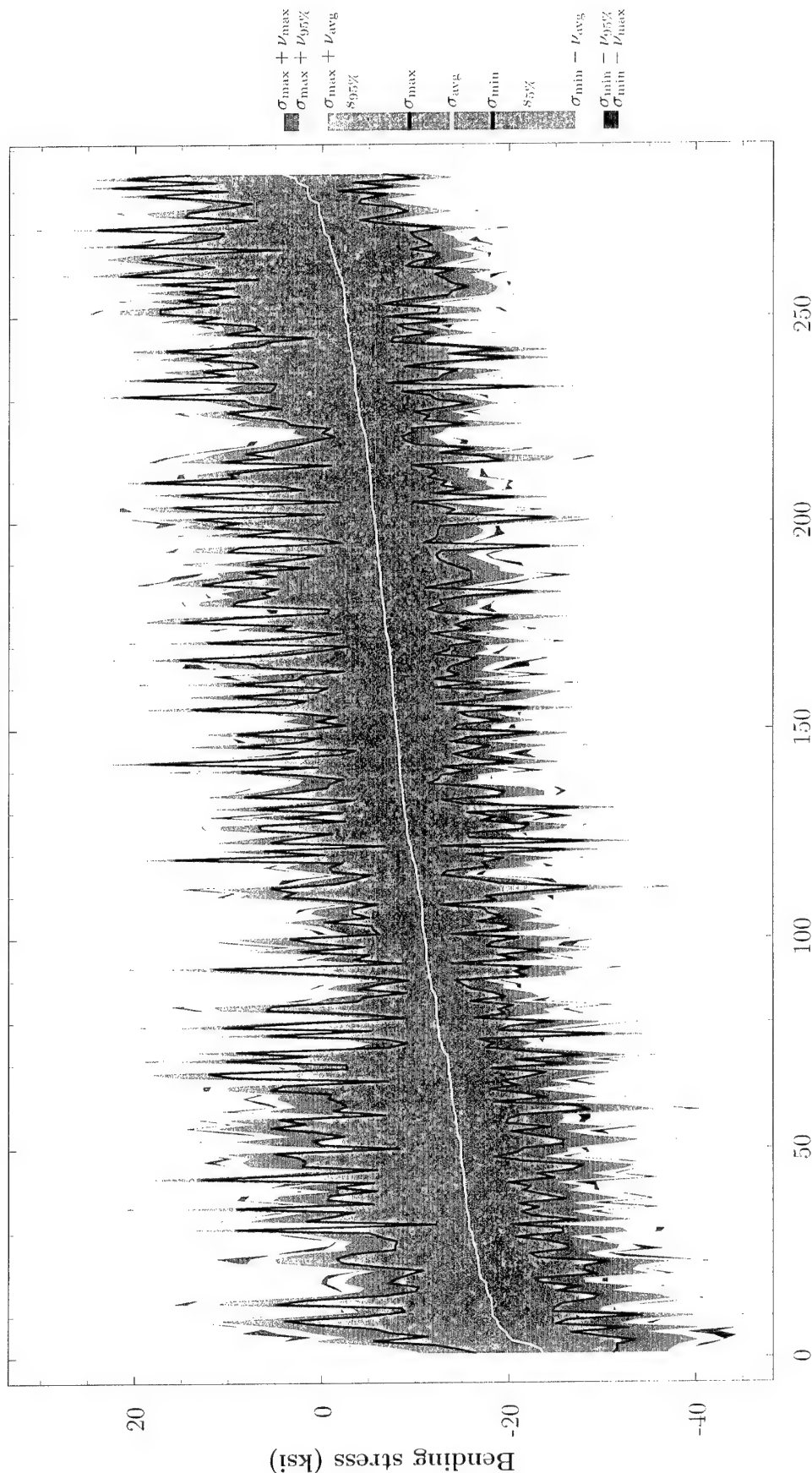


DSTO-TR-1590

Enumeration of runs

Figure D9: Plot of stabilator spar bending stress for the manoeuvre group of *sideslip*. These stresses were sorted by the average steady stress for each run. These strain measurement were taken at the zeroth gauge, which is located 9.2" from the stabilator root.

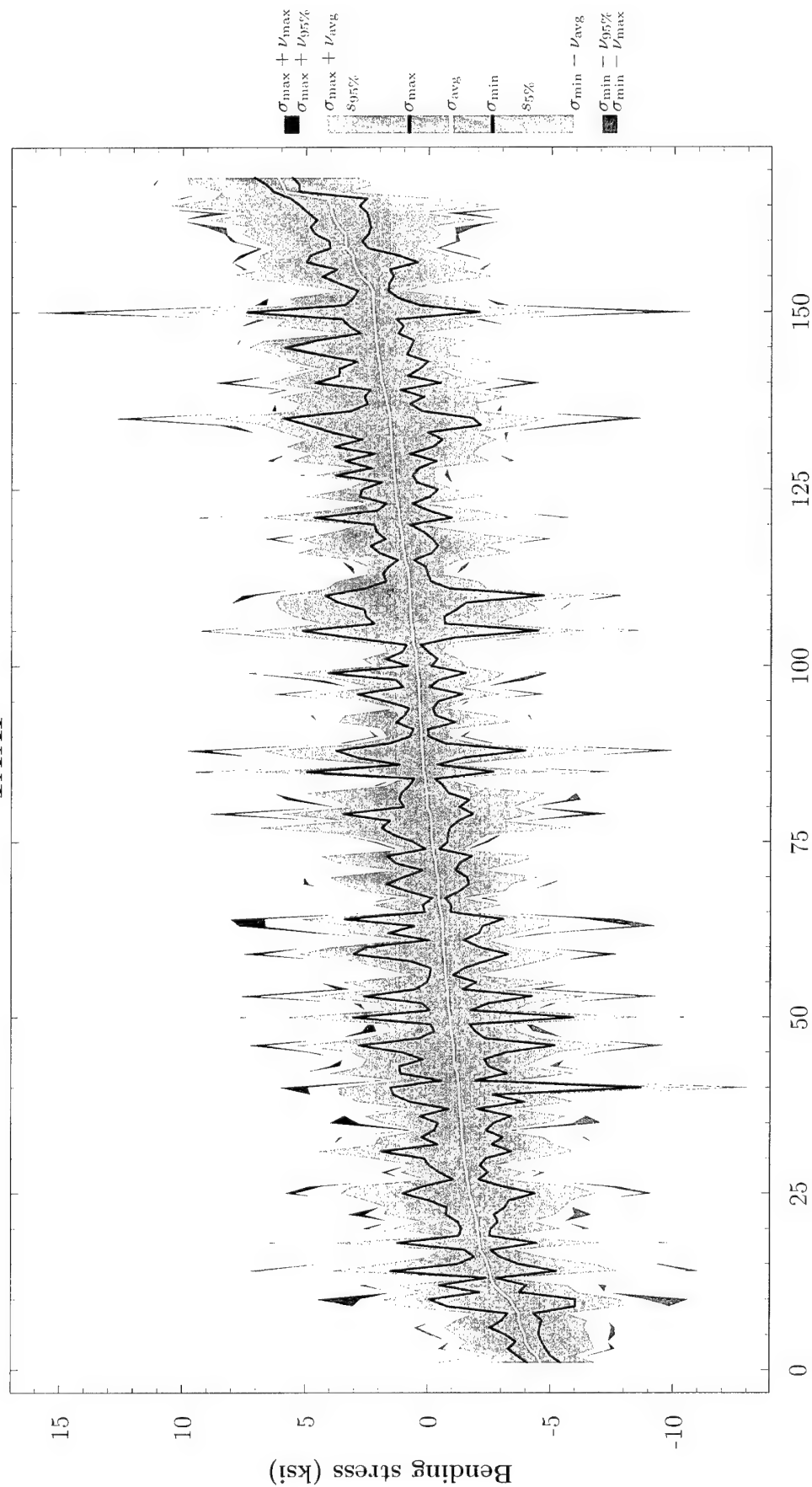
SYMMETRIC PULLOUTS



DSTO TR 1590

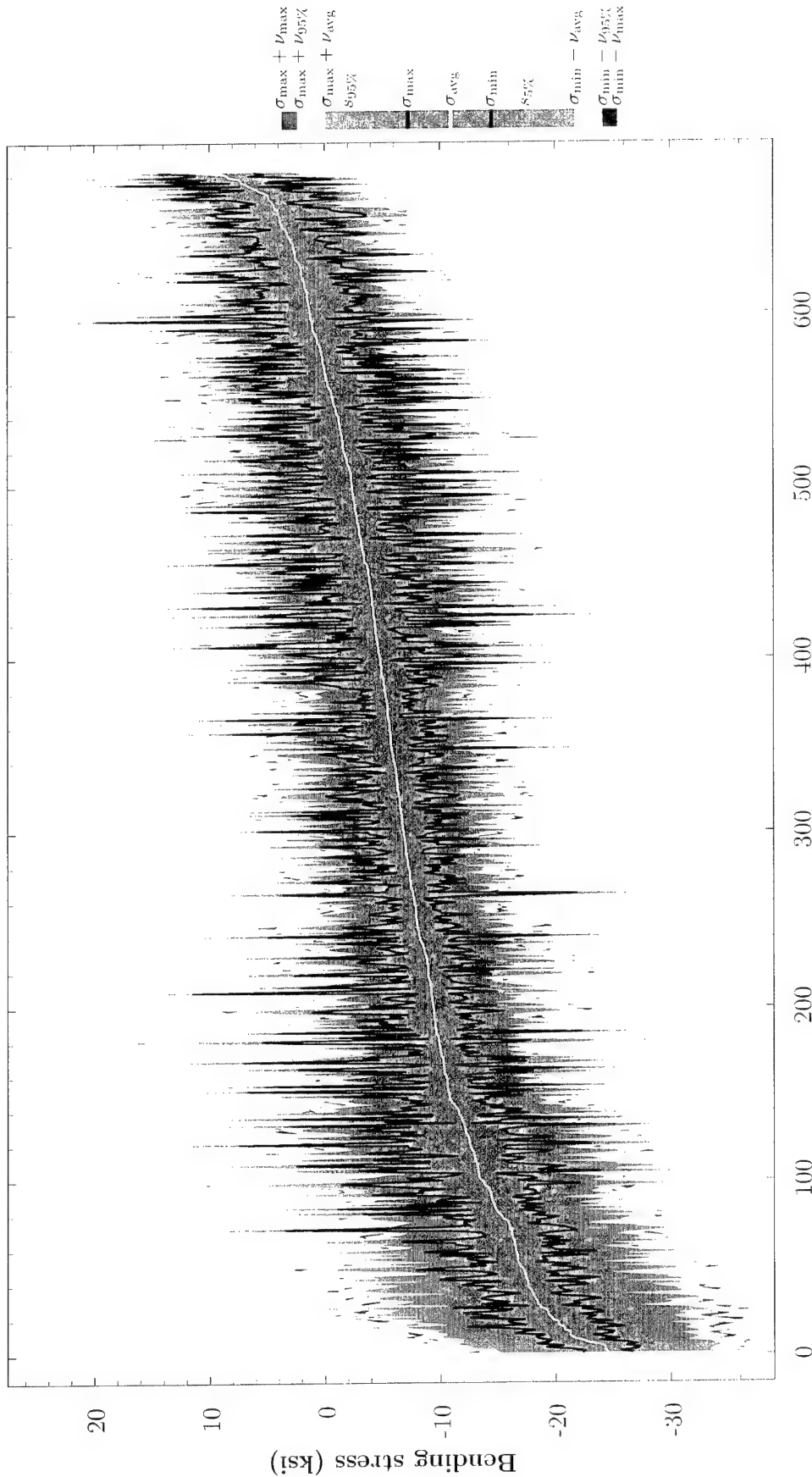
Enumeration of runs

Figure D10: Plot of stabilator spar bending stress for the manoeuvre group of **symmetric pullouts**. These stresses were sorted by the average steady stress for each run. These strain measurement were taken at the zeroth gauge, which is located 9.2" from the stabilator root.



Enumeration of runs

Figure D11: Plot of stabilator spar bending stress for the manoeuvre group of *taxi*. These stresses were sorted by the average steady stress for each run. These strain measurement were taken at the zeroth gauge, which is located 9.2" from the stabilator root.



Enumeration of runs

Figure D12: Plot of stabilator spar bending stress for the manoeuvre group of turns. These stresses were sorted by the average steady stress for each run. These strain measurement were taken at the zeroth gauge. which is located 9.2" from the stabilator root.

AUTOS

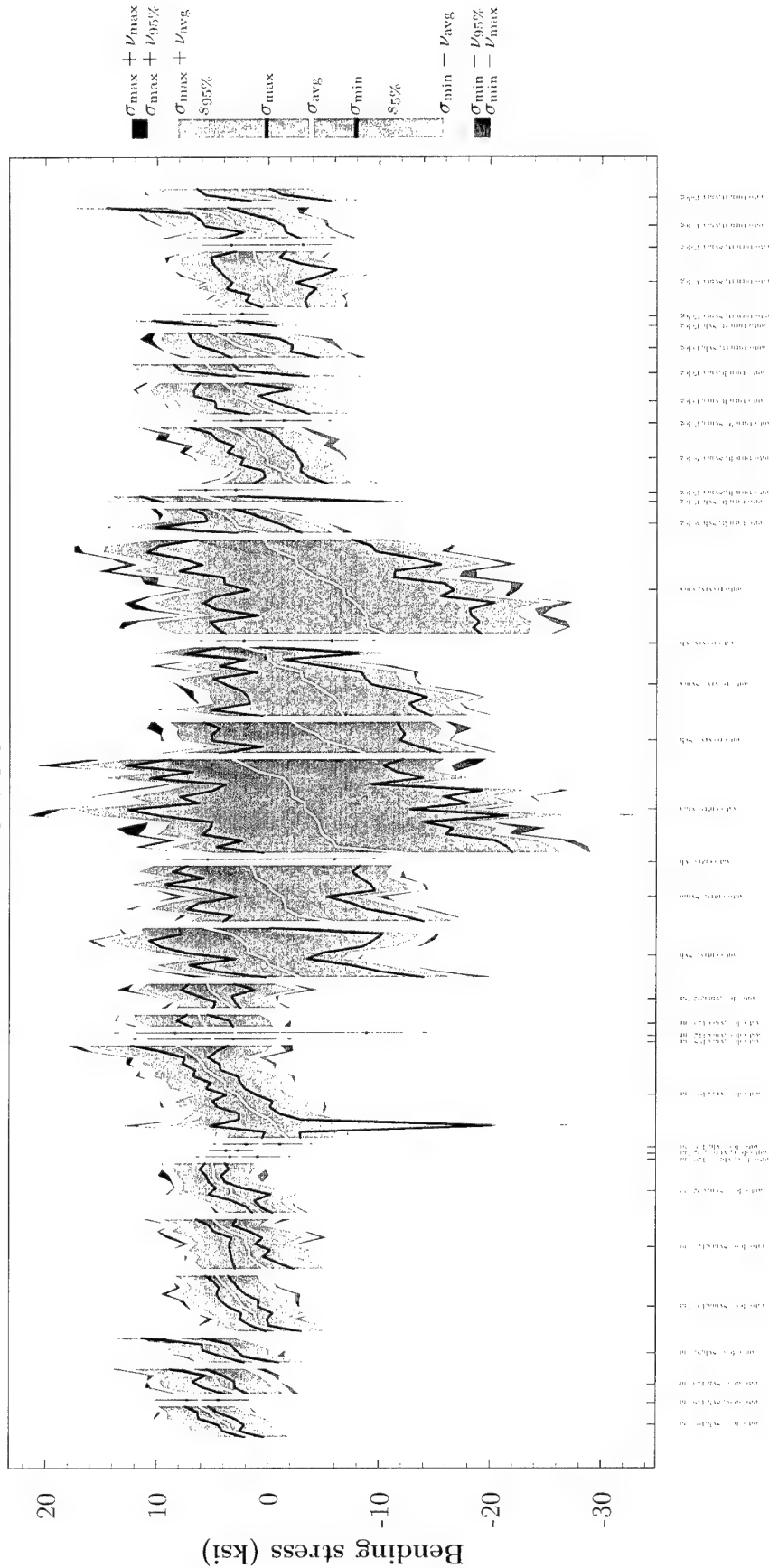


Figure D13: Plot of stabilator spar bending stress for the manoeuvres group of autos. These stresses were partitioned into manoeuvres, and then sorted by the average steady stress for each run within that manoeuvre. These strain measurement were taken at the zeroth gauge, which is located 9.2" from the stabilator root.

CLIMB

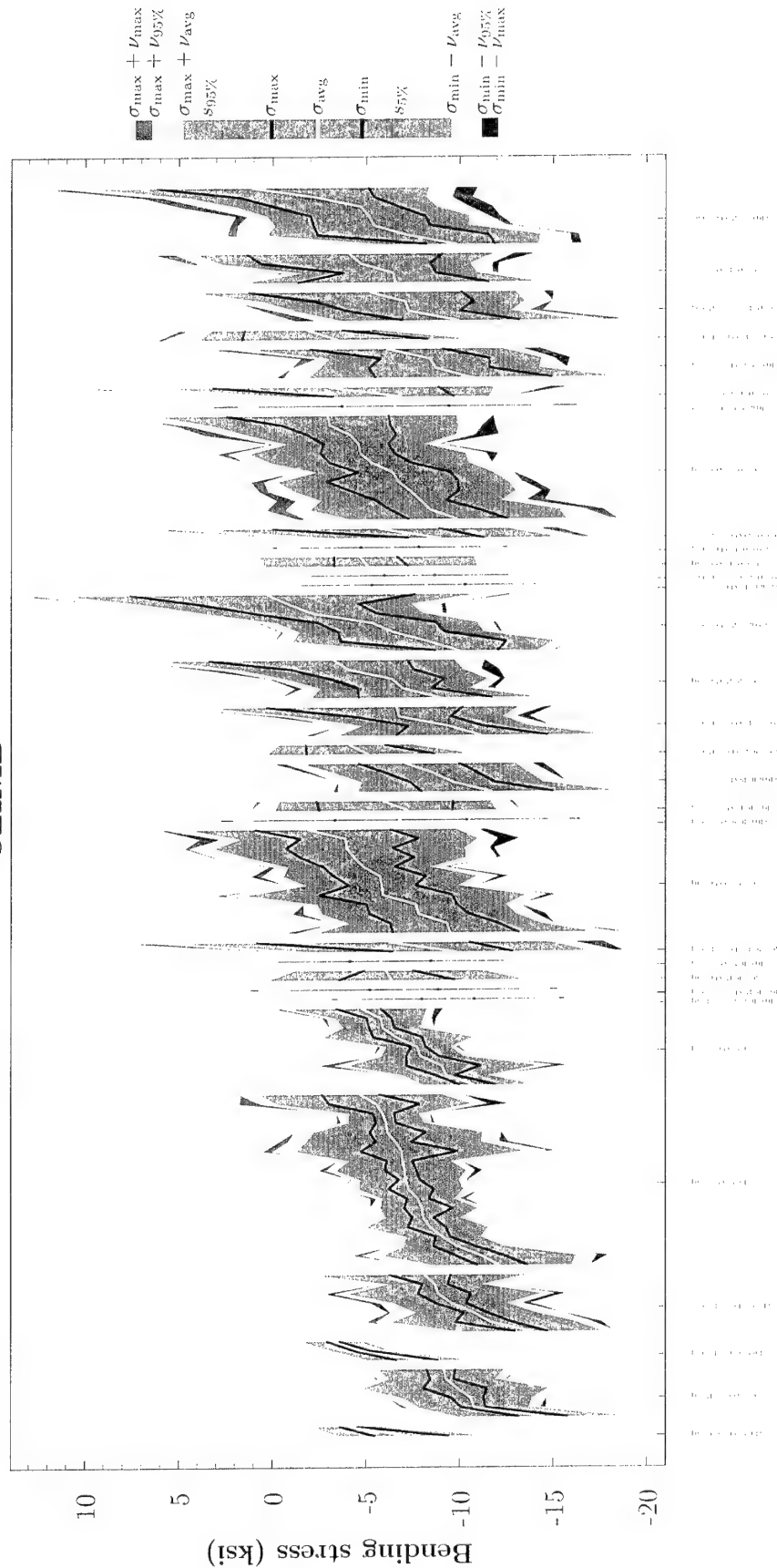


Figure D14: Plot of stabilator spar bending stress for the manoeuvres group of *climb*. These stresses were partitioned into manoeuvres, and then sorted by the average steady stress for each run within that manoeuvre. These strain measurement were taken at the zeroth gauge, which is located 9.2" from the stabilator root.

HOVER



Figure D15: Plot of stabilator spar bending stress for the manoeuvres group of *hover*. These stresses were partitioned into manoeuvres, and then sorted by the average steady stress for each run within that manoeuvre. These strain measurements were taken at the zeroth gauge, which is located 9.2" from the stabilator root.

LEVEL FLIGHT

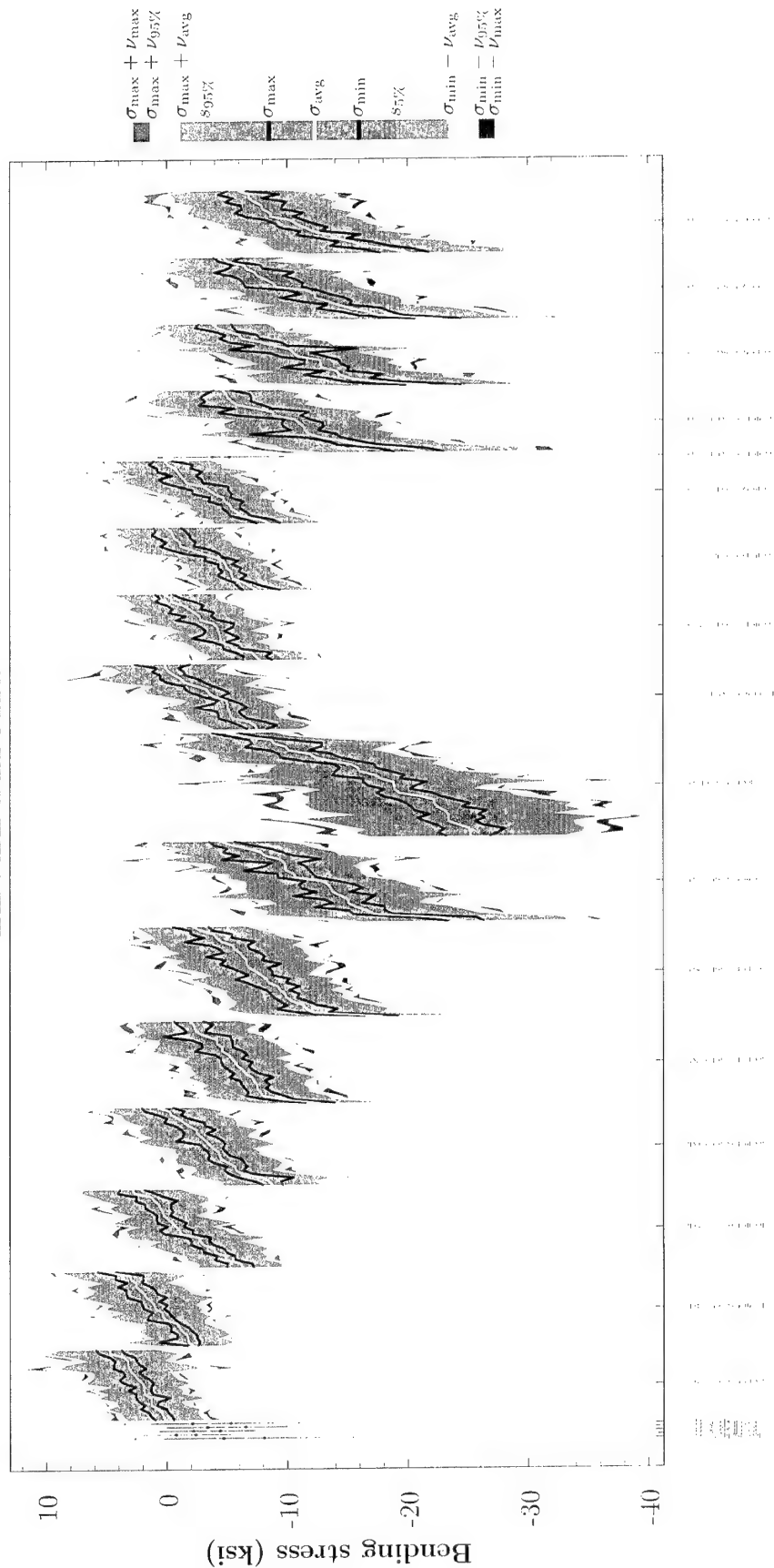


Figure D16: Plot of stabilator spar bending stress for the manoeuvres group of **level flight**. These stresses were partitioned into manoeuvres, and then sorted by the average steady stress for each run within that manoeuvre. These strain measurement were taken at the zeroth gauge, which is located 9.2" from the stabilator root.

MISCELLANEOUS

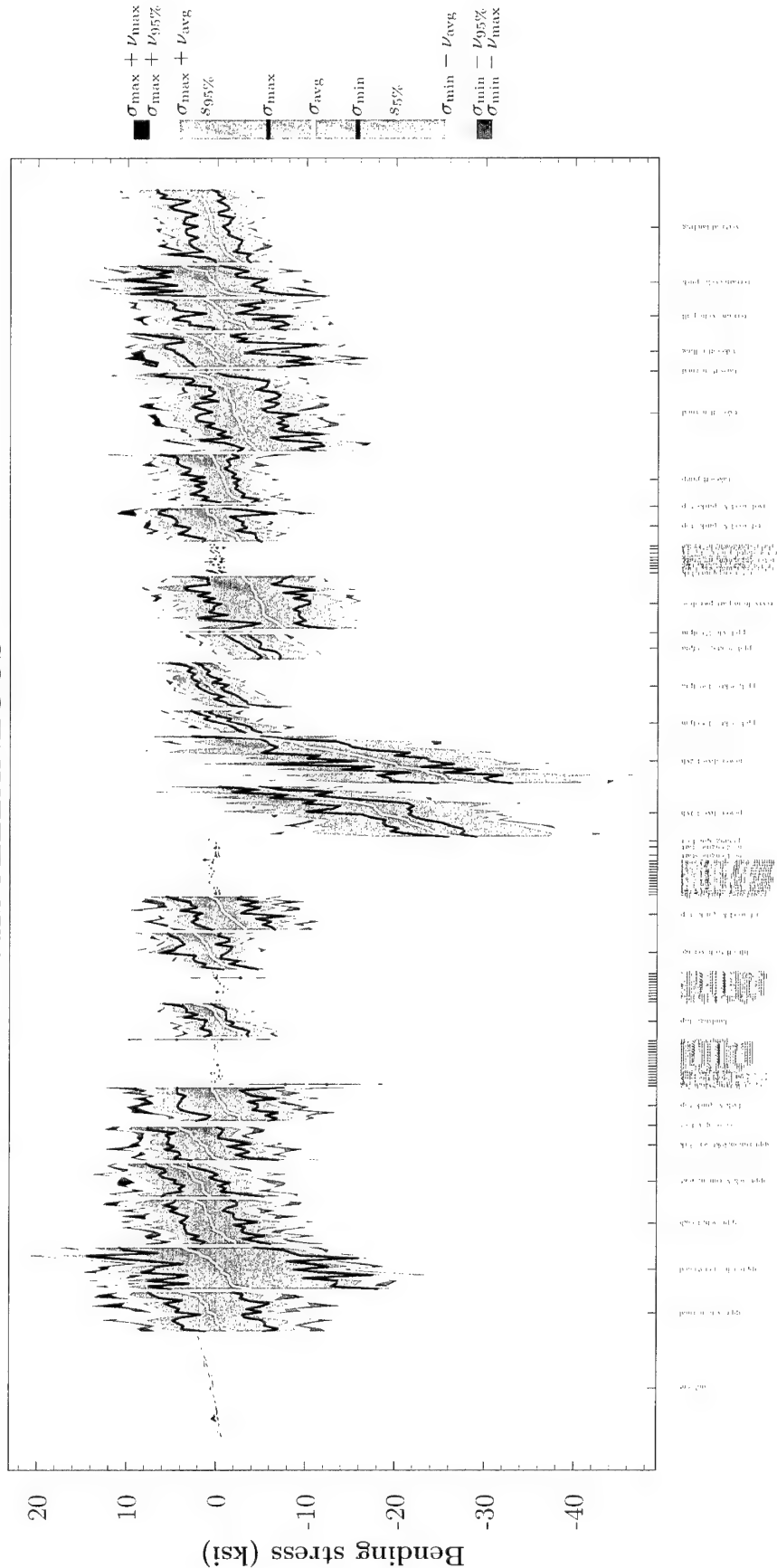


Figure D17: Plot of stabilator spar bending stress for the manoeuvres of miscellaneous. These stresses were partitioned into manoeuvres, and then sorted by the average steady stress for each run within that manoeuvre. These strain measurement were taken at the zeroth gauge, which is located 9.2" from the stabilator root.

REVERSALS

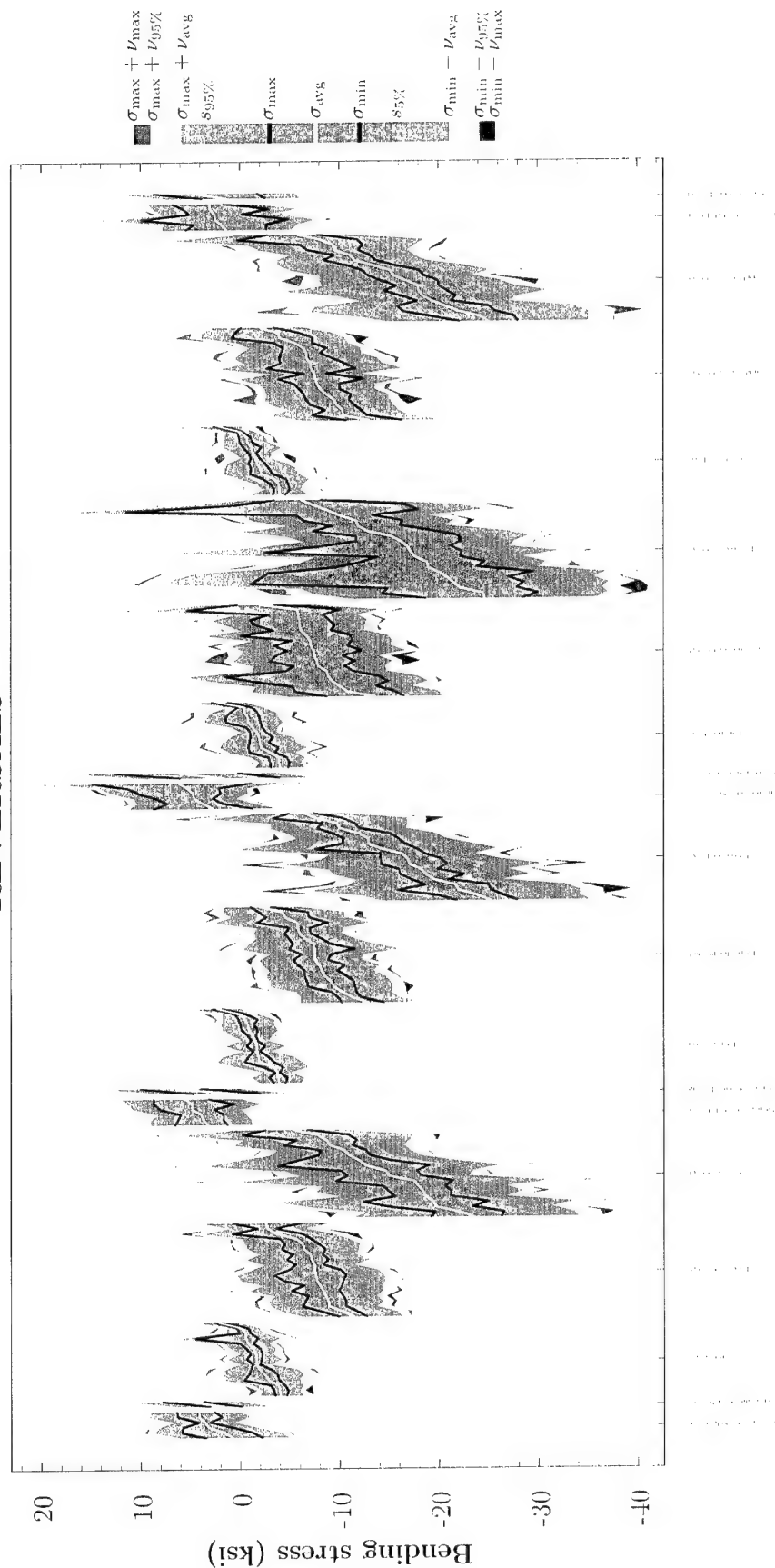


Figure D18: Plot of stabilator spar bending stress for the manoeuvres group of **reversals**. These stresses were partitioned into manoeuvres, and then sorted by the average steady stress for each run within that manoeuvre. These strain measurement were taken at the zeroth gauge, which is located 9.2" from the stabilator root.

ROLLING PULLOUT

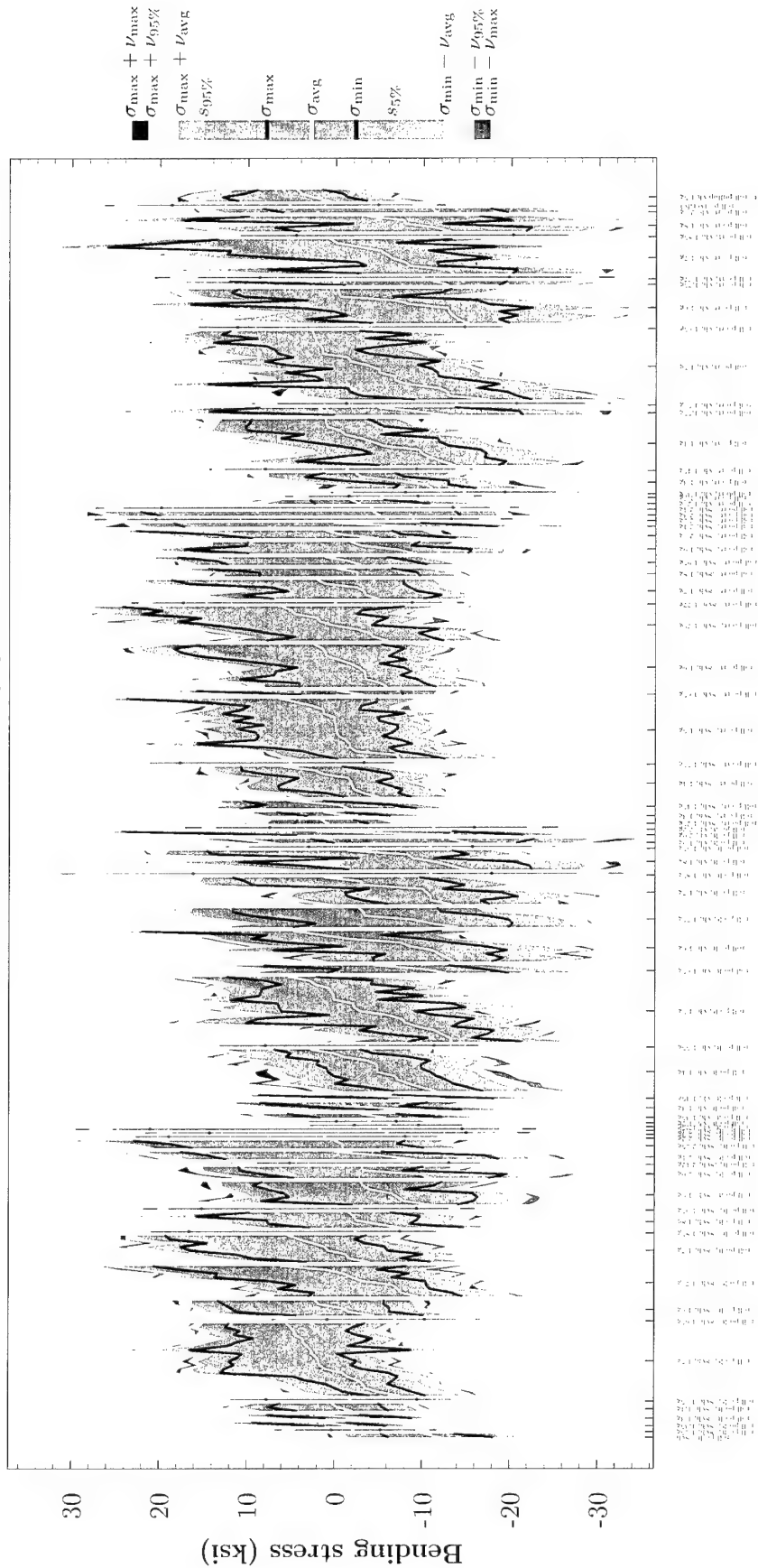


Figure D19: Plot of stabilator spar bending stress for the manoeuvres group of rolling pullout. These stresses were partitioned into manoeuvres, and then sorted by the average steady stress for each run within that manoeuvre. These strain measurement were taken at the zeroth gauge, which is located 9.2" from the stabilator root.

SIDE AND REAR FLIGHT

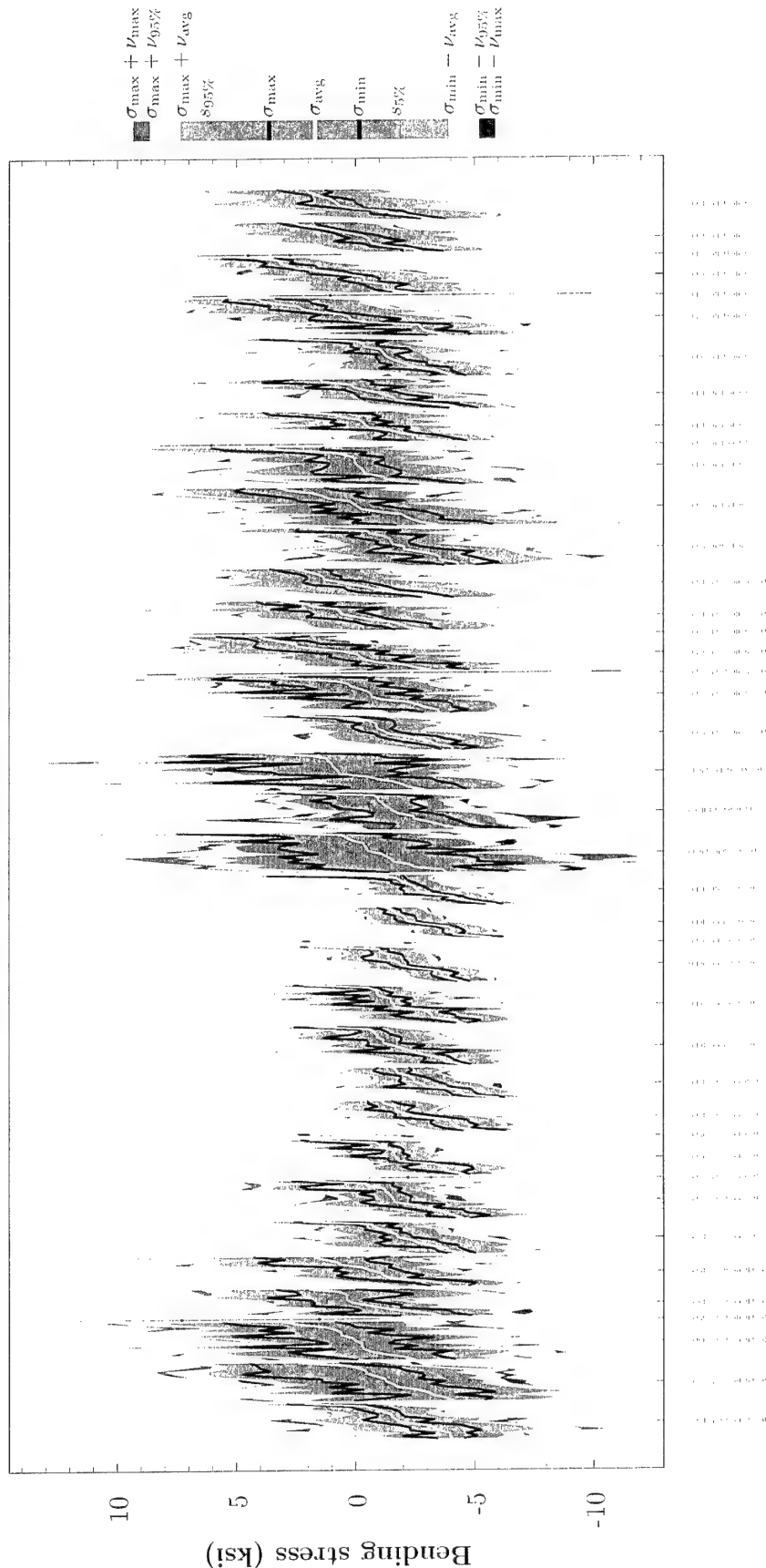


Figure D20: Plot of stabilator spar bending stress for the manoeuvres group of **side and rear flight**. These stresses were partitioned into manoeuvres, and then sorted by the average steady stress for each run within that manoeuvre. These strain measurement were taken at the zeroth gauge, which is located 9.2" from the stabilator root.

SIDESLIP

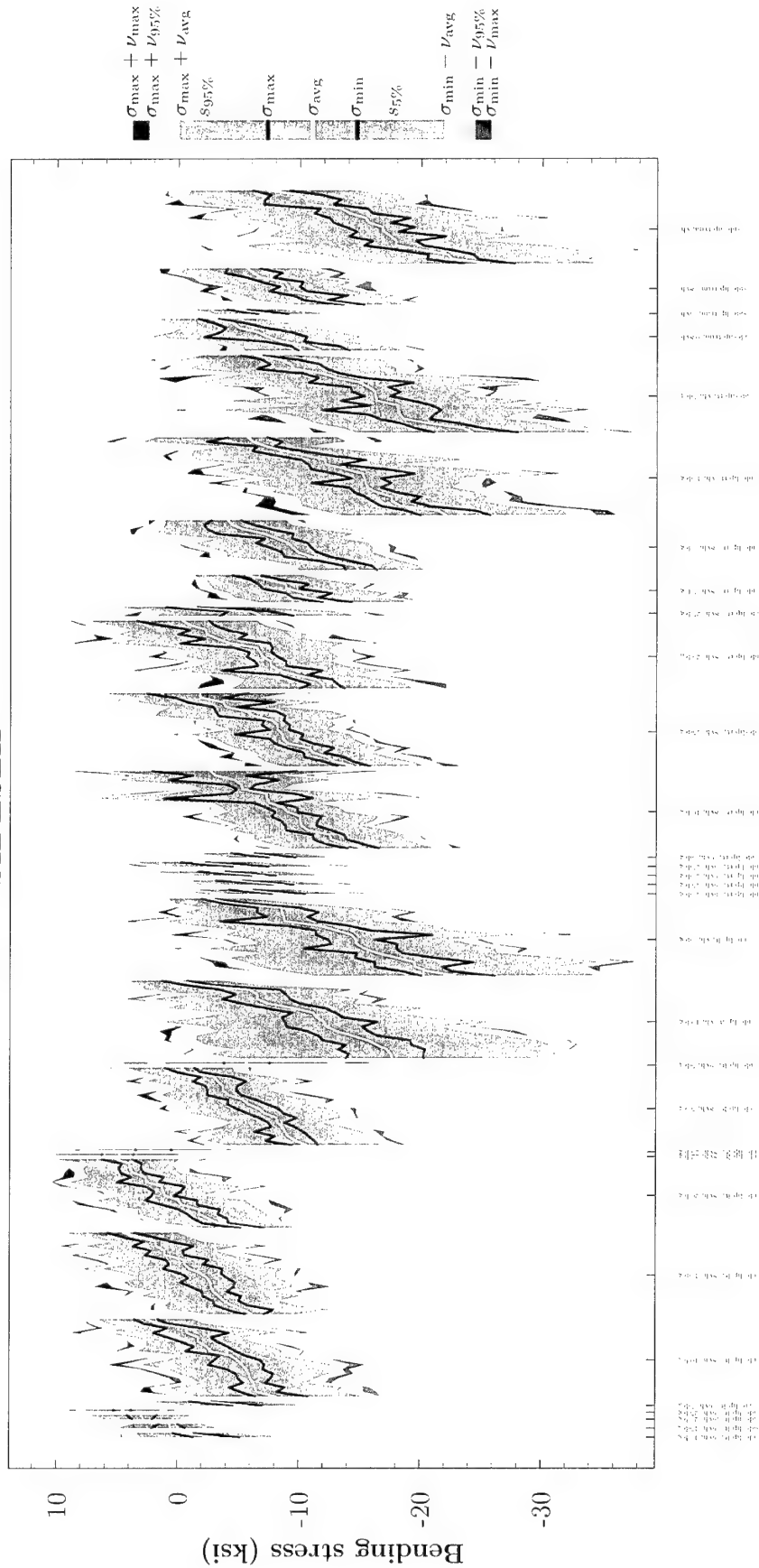


Figure D21: Plot of stabilator spar bending stress for the manoeuvres group of sideslip. These stresses were partitioned into manoeuvres, and then sorted by the average steady stress for each run within that manoeuvre. These strain measurements were taken at the zeroth gauge, which is located 9.2" from the stabilator root.

SYMMETRIC PULLOUT

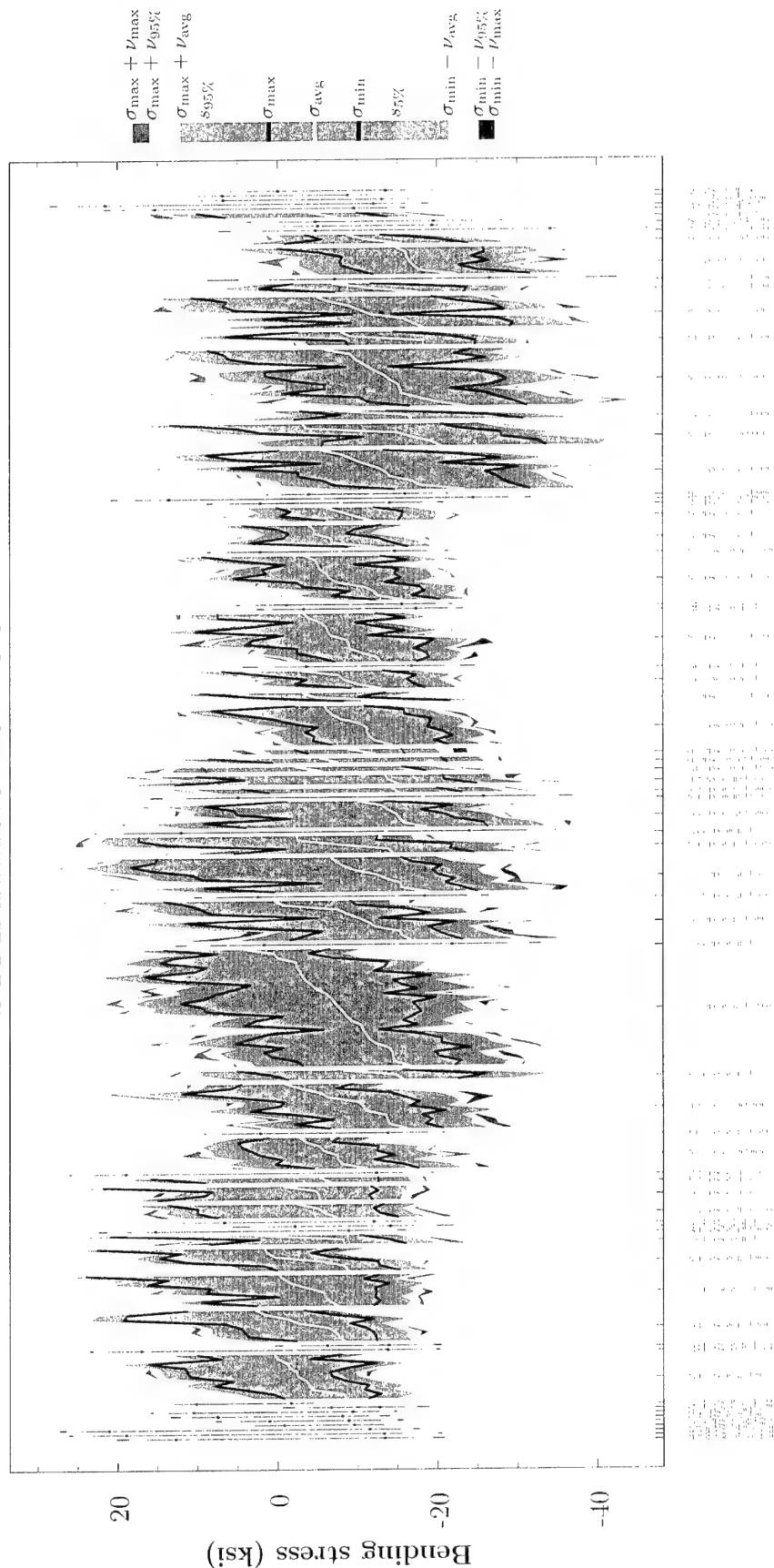


Figure D22: Plot of stabilator spar bending stress for the manoeuvres group of **symmetric pullout**. These stresses were partitioned into manoeuvres, and then sorted by the average steady stress for each run within that manoeuvre. These strain measurement were taken at the zeroth gauge, which is located 9.2" from the stabilator root.

TAXI

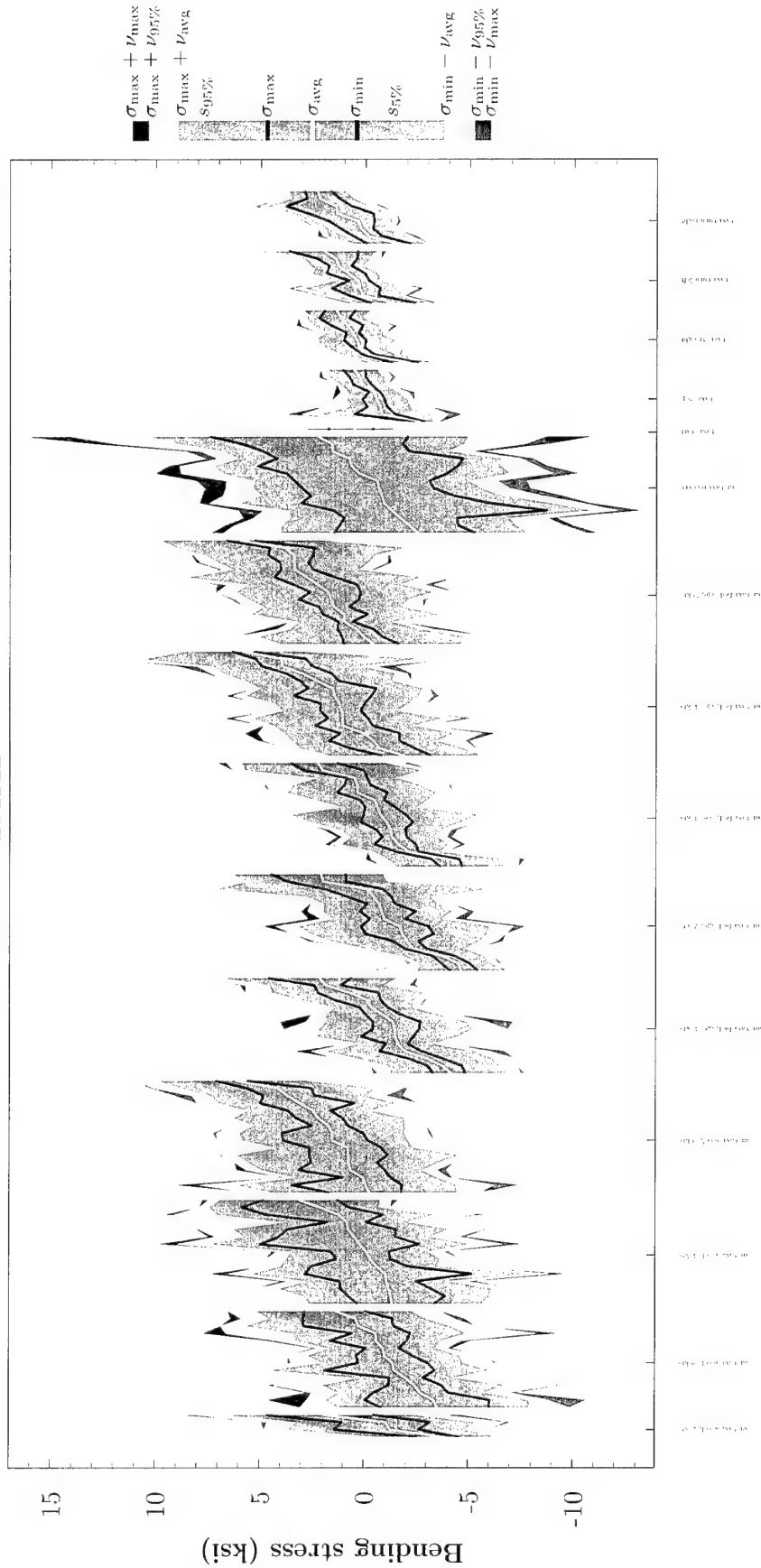


Figure D23: Plot of stabilator spar bending stress for the manoeuvres group of taxi. These stresses were partitioned into manoeuvres, and then sorted by the average steady stress for each run within that manoeuvre. These strain measurement were taken at the zeroth gauge, which is located 9.2" from the stabilator root.

TURNS

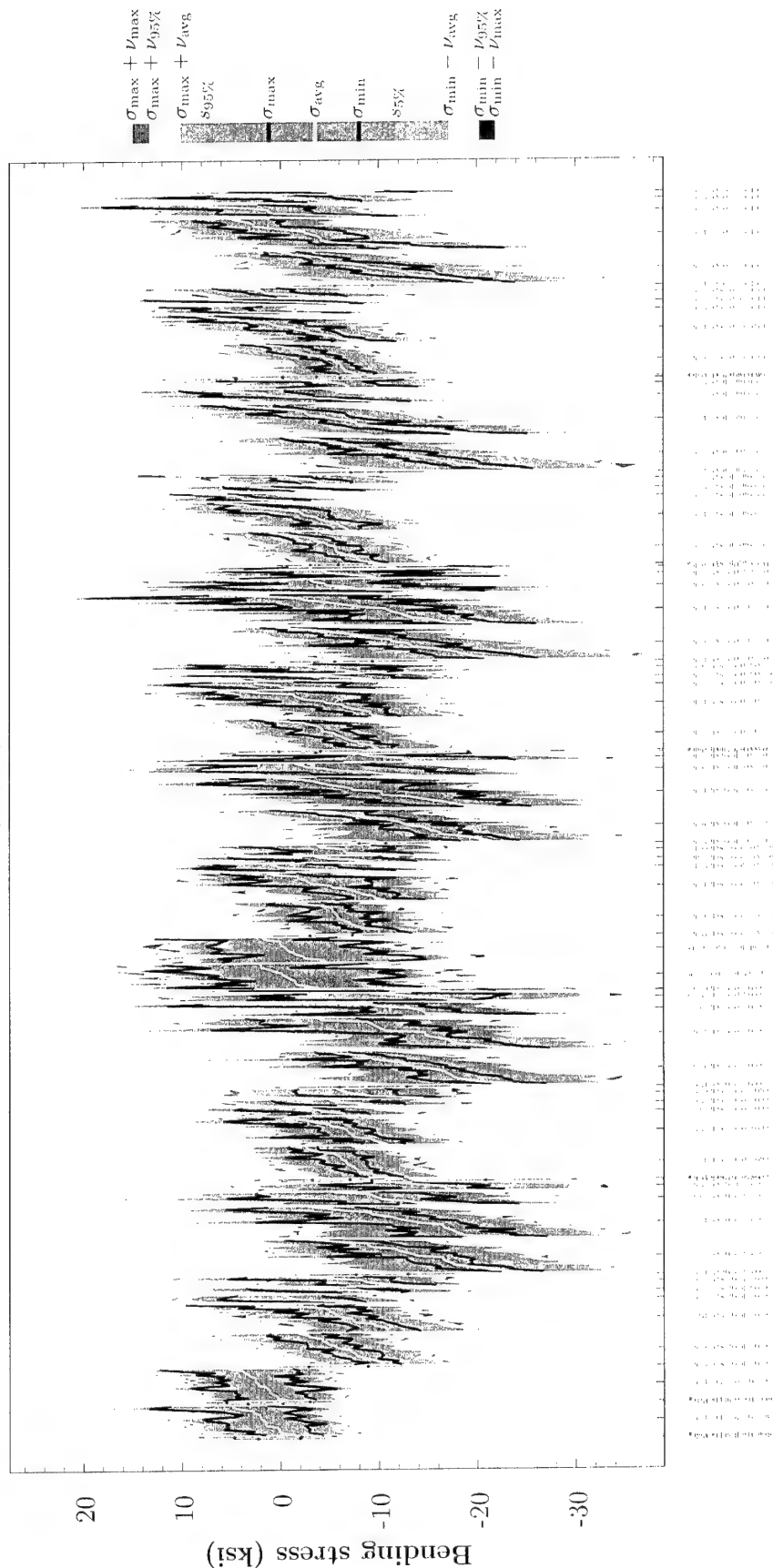


Figure D24: Plot of stabilator spar bending stress for the manoeuvres group of **turns**. These stresses were partitioned into manoeuvres, and then sorted by the average steady stress for each run within that manoeuvre. These strain measurement were taken at the zeroth gauge, which is located 9.2" from the stabilator root.

Appendix E Stabilator Frequency Response: Rolling Pullout and Rough Approach

In Section 6.1 the frequency response of the stabilator to level flight was investigated. In order to check that those results represent a “typical” frequency response, we investigate the frequency response of two further manoeuvres in this appendix.

The two manoeuvres investigated were:

- a rolling pullout manoeuvre from flight 45 run 44 (ROLL_PO_LT,VH,2.2G) and
- a rough approach from flight 69 run 42 (APPROACH,ROUGH).

These manoeuvres were chosen as the antithesis of level flight for the following reasons. The left rolling pullout was chosen because it was thought that the left turn, combined with the pullout motion, would force the unsteady downwash (from the main rotor) onto the stabilator. In contrast, the rough approach would provide frequency information for low speed flight combined with continuously fluctuating stabilator movements.

Figures E1 and E2 show the frequency response of the stabilator respectively for the rolling pullout and rough approach manoeuvres.

As in Section 6.1, the thick black lines represent a twentieth order Chebyshev polynomial through the frequency response shown in the plot. The red lines denote selected multiples of the main and tail rotor frequencies. The box that labels these red lines denotes which multiple of the rotor frequency each line represents.

For a more detailed analysis of these plots see the comments made for the frequency response of the level flight manoeuvre in Section 6.1.

The Mathematica code used to generate these frequency response plots is shown in Figures E3 E6

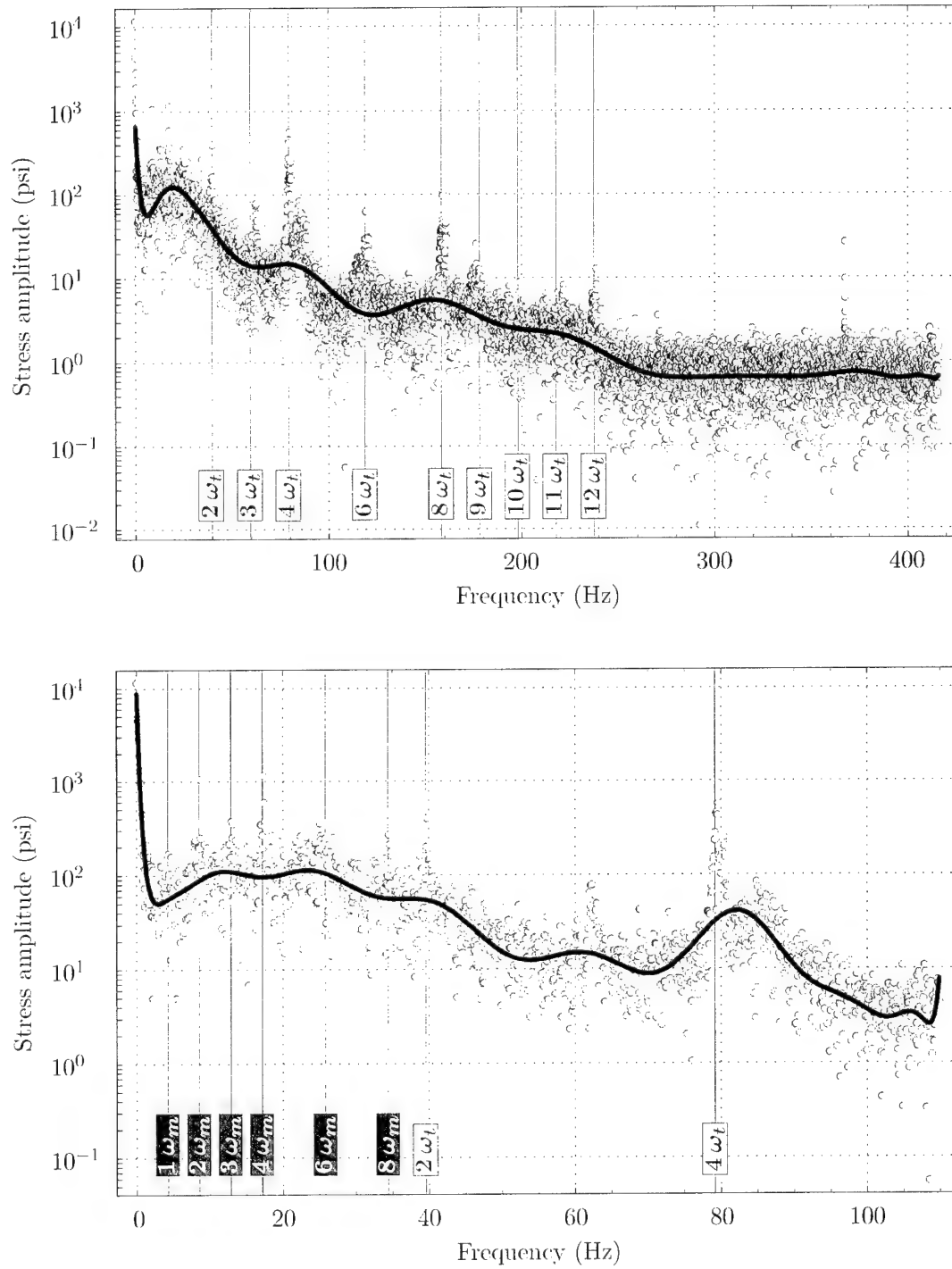


Figure E1: Frequency response of stabilator loading to **rolling pullout**. The red vertical lines labelled with a box denote multiples of the main or tail rotor frequency, which are $\omega_m = 4.3$ Hz and $\omega_t = 19.8$ Hz, respectively.

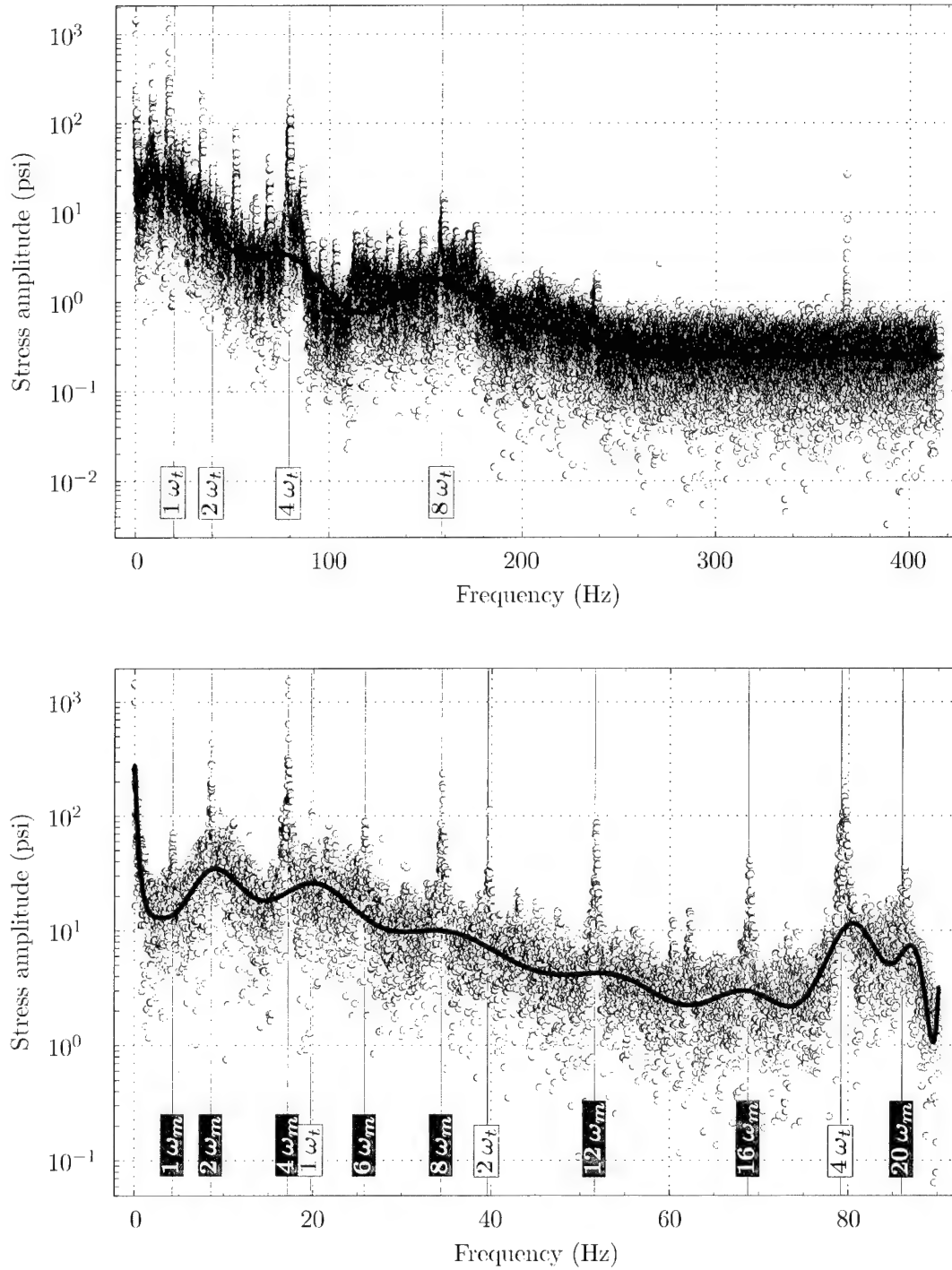


Figure E2: Frequency response of stabilator loading to **rough approach**. The red vertical lines labelled with a box denote multiples of the main or tail rotor frequency, which are $\omega_m = 4.3$ Hz and $\omega_t = 19.8$ Hz, respectively.

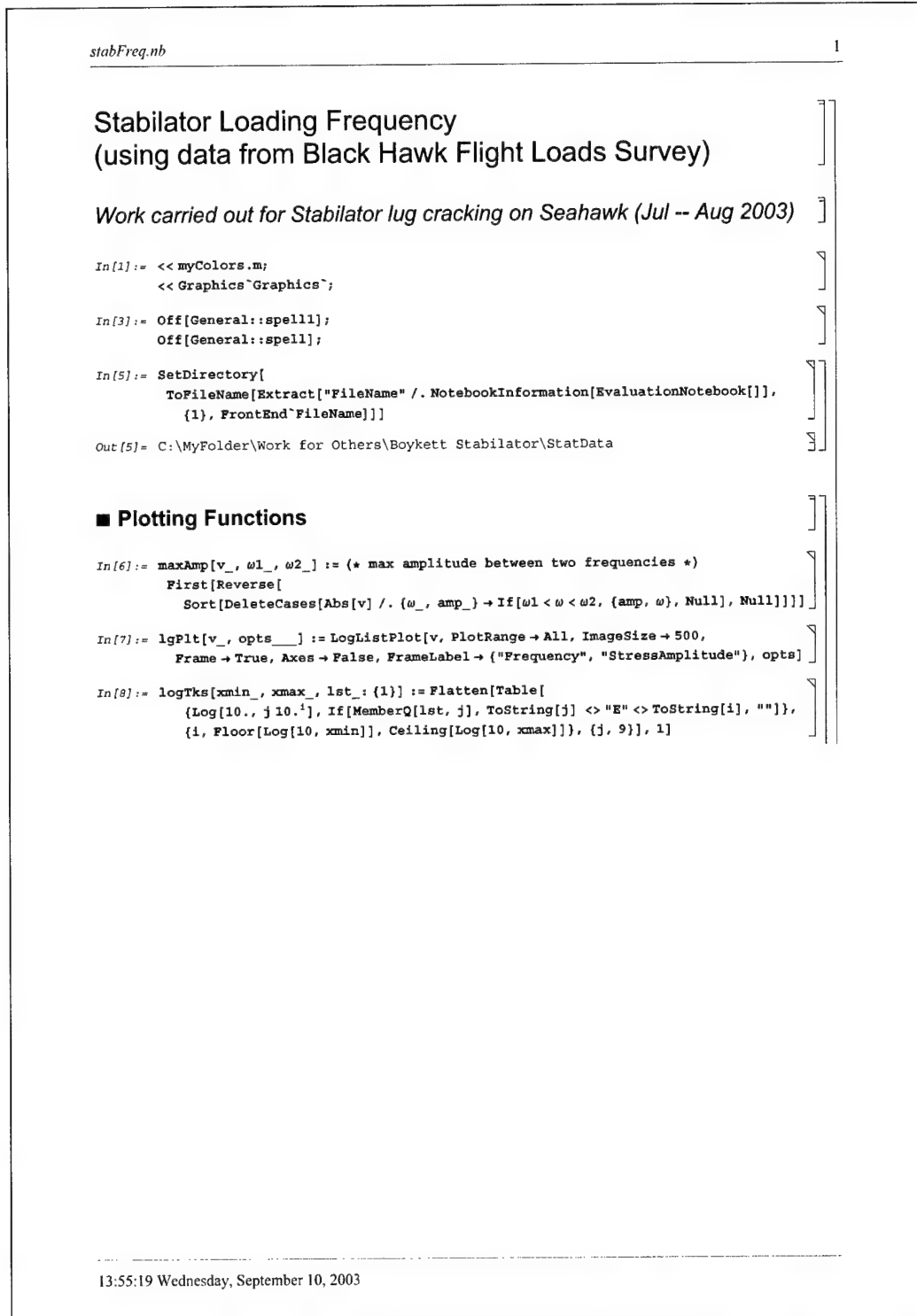


Figure E3: Mathematica code for frequency plots, Page 1.

stabFreq.nb

2

```

In[9]:= pltDat[pts_, n_, polyOrd_, tail_] :=
Module[{v, fn, p1, p2, x0, x1, chebPoly, xa, xb, ya, yb, tks, dsh,
  tksX, tksY, tailRotorFreq = 19.8, rotorTxt, y0, colRotor = Red},
  rotorTxt[i_] := {colRotor,
    Text[ToString[i], {tailRotorFreq+i, y0}, {0, -1}, {0, 1}];
  chebPoly[k_, x_] := chebPoly[k, x] = ChebyshevT[k,  $\frac{2(x-x0)}{(x1-x0)} - 1$ ];
  dsh = Dashing[{0.001, 0.01}];
  y0 = Log[10, Min[Abs[Take[Transpose[pts][[2], n]]]];
  v = Map[{#1], If[#2] < 0, 10-6, Log[10, #2]]} &, Abs[Take[pts, n]]];
  {x0, x1} = {v[[1, 1]], v[[-1, 1]]};
  p1 = lgPlt[Map[{#1], 10#2} &, v], DisplayFunction -> Identity,
    PlotStyle -> {CornflowerBlue}, GridLines -> Automatic];
  {xa, xb}, {ya, yb} = PlotRange /. FullOptions[p1];
  tks = logTks[10ya, 10yb];
  tksX = Prepend[GridLines /. FullOptions[p1]][[1], {0, {GrayLevel[0]}}] /.
    {x_, y_} -> {x, {dsh}};
  tksX = Join[tksX, Map[{#, {colRotor}} &, tailRotorFreq+tail]];
  tksY = DeleteCases[tks, {x_, ""}] /. {x_, y_} -> {x, {dsh}};
  fn = Simplify[Fit[v, Table[chebPoly[i, x], {i, 0, polyOrd}], x]];
  p2 = Plot[fn, {x, 0, v[[-1, 1]]},
    PlotStyle -> {Thickness[0.005]}, DisplayFunction -> Identity];
  Show[{p1, p2, Graphics[Map[rotorTxt, tail]]},
    DisplayFunction -> $DisplayFunction,
    FrameTicks -> {Automatic, tks, Automatic, tks /. {{x_, y_} -> {x, ""}}},
    GridLines -> {tksX, tksY}, TextStyle -> {FontFamily -> "Courier"}}]

```

■ Importing Data (Tape 24 Run 82)

```

In[10]:= Dimensions[dat24 = ReadList["stbnbm1rT024R082.dat"]]
Out[10]= {12907}

In[11]:= fd24 = Module[{v, n, dt = 1/832.},
  v = 2 Fourier[dat24, FourierParameters -> {-1, 1}];
  v = ReplacePart[v, v[[1]]/2, 1];
  n = Round[Length[v]/2.] - 1;
  Transpose[{Range[0,  $\frac{1}{2 \Delta t}$ ,  $\frac{1}{2 n \Delta t}$ ], Take[v, n+1]}]
];

In[12]:= picFullFreq24 = pltDat[fd24, Length[fd24], 20, {2, 3, 4, 6, 8, 9, 10, 11, 12}]
In[13]:= maxAmp[fd24, 360, 370]
Out[13]= {24.7477, 367.457}

```

13:55:20 Wednesday, September 10, 2003

Figure E4: Mathematica code for frequency plots, Page 2.

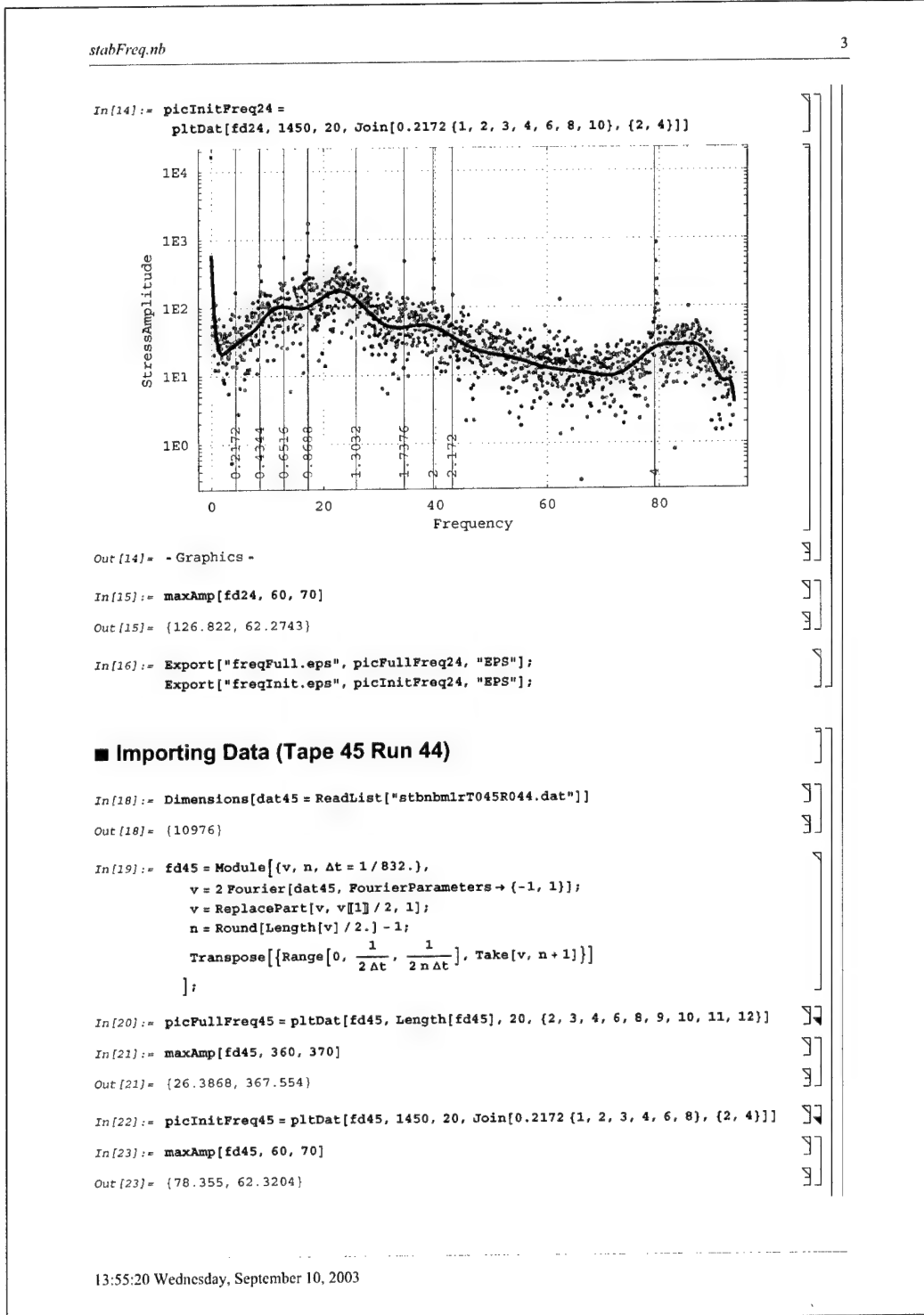


Figure E5: Mathematica code for frequency plots, Page 3.

stabFreq.nb

4

```
In[24]:= Export["fRollFul.eps", picFullFreq45, "EPS"];
Export["fRollIni.eps", picInitFreq45, "EPS"];
```

■ Importing Data (Tape 69 Run 42)

```
In[26]:= Dimensions[dat69 = ReadList["stbnbm1rT069R042.dat"]]
```

```
Out[26]= {68320}
```

```
In[27]:= fd69 = Module[{v, n, Δt = 1/832.},
  v = 2 Fourier[dat69, FourierParameters → {-1, 1}];
  v = ReplacePart[v, v[[1]]/2, 1];
  n = Round[Length[v]/2.] - 1;
  Transpose[{Range[0,  $\frac{1}{2\Delta t}$ ,  $\frac{1}{2n\Delta t}$ ], Take[v, n+1]}]
];
```

```
In[28]:= picFullFreq69 = pltDat[fd69, Length[fd69], 20, {1, 2, 4, 8}]
```

```
In[29]:= maxAmp[fd69, 360, 370]
```

```
Out[29]= {26.5608, 367.603}
```

```
In[30]:= picInitFreq69 =
  pltDat[fd69, 7400, 20, Join[0.2172 {1, 2, 4, 6, 8, 12, 16, 20}, {1, 2, 4}]]
```

```
In[31]:= maxAmp[fd69, 60, 65]
```

```
Out[31]= {14.5888, 62.2313}
```

```
In[32]:= Export["fAprFul.eps", picFullFreq69, "EPS"];
Export["fAprIni.eps", picInitFreq69, "EPS"];
```

13:55:20 Wednesday, September 10, 2003

Figure E6: Mathematica code for frequency plots, Page 4.

Appendix F Bending Stress on Wing Panel Lug

In this section, given a value of vertical load on the stabilator, we calculate the bending stress on the top lug of the forward spar. We want to compare the bending stress from two separate Sikorsky reports [1, 9] with our predictions based on measurements from the Flight Loads Survey.

In Sikorsky's fatigue report [1], a diagram (on page H-10) shows the strain gauge locations during the fatigue test. In particular, a gauge labelled Number 2 (with mnemonic STABL-2) on the top lug of the forward spar appears to be the strain gauge used to check that the correct test loading was applied.

In Sikorsky's flight loads report [9], instead of the bending stress on the forward spar's lug, the vertical loading on the stabilator's wing panel is given. The geometry calculations in this section are used to determine an equivalent bending stress on the top lug of the forward spar, which is where the bending stress from Sikorsky's fatigue report [1] was measured. We will first convert this vertical load into a bending moment, and then convert this bending moment into a bending stress.

To convert a bending moment to a bending stress, we must know the second moment of area (see Equation (3.4) on page 16) on the four lugs supporting each stabilator wing panel. Both the forward and aft spar have two lugs located on the top and bottom of the spars. These lugs attach the stabilator's wing panels to the centre-box, and they form the male part of the clevis lug connection. Figures A4 and A12 (on pages 55 and 63) respectively show the lugs attached to the forward and aft spars. From these figures we can determine the cross-sectional geometry of the lugs for use in second moment of area calculations, see Figure F1.

From the strain gauge location diagram in Sikorsky's fatigue report [1], strain gauge Number 2 appears to be mounted on the lug's upper surface, away from the lug's hole and towards the spar's root. This mounting (away from the hole) would reduce the stress concentration effect produced by the lug's hole. We see from Figure A4 (and more clearly from Figure F1) that between the lug's hole and the spar's root, the lug has a varying cross-sectional area, which is a function of the distance ξ . This distance is measured from the spars root (at BL 9) towards the lug's hole, see Figure F1. To avoid the bending gauge being located above the forward spar or above the hole of the forward spar's lug, we bound the distance ξ within the range

$$0 \leq \xi \leq 0.884.$$

For ease of calculation, the cross-sectional area of the forward spar's lug is partitioned into two regions. These two regions are the constant and fillet regions, which are denoted respectively by the subscripts 1 and 2 on the centroid symbols. (The lug's fillet region is shown cross-hatched in Figure F1.) The height of this fillet region is a function of the distance ξ , and may be calculated from the geometry of a square inscribed in a circle. The radius of the fillet is 1.00", and so the fillet's height is given by the relation

$$\eta = 1 - \sqrt{\xi(2 - \xi)}.$$

The distance from the fillet's centroid to the neutral axis is given by

$$\lambda_f = 1.59 - \eta/2.$$

Figure F1: Dimensions to calculate the second moment of area for the lugs on the stabilator wing panel. These lugs connect the forward and aft spars to the stabilator's centre-box. The angle $\vartheta = 28.7^\circ$ is calculated from the quadrilateral $OABC$.

The angle the aft spar's lug makes with the horizontal (denoted by ϑ) was not shown in any available drawing, and so it was calculated from the given geometry. Figure F1 shows the quadrilateral \mathcal{OABC} , where the point \mathcal{D} lies on the line \mathcal{OC} . The lines \mathcal{AD} and \mathcal{BC} are parallel, and are both perpendicular to the line \mathcal{OC} . Using simple geometry, an equation in terms of ϑ is obtained, $1.866 \sin \vartheta = 0.78 + 0.145 \cos \vartheta$, whose only solution in the range $0 \leq \vartheta \leq 90^\circ$ is $\vartheta = 28.7^\circ$. The centroid of the Region 3 is a distance

$$\lambda_a = 2.500 - (1.196 - \xi) \tan \vartheta$$

from the spar's centreline of symmetry.

A rectangle whose centroid is a distance y from the neutral axis has a second moment of area given by (see Roark [28]) the equation

$$I = bd^3/12 + bd y^2,$$

where b and d are the rectangle's width and height, respectively. The second moment of area for Regions 1 and 2 of the forward spar's lug are then

$$I_1 = 5.27 \text{ in}^4$$

and

$$\begin{aligned} I_2 &= \eta (0.037\eta^2 + 0.444\lambda_f^2) \\ &= 0.565 + \xi(0.262\xi - 0.524) + 0.148(\xi + 0.430)(\xi - 2.43)\sqrt{\xi(2 - \xi)} \text{ in}^4. \end{aligned}$$

The second moment of area for Region 3 of the aft spar's lug is

$$\begin{aligned} I_3 &= 0.181 + 0.685\lambda_a^2 \\ &= 2.51 + \xi(0.205\xi + 1.38) \text{ in}^4. \end{aligned}$$

Summing I_1 , I_2 , and I_3 and multiplying by two (to account for symmetry) gives the total second moment of area of the stabilator wing panel lugs a distance ξ inboard from the spar roots (at BL 9.00)

$$\begin{aligned} I_{wp} &= 2(I_1 + I_2 + I_3) \\ &= 16.7 + \xi(0.935\xi + 1.72) + 0.296(\xi + 0.430)(\xi - 2.43)\sqrt{\xi(2 - \xi)} \text{ in}^4. \end{aligned}$$

This curve is close to linear with a quick turn at $\xi = 0$. The minimum and maximum second moments of area are

$$\min(I_{wp}) = 16.7 \text{ in}^4 \quad (\text{which occurs at } \xi = 0.0184) \quad (\text{F1})$$

and

$$\max(I_{wp}) = 18.4 \text{ in}^4 \quad (\text{which occurs at } \xi = 0.884). \quad (\text{F2})$$

From Sikorsky's loads report [9, p. 47], the maximum vertical load on the right stabilator from the flight loads measurements was $V_{\max} = 1848$ lb. Assume¹⁶ that this vertical load acts through the horizontal centroid of an elliptical lifting distribution. If the spar's length is $L = 74$ in, then the bending moment¹⁷ at the spar's root is given by

$$\begin{aligned}\max(M_r) &= 4V_{\max}L/(3\pi) \\ &= 58 \times 10^3 \text{ in lb.}\end{aligned}\tag{F3}$$

For the forward spar, the height from the centreline of symmetry to the top of lug is $h_f = 3.41''$, see Figure F1. While from Equation (3.4), the bending stress at the top of the forward spar's lug is given by $\sigma_r = M_r h_f / I_{wp}$. Using the maximum bending moment given by Equation (F3) and the range of second moment of area given by Equations (F1) and (F2), yields the range of maximum bending stress at the top of the forward spar's lug

$$11 \text{ ksi} \leq \max(\sigma_r) \leq 12 \text{ ksi.} \quad (\text{derived from vertical load on stabilator}). \tag{F4}$$

A range of maximum stresses was obtained because the second moment of area varied depending on where the bending strain gauge was located.

Sikorsky [1, p. H-16] appear to have carried out the fatigue testing of the stabilator's wing panel at a steady stress of 6.00 ksi and vibratory stresses of 3.75–7.50 ksi. These steady and vibratory stresses sum to a maximum bending stress at top of the forward spar's lug of

$$13.5 \text{ ksi} \quad (\text{obtained from fatigue testing on stabilator}). \tag{F5}$$

We now see that the maximum bending stresses given by Equations (F4) and (F5) (that is, the two different Sikorsky reports) are comparable.

¹⁶The assumptions made in this appendix are not numbered because they are not part of the main analysis.

¹⁷The horizontal centroid (of the quarter-ellipse) occurs at a distance $4L/(3\pi)$ from the root, see page 16.

Appendix G Fractographic Analysis

In this appendix, we examine the cracked lug fractographically in order to obtain a simple lower bound on the number of cycles to failure.

Five regions from the cracked lug's fracture surface were chosen to estimate the overall crack growth rate. Figure G1 shows the cracked lug, as well as the five regions inspected more closely. For the location of this lug tip within the stabilator see Figure 1.3 (shown on page 4).

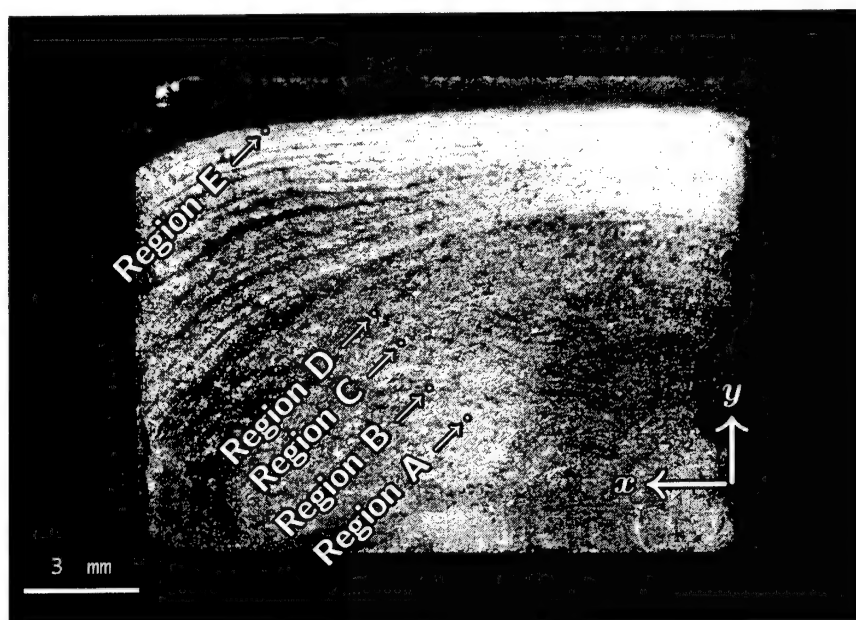


Figure G1: Upper section of cracked lug tip showing positions of the five selected regions for striation sampling. The origin and positive direction of the x and y coordinates are shown by the axes. (Unlabelled photograph courtesy of Rohan Byrnes.)

In each of these five inspection regions, the coordinates of the visible striations were measured in three coordinate x , y , and z . The x and y coordinates lie on the crack propagation plane (see Figure G1). The z coordinate was measured perpendicular to the crack propagation plane, and was determined using the focal length of the microscope. The measured¹⁸ coordinates (which are in millimetres) are shown in Table G1.

These regions were chosen in an approximately straight line from the crack initiation site (the x - y origin in Figure G1) to the crack edge (which is near Region E). Crack striations near the origin were difficult to resolve, so the first region sampled (Region A) was approximately 10 mm from the origin. In order to determine the coordinates of the striations, the sampled regions were magnified 1000 times ($\times 100$ for the lens and $\times 10$

¹⁸These striation coordinates were measured by Rohan Byrnes at DSTO.

Region A				Region B				Region C				Region D				Region E			
x	y	z		x	y	z		x	y	z		x	y	z		x	y	z	
7.8648	2.8769	1.4584	7.8535	2.8533	1.4492	8.5708	4.0386	1.1098	9.2662	4.8074	1.0348	12.0846	9.4418	0.5272					
7.8641	2.8767	1.4584	7.8535	2.8529	1.4492	8.5704	4.0382	1.1098	9.2660	4.8071	1.0348	12.0851	9.4420	0.5272					
7.8641	2.8759	1.4584	7.8528	2.8527	1.4492	8.5699	4.0380	1.1098	9.2656	4.8068	1.0348	12.0851	9.4428	0.5294					
7.8641	2.8756	1.4582	7.8517	2.8530	1.4474	8.5676	4.0381	1.1082	9.2650	4.8062	1.0348	12.0851	9.4433	0.5294					
7.8640	2.8749	1.4582	7.8512	2.8528	1.4474	8.5668	4.0381	1.1070	9.2649	4.8058	1.0348	12.0851	9.4443	0.5300					
7.8635	2.8743	1.4582	7.8504	2.8527	1.4474	8.5655	4.0373	1.1088	9.2647	4.8050	1.0334	12.0859	9.4445	0.5300					
7.8635	2.8737	1.4582	7.8503	2.8519	1.4474	8.5646	4.0367	1.1074	9.2641	4.8047	1.0334	12.0862	9.4451	0.5300					
7.8631	2.8731	1.4582	7.8495	2.8515	1.4474	8.5644	4.0363	1.1074	9.2637	4.8045	1.0334	12.0866	9.4458	0.5300					
7.8631	2.8725	1.4572	7.8494	2.8508	1.4474	8.5640	4.0360	1.1074	9.2631	4.8042	1.0334	12.0868	9.4467	0.5300					
7.8628	2.8723	1.4572	7.8469	2.8516	1.4458	8.5638	4.0354	1.1074	9.2628	4.8038	1.0330	12.0874	9.4472	0.5310					
7.8626	2.8716	1.4572	7.8462	2.8514	1.4458	8.5638	4.0347	1.1074	9.2628	4.8035	1.0330	12.0874	9.4476	0.5310					
7.8622	2.8713	1.4572	7.8456	2.8509	1.4458	8.5631	4.0344	1.1074	9.2624	4.8031	1.0330	12.0874	9.4480	0.5310					
7.8622	2.8708	1.4562	7.8454	2.8500	1.4458	8.5631	4.0336	1.1074	9.2618	4.8026	1.0330	12.0876	9.4486	0.5310					
7.8622	2.8701	1.4562	7.8454	2.8494	1.4458				9.2614	4.8022	1.0330	12.0884	9.4493	0.5320					
7.8620	2.8694	1.4562	7.8449	2.8486	1.4458				9.2608	4.8016	1.0330	12.0894	9.4506	0.5332					
7.8617	2.8691	1.4562	7.8449	2.8478	1.4454				9.2607	4.8013	1.0330	12.0898	9.4517	0.5332					
7.8614	2.8689	1.4562	7.8449	2.8474	1.4454				9.2603	4.8008	1.0316	12.0910	9.4519	0.5332					
7.8614	2.8680	1.4562	7.8445	2.8466	1.4454				9.2599	4.8006	1.0316	12.0910	9.4531	0.5342					
7.8613	2.8674	1.4548	7.8441	2.8463	1.4454				9.2595	4.8001	1.0316	12.0927	9.4532	0.5342					
7.8605	2.8669	1.4548							9.2593	4.7998	1.0316	12.0928	9.4544	0.5342					
7.8604	2.8664	1.4536							9.2579	4.7991	1.0306	12.0935	9.4546	0.5342					
7.8594	2.8661	1.4536							9.2579	4.7987	1.0306	12.0941	9.4555	0.5358					
7.8594	2.8652	1.4536	8.5807	4.0435	1.1132				9.2576	4.7982</									

for the eye piece). The resolution of coordinate measurements and of the motion in the microscope's stage was $0.25 \mu\text{m}$.

One way to estimate the crack growth rate is to determine the distance between visible striations. In other words, if a denotes the crack length from the crack initiation point, then we can estimate the crack growth rate (per loading cycle) as

$$\frac{da}{dN} \approx \frac{\Delta a}{\Delta N}, \quad (\text{G1})$$

where

$$\Delta a = \sqrt{(\Delta x)^2 + (\Delta y)^2} \quad (\text{G2})$$

is the perpendicular distance between visible striations and ΔN is the number of loading cycles between these striations. We need to make an assumption about the number of cycles between visible crack striations in order to estimate the number of cycles it took to completely crack the lug:



Assumption 17 *There is only one loading cycle between visible crack striations, that is, $\Delta N=1$ in Equation (G1).*

In other words, at a magnification of $\times 1000$, only loading cycles that cause these visible crack striations are considered. This assumption means that any estimate we obtain for the number of cycles to failure has to necessarily be a *lower bound* on the true value. This statement follows from the fact that there are more striations than could be seen at a magnification of $\times 1000$.

The crack's total length (which is approximately 16 mm) can only be measured in the plane of the crack, that is, in the x - y plane. (It would be impossible to measure the millions of out-of-plane surface variations along the crack's length.) Hence when measuring crack growth we ignore the variation in the z coordinate both (i) between striations (in Equation (G2)) and (ii) of the total crack length.

Using Equation (G1), the crack growth rate can be estimated using the measured coordinates of the visible crack striations. If (x_i, y_i, z_i) represents the coordinates of the i th measured striation, then

$$\frac{\Delta a}{\Delta N} = \sqrt{(x_{i+1} - x_i)^2 + (y_{i+1} - y_i)^2}, \quad (\text{G3})$$

since $\Delta N=1$ from Assumption 17. Estimates of the crack growth rate, calculated using Equation (G3), are plotted in Figure G2. Note that the crack growth Δa and crack growth rate $\Delta a/\Delta N$ are equivalent for these striation measurements because we have assumed that $\Delta N=1$.

In Figure G2, the box-plots show the 5th, 25th, 50th, 75th, and 95th percentiles of the relevant data. The 5th and 95th percentiles are denoted by the lower and upper parts, respectively, of the box-plot's whiskers. The 25th and 75th quartiles are denoted by the lower and upper sections, respectively, of the box-plot's rectangle. The median (or 50th percentile) is denoted by the horizontal bar through the mid-region of the box-plot's rectangle, which extends through the domain of the relevant data. The solid black line

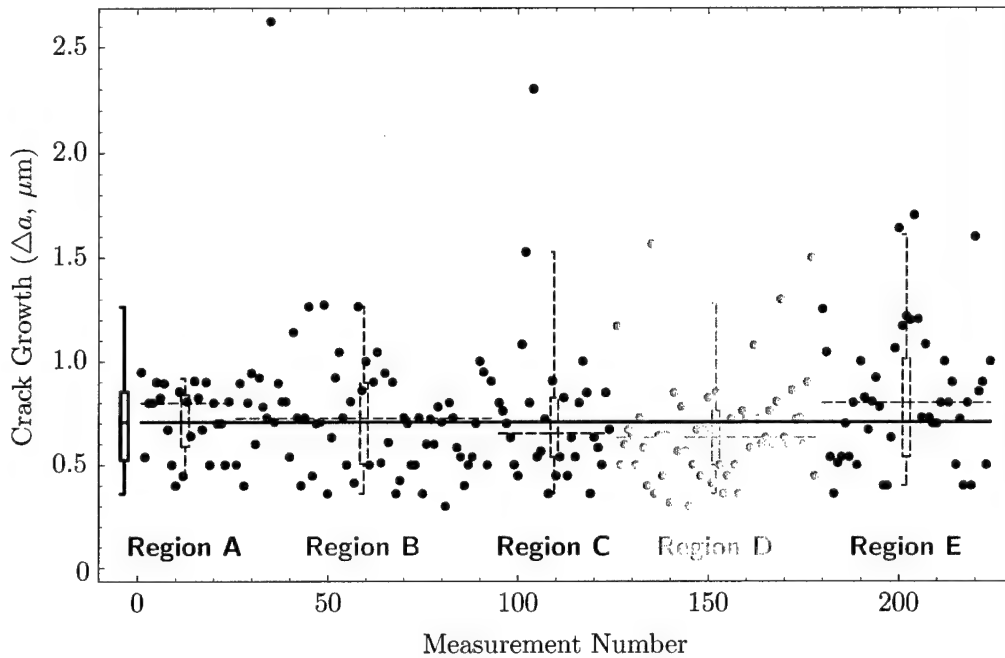


Figure G2: *Estimate of crack growth rate from five selected regions. Box-plots show 5th, 25th, 50th, 75th, and 95th percentiles. Horizontal dashed lines and dashed box-plots denote median and percentiles, respectively, of individual regions. Solid black line and solid box-plot denote median and percentiles, respectively, of five regions aggregated.*

through all five regions and the solid box-plot on the left denote the median and percentiles of the aggregated data from all five regions.

We can estimate the number of cycles to failure by dividing the total crack length by the crack growth rate, but first we need to make an assumption about the way in which the crack grows:



Assumption 18 *The crack grows linearly (that is, at a constant rate) throughout its length.*

In reality, the crack growth rate probably follows some sort of power law as a function of crack length. For example, a simple law for crack growth rate is given by

$$\frac{da}{dN} = C(\Delta K)^m, \quad (\text{G4})$$

where C is a coefficient, ΔK is the range of the stress intensity factor, and m is the characteristic slope for the curve of the crack growth rate. (See Megson [20] or the fracture mechanics ESDU data sheet [21] for further details.) Both C and m are dependent on the material properties and the mean stress under consideration.

Let S_{\min} and S_{\max} denote respectively the minimum and maximum values for stress within a cycle of a constant amplitude loading. In its simplest form, the range of the stress

intensity factor is given by

$$\Delta K = (S_{\max} - S_{\min}) \sqrt{\pi a} \alpha, \quad (\text{G5})$$

where α is a non-dimensional length coefficient, which usually expressed as the ratio of crack length to any convenient local dimension in the plane of the component.

Combining Equations (G4) and (G5), we see that the crack growth rate (given by this simple law) is a power function of the crack length. The data shown in Figure G2 suggests that the crack growth rate is relatively constant, and hence at least for the later part of the crack the characteristic slope m must be close to zero.

From Figure G2 we can determine the median crack growth rate of the five sampled regions, as well as the five regions aggregated. These median values for the crack growth rate are shown in Table G2. As can be seen, the crack growth rate appears to remain relatively constant (at approximately $0.7 \mu\text{m}/\text{cycle}$) over the five sampled regions.

Table G2: Median of crack growth rate for five sampled regions and regions aggregated.

Region	A	B	C	D	E	Aggregate
Crack growth rate ($\mu\text{m}/\text{cycle}$)	0.8	0.7	0.7	0.6	0.8	0.7

Using Assumption 18, we can divide the total crack length (which is 16 mm) by the median crack growth rate (which is $0.7 \mu\text{m}/\text{cycle}$) to obtain a *lower bound* on the number of cycles to failure: 20×10^3 cycles.

Dividing the number of flight hours before the crack was detected (which is approximately 400 hours) by the number of cycles (which is 20×10^3 striations), we obtain the cycle period:

1 minute (between cycles causing *visible striations*).

In obtaining this period we have made an implicit assumption about when the crack began:



Assumption 19 *The crack began when the component was installed (which was 402 flight hours before detection).*

If the crack began significantly after installation, then the time between cycles given above would be significantly shorter.

This 1 minute period between cycles suggests that at least the visible striations were caused by loading that occurred approximately once per manoeuvre.

DISTRIBUTION LIST

Fatigue Life Estimate of Centre-Box Lug in Seahawk's Stabilator

Frank G. Polanco and Robert P. H. Boykett

Number of Copies

AUSTRALIA

DEFENCE ORGANISATION

S & T Program

Chief Defence Scientist	}	1
FAS Science Policy		
AS Science Corporate Management		
Director General Science Policy Development		
Counsellor Defence Science, London		Doc Data Sheet
Counsellor Defence Science, Washington		Doc Data Sheet
Scientific Adviser to MRDC, Thailand		Doc Data Sheet
Scientific Adviser Joint		1
Navy Scientific Adviser		1
Scientific Adviser, Army		Doc Data Sheet
Air Force Scientific Adviser		1
Scientific Adviser to the DMO M&A		Doc Data Sheet
Scientific Adviser to the DMO ELL		Doc Data Sheet
Director Trials		1

Platforms Sciences Laboratory

Chris Guy (Chief of Air Vehicles Division)	Doc Data Sheet
Graham Clark (Research Leader Structural Integrity)	Doc Data Sheet
Philip Jackson (Head of Helicopters and Transport Aircraft)	1
Frank G. Polanco (author)	1
Robert Boykett (author and task manager)	1
Domenico C. Lombardo	1
Chris G. Knight	1
Luther Krake	1
Christine Trasteli	1
Soon-Aik Gan	1
Christopher Dore	1
Cecil N. King	1
Noel Goldsmith	1
Rohan Byrnes	1

DSTO Libraries and Archives

Library Fishermans Bend	1
Library Edinburgh	1
Australian Archives	1
Library, Sydney	Doc Data Sheet
Library, Stirling	Doc Data Sheet
Library, Canberra	Doc Data Sheet

Capability Systems Division

Director General Maritime Development	Doc Data Sheet
Director General Land Development	1
Director General Information Capability Development	Doc Data Sheet

Office of the Chief Information Officer

Deputy CIO	Doc Data Sheet
Director General Information Policy and Plans	Doc Data Sheet
AS Information Structures and Futures	Doc Data Sheet
AS Information Architecture and Management	Doc Data Sheet
Director General Australian Defence Simulation Office	Doc Data Sheet

Strategy Group

Director General Military Strategy	Doc Data Sheet
Director General Preparedness	Doc Data Sheet

HQAST

SO (Science) (ASJIC)	Doc Data Sheet
----------------------	----------------

Navy

SO (SCIENCE), COMAUSNAVSURFGRP, NSW	Doc Data Sheet
Director General Navy Capability, Performance and Plans, Navy Headquarters	Doc Data Sheet
Director General Navy Strategic Policy and Futures, Navy Headquarters	Doc Data Sheet

Army

ASNSO ABCA, Puckapunyal	4
SO(Science), DJFHQ(L), MILPO Enoggera, Qld 4051	1
Commander Aviation Support Group, Oakey	1
NAPOC QWG Engineer NBCD c/- DENGERS-A, HQ Engineer Centre Liverpool Military Area, NSW 2174	Doc Data Sheet

Air Force

Director General Technical Airworthiness (Attn OIC RWS), RAAF Williams	3
--	---

Army

ABCA National Standardisation Officer, Land Warfare Development Sector, Puckapunyal	Doc Data Sheet
---	----------------

SO (Science), Deployable Joint Force Headquarters (DJFHQ) (L), Enoggera QLD	Doc Data Sheet
---	----------------

SO (Science) - Land Headquarters (LHQ), Victoria Barracks NSW	Doc Data Sheet
---	----------------

Intelligence Program

DGSTA Defence Intelligence Organisation	1
---	---

Manager, Information Centre, Defence Intelligence Organisation	1
--	---

Assistant Secretary Corporate, Defence Imagery and Geospatial Organisation	Doc Data Sheet
--	----------------

Defence Materiel Organisation

Head Airborne Surveillance and Control	Doc Data Sheet
--	----------------

Head Aerospace Systems Division	Doc Data Sheet
---------------------------------	----------------

Head Electronic Systems Division	Doc Data Sheet
----------------------------------	----------------

Head Maritime Systems Division	Doc Data Sheet
--------------------------------	----------------

Head Land Systems Division	Doc Data Sheet
----------------------------	----------------

Head Industry Division	Doc Data Sheet
------------------------	----------------

Chief Joint Logistics Command	Doc Data Sheet
-------------------------------	----------------

Management Information Systems Division	Doc Data Sheet
---	----------------

Head Materiel Finance	Doc Data Sheet
-----------------------	----------------

Defence Libraries

Library Manager, DLS-Canberra	Doc Data Sheet
-------------------------------	----------------

Library Manager, DLS - Sydney West	Doc Data Sheet
------------------------------------	----------------

OTHER ORGANISATIONS

National Library of Australia	1
-------------------------------	---

NASA (Canberra)	1
-----------------	---

UNIVERSITIES AND COLLEGES

Australian Defence Force Academy Library (ADFA)	1
---	---

Head of Aerospace and Mechanical Engineering, ADFA	1
--	---

Deakin University Library, Serials Section (M List), Geelong 3217	1
---	---

Monash University, Hargrave Library	Doc Data Sheet
-------------------------------------	----------------

Librarian, Flinders University	1
--------------------------------	---

OUTSIDE AUSTRALIA

INTERNATIONAL DEFENCE INFORMATION CENTRES

US Defense Technical Information Center	2
UK Defence Research Information Centre	2
Canada Defence Scientific Information Service	1
NZ Defence Information Centre	1

ABSTRACTING AND INFORMATION ORGANISATIONS

Library, Chemical Abstracts Reference Service	1
Engineering Societies Library, US	1
Materials Information, Cambridge Science Abstracts, US	1
Documents Librarian, The Center for Research Libraries, US	1

INFORMATION EXCHANGE AGREEMENT PARTNERS

National Aerospace Laboratory, Japan	1
National Aerospace Laboratory, Netherlands	1

SPARES	5
--------	---

Total number of copies:	55
--------------------------------	-----------

DEFENCE SCIENCE AND TECHNOLOGY ORGANISATION DOCUMENT CONTROL DATA				1. CAVEAT/PRIVACY MARKING	
2. TITLE Fatigue Life Estimate of Centre-Box Lug in Sea-hawk's Stabilator			3. SECURITY CLASSIFICATION Document (U) Title (U) Abstract (U)		
4. AUTHORS Frank G. Polanco and Robert P. H. Boykett			5. CORPORATE AUTHOR Platforms Sciences Laboratory 506 Lorimer St, Fishermans Bend, Victoria, Australia 3207		
6a. DSTO NUMBER DSTO-TR-1590		6b. AR NUMBER AR-013-125		6c. TYPE OF REPORT Technical Report	
				7. DOCUMENT DATE July 2004	
8. FILE NUMBER M1/9/1220		9. TASK NUMBER ARM 03/227		10. SPONSOR DGTA	
				11. No OF PAGES 124	
				12. No OF REFS 28	
13. URL OF ELECTRONIC VERSION http://www.dsto.defence.gov.au/corporate/reports/DSTO-TR-1590.pdf			14. RELEASE AUTHORITY Chief, Air Vehicles Division		
15. SECONDARY RELEASE STATEMENT OF THIS DOCUMENT <i>Approved For Public Release</i> OVERSEAS ENQUIRIES OUTSIDE STATED LIMITATIONS SHOULD BE REFERRED THROUGH DOCUMENT EXCHANGE, PO BOX 1500, EDINBURGH, SOUTH AUSTRALIA 5111					
16. DELIBERATE ANNOUNCEMENT No Limitations					
17. CITATION IN OTHER DOCUMENTS No Limitations					
18. DEFTEST DESCRIPTORS Fatigue (Materials); Fatigue tests; Stabilators; Military helicopters; Lugs; Cracks					
19. ABSTRACT <p>The fatigue failure of a centre-box lug, found in the Seahawk's stabilator, highlighted deficiencies in the fatigue life assessment of helicopter airframe structure. Thus a methodology for fatigue life assessment was developed using this cracked lug as a demonstrator. Indirect measurements from the Flight Loads Survey on the Black Hawk, although not ideal, allowed the estimation of the amplitude and frequency of the lug's loading. Of the sixteen assumptions made in this fatigue analysis, the most restrictive was that a high amplitude and high frequency loading acts for the entire flying time. Three different fatigue lives were obtained based on different levels of conservatism in the loading estimates. These three loadings were: the worst-case scenario, a high loading scenario, and a best-case scenario. The worst-case and high-loading scenarios resulted in low fatigue lives, while the best-case scenario resulted in an unlimited life for the cracked lug. It was surprising to find such low fatigue lives for two of these scenarios, but these low lives may be due to the conservative assumptions used in the analysis.</p>					